Large deformation near a crack tip in a fiber-reinforced neo-Hookean sheet with discrete and continuous distributions of fiber orientations

Luca Di Stasio [*], Yin Liu, Brian Moran

Division of Physical Sciences and Engineering, King Abdullah University of Science and Technology (KAUST), Thuwal 23955-6900, Saudi Arabia

A B S T R A C T

We consider crack tip deformations under plane stress conditions of a Neo-Hookean sheet reinforced by Neo-Hookean fibers, whose orientation and elastic properties are described by discrete and continuous spatial distributions. The mechanical behavior of the composite is described in terms of the first and fourth invariant of the right Cauchy-Green tensor following Guo et al. [1–3]. The crack tip integrals developed in Liu and Moran [4,5] are used to determine the coefficients of the crack tip asymptotic expansion. The *von Mises* distribution of orientation is analyzed. The existence of a regime of isotropic behavior, which we call *asymptotic isotropy*, in the region of dominance of the asymptotic fields is established for certain combinations of fiber orientations. Finally, the possibility to construct an *asymptotic universal one-to-one mapping* between anisotropic and isotropic Neo-Hookean plane stress response at the crack tip is discussed.

1. Introduction

A large class of both biological and synthetic bioinspired soft materials can be modeled as composed of a hyperelastic matrix reinforced by one or more families of hyperelastic fibers. Each family of fibers is characterized by their specific elastic properties and an orientation in space, and the overall variation in elastic properties and orientations is expressed in terms of discrete or continuous distributions. We thus refer to this class of materials as hyperelastic materials reinforced by a distribution of fibers. Examples are numerous: articular cartilage [6], human cornea [7], aneurysms [8], human brain arteries [9], muscle tissue [10], the aorta [11], aortic heart valves [12], hydrogels [13], scaffolding materials to grow load-bearing soft tissues [14], ink-printed hydrogels reinforced by cellulose fibrils [15].

Focusing on the mechanical response of arterial layers, the importance of the presence of distributions of fibers in soft materials is emphasized in [16]. In the latter, the authors include the effect of the distributed fiber orientations through a generalized structure tensor in the framework of anisotropic large-deformation elasticity. By means of numerical experiments, they show that the mechanical response of the soft-composite is strongly dependent of the fiber distribution. A highly dispersed distribution of orientations translates into a stiffer material less dependent on the main direction of alignment of the fibers, whereas a distribution concentrated around the main direction causes a highly

direction-dependent response. They furthermore observe that, in the case of a single fiber orientation, fibers undergo large rotations before carrying load to align with the direction of the applied load. They thus conclude that the study of ideally aligned fibers, i.e. all parallel to one direction, is not sufficient to predict the mechanical response of fiber-reinforced soft materials. In [16], the authors adopt a continuum mechanics approach and use the strain-energy superposition assumption. Based on the volumetric-distortional decomposition of [17,18], the strain-energy superposition assumption allows the additive split of the strain energy into a purely volumetric term and a purely distortional term [19] and it is valid for incompressible and nearly-incompressible materials [20]. In the case of fiber-reinforced soft composites, the matrix may be considered as the driver of volumetric deformations whereas fibers are responsible for the isochoric distortional part of the deformation. Thus, the contribution to the strain energy density of the two phases can be additively split by identifying the matrix contribution with the volumetric term and the fiber contribution with the distortial term of the volumetric-distortional decomposition [6,21]. In the presence of multiple families of fibers located in a finite and discrete set of orientations and properties, the contributions of each family of fibers (meant as a set of fibers with one specific orientation and the same set of mechanical properties) are summed up to provide the distortional part of the strain-energy density [22]. In the case of a continuous distribution of orientations and/or mechanical properties, the finite sum becomes a

---

distribution-weighted integral [6,16,21,23]. Further details on the continuum mechanics approach to modeling fiber-reinforced soft materials with discrete or continuous distribution of orientations or properties can be found in the reviews of [24,25]. Efforts at modeling the failure behavior have proposed a number of approaches, namely limiting failure criteria [26], softening models [27], micro-structural damage mechanisms [28,29], cohesive surfaces [30], internal damage variables [31,32], permanent deformations [33], statistical approaches [34], bond kinetics [35], phase field modeling [36] (see [37] for a thorough review on the subject).

It appears however that the analysis of the behavior of the elastic fields at the crack tip remains unaddressed. In [4], a set of crack tip contour integrals is presented to evaluate the parameters determining the stress and deformation fields at the crack tip in an isotropic hyperelastic material under conditions of plane stress or plane strain. The integrals are then extended in [5] to anisotropic fiber-reinforced soft materials with fibers oriented in one or two directions. Building upon this previous work, the crack tip contour integrals approach is applied in this paper to the analysis of the crack tip large deformation fields in Neo-Hookean sheets reinforced by discrete and continuous distributions of fibers under conditions of plane stress.

This paper is organized as follows. In Section 2, the governing equations of a Neo-Hookean matrix reinforced by discrete and continuous distributions of fibers are introduced for general 3D deformation fields. The model is then restricted to plane stress conditions and its main equations are provided in Section 3. The asymptotic boundary value problem and its solution are introduced in Section 4. Section 5 briefly introduces the crack tip integrals used for the evaluation of the coefficients of the asymptotic expansion derived in Section 4. Numerical results for discrete and continuous distributions of fibers are presented and analyzed in Section 6. Conclusions are finally discussed in Section 7.

2. Governing equations

In the presence of multiple families of fibers, their properties and orientation are described by a distribution function $f(\mathbf{a}_0, \kappa)$. In general, for a given family of fibers the vector

$$\mathbf{a}_0 = \sin\phi\cos\psi\mathbf{e}_1 + \sin\phi\sin\psi\mathbf{e}_2 + \cos\phi\mathbf{e}_3 \tag{1}$$

represents the fiber orientation in the material reference (undeformed) configuration in a three-dimensional space spanned by the unit vectors
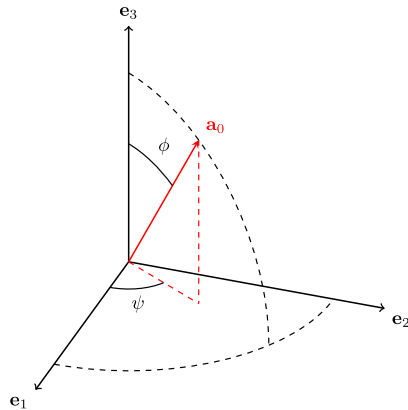
e_1, e_2, e_3 using the spherical coordinates ϕ and θ (see Fig. 1). On the other hand, the parameter κ in the distribution function $f(\mathbf{a}_0, \kappa)$ represents the ratio of fiber to matrix shear moduli such that $\mu_f = \kappa\mu$ where μ is the matrix shear modulus.

When considered transversely isotropic, the strain energy density function W (per unit of undeformed volume) of fiber-reinforced hyperlastic materials is, in general, a function of the first five invariants I_1, I_2, I_3, I_4, I_5 of the right Cauchy-Green tensor $\mathbf{C} = \mathbf{F}^T\mathbf{F}$ [38]. $\mathbf{F}$ represents the deformation gradient whose components are given by $F_{ij} = \frac{\partial y_i}{\partial x_j}$, where x_j and y_i denote the coordinates respectively in the undeformed and deformed configuration. The first three invariants do not depend on fiber properties and orientation and can be expressed as

$$I_1 = tr\mathbf{C} \quad I_2 = \frac{1}{2}\left[(tr\mathbf{C})^2 - tr\mathbf{C}^2\right] \quad I_3 = det\mathbf{C}, \tag{2}$$

or, in terms of the three principal stretches $\lambda_1, \lambda_2, \lambda_3$ as

$$I_1 = \lambda_1^2 + \lambda_2^2 + \lambda_3^2 \quad I_2 = \lambda_1^2\lambda_2^2 + \lambda_2^2\lambda_3^2 + \lambda_3^2\lambda_1^2 \quad I_3 = \lambda_1^2\lambda_2^2\lambda_3^2. \tag{3}$$

On the other hand, the fourth and fifth invariant depend on fiber properties and orientation and can be represented as

$$I_4 = \mathbf{a}_0^T\mathbf{C}\mathbf{a}_0 \quad I_5 = \mathbf{a}_0^T\mathbf{C}^2\mathbf{a}_0. \tag{4}$$

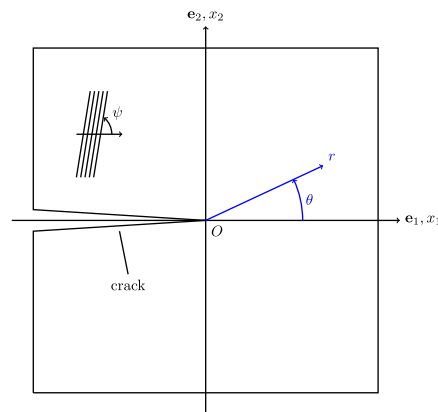The functional form of the distribution function is such that

$$\frac{1}{4\pi}\int_\kappa\int_S f(\mathbf{a}_0,\kappa)dSd\kappa = 1, \tag{5}$$

where S represents any spherical surface inside the material domain. Note that the approach proposed may also be used to model discrete distributions of fibers, by taking $f(\mathbf{a}_0,\kappa) = \sum_i^n \delta(\mathbf{a}_0^i, \kappa^i)$ where $\delta(\cdot)$ is the Dirac delta. In the case $f(\mathbf{a}_0,\kappa) = \delta(\mathbf{a}_0,\kappa)$, a model with a single family of fibers is retrieved. We restrict our attention here to fiber-reinforced hyperlastic materials whose strain energy density is a function $W(I_1, I_4)$ only of the first and fourth invariant and where the contribution of each invariants can be isolated by an additive decomposition

$$W(I_1, I_4) = W_m(I_1) + W_f(I_4) \tag{6}$$

Following [1,2,3], we assume the contribution of I_1 to be Neo-Hookean

$$W_m(I_1) = \frac{\mu}{2}(I_1 - 3) \tag{7}$$

(a) Spherical coordinates employed in Equation 1. $\phi \in [0, \pi)$ is the inclination, $\psi \in [0, \pi)$ the azimuth.

(b) A thin sheet of fiber-reinforced hyperelastic material with an edge crack. Reference configuration of the plane stress problem with both the global cartesian coordinates $x_1 - x_2$ and polar coordinates r, θ at the crack tip.

Fig. 1. Reference frames assumed in this work.

and that of I_4 to be, for any family of fibers [1]

$$w_f(I_4(\mathbf{a}_0, \kappa)) = \kappa \frac{\mu}{2} \left(I_4 + 2I_4^{-\frac{1}{2}} - 3 \right) \tag{8}$$

The total contribution to the strain energy of the fourth invariant can be thus calculated as

$$W_f(I_4) = \frac{1}{4\pi} \int_\kappa \int_S f(\mathbf{a}_0, \kappa) w(I_4(\mathbf{a}_0, \kappa)) dSd\kappa. \tag{9}$$

The full form of our chosen strain energy density function is thus

$$W(I_1, I_4) = \frac{\mu}{2}(I_1 - 3) + \frac{\mu}{4\pi} \int_0^\infty \int_0^\pi \int_0^\pi f(\mathbf{a}_0, \kappa)\kappa$$
$$\left((\mathbf{a}_0^T \mathbf{C} \mathbf{a}_0) + 2(\mathbf{a}_0^T \mathbf{C} \mathbf{a}_0)^{-\frac{1}{2}} - 3 \right) \sin\phi d\phi d\psi d\kappa, \tag{10}$$

where the integration over the spherical surface S has been written explicitly in its inclination ϕ and azimuthal ψ components and the integration over κ has been specified over the range $[0, \infty)$.

We consider incompressible materials only and thus the second Piola-Kirchhoff tensor is calculated as

$$\mathbf{S} = 2\frac{\partial W}{\partial \mathbf{C}} - p\mathbf{C}^{-1}, \tag{11}$$

where the second term accounts for the incompressibily constraint and $p = -\frac{1}{3}tr\sigma$, with σ the Cauchy (true) stress tensor.

Substituting Eq. (10) into (11), we get

$$\mathbf{S} = 2\frac{\partial W_m}{\partial I_1}\mathbf{I} + \frac{1}{2\pi} \int_\kappa \int_S f(\mathbf{a}_0, \kappa) \frac{\partial w_f}{\partial I_4} \mathbf{a}_0 \otimes \mathbf{a}_0 dSd\kappa - p\mathbf{C}^{-1}$$
$$= \mu\mathbf{I} + \frac{\mu}{4\pi} \int_\kappa \int_S f(\mathbf{a}_0, \kappa)\kappa \left(1 + I_4^{-\frac{3}{2}} \right) \mathbf{a}_0 \otimes \mathbf{a}_0 dSd\kappa - p\mathbf{C}^{-1}. \tag{12}$$

The first Piola-Kirchhoff stress tensor $\mathbf{P}$ is obtained from $\mathbf{S}$ as $\mathbf{P} = \mathbf{FS}$. Taking into account Equation (12), we have

$$\mathbf{P} = \mu\mathbf{F} + \frac{\mu}{4\pi} \int_\kappa \int_S f(\mathbf{a}_0, \kappa)\kappa \left(1 + I_4^{-\frac{3}{2}} \right) \mathbf{F}\mathbf{a}_0 \otimes \mathbf{a}_0 dSd\kappa - p\mathbf{F}^{-T}. \tag{13}$$

3. Plane stress

Given that many applications of highly stretchable fiber-reinforced polymers are in the form of thin sheets [39–41] and that tissues as well can be modeled as such [16,23,25], we restrict our analysis to this structural configuration and thus, following [42], to plane stress conditions. It is worth to remark here that the assumption of plane stress is key for all the derivations and results presented in this work. Extension to axisymmetric and/or generic 3D configurations is thus not straightforward and will require further work to explore it. The results shall thus be considered as applicable only to thin sheets, for which assumptions of plane stress reasonably apply. We assume that the thin sheet belongs to the plane where the unit vectors $\mathbf{e}_1, \mathbf{e}_2$ lie, and that $\mathbf{e}_3$ coincides with the thickness direction and denotes the normal to the plane of planar stress state. To enforce the state of plane stress we require that

$$\mathbf{e}_3^T \mathbf{a}_0 = 0 \tag{14}$$

for any family of fibers, which restricts the fiber orientations to $\phi = \frac{\pi}{2}$ and thus reduces Eq. (1) to

$$\mathbf{a}_0 = \cos\psi\mathbf{e}_1 + \sin\psi\mathbf{e}_2. \tag{15}$$

In agreement with the assumption of plane stress in the plane $1-2$, it

holds that $P_{33} = 0$ and $P_{\alpha\beta,3} = 0$ with $\alpha,\beta = 1,2$, where the comma stands for the partial derivative. As $F_{\alpha 3} = F_{3\alpha} = 0$ with $\alpha = 1,2$, the component F_{33} is equal to the out-of-plane stretch $\lambda_3 = \lambda$, i.e. $F_{33} = \lambda$. By calling J the jacobian of the deformation gradient restricted to the plane of planar stress, i.e. $J = det(F_{\alpha\beta})$ with $\alpha, \beta = 1, 2$, the satisfaction of the incompressibility constraint requires that $J = \lambda^{-1}$ and $C_{33}^{-1} = \lambda^{-2}$, which implies that $P_{\alpha 3} = P_{3\alpha} = 0$. The equilibrium equations in the absence of body forces are thus reduced to $P_{\alpha\beta,\beta} = 0\alpha, \beta = 1, 2$. Inserting the expression $C_{33}^{-1} = \lambda^{-2}$ into the third of Eq. (12), and taking into account the condition of Eq. (14), we obtain the expression of p as a function of λ as $p = \mu\lambda^2$. Thanks to the latter equality, noting that $JF_{\beta\alpha}^{-1} = \varepsilon_{\alpha\gamma}\varepsilon_{\beta\nu}F_{\gamma\nu} = \varepsilon_{\alpha\gamma}\varepsilon_{\beta\nu}y_{\gamma,\nu}$, and recalling that $F_{\alpha\beta} = y_{\alpha,\beta}$, the plane components of the first Piola-Kirchhoff stress tensor can be written as (in indicial notation, all indices vary in the range $1,2$)

$$P_{\alpha\beta} = \mu\left(y_{\alpha,\beta} + y_{\alpha,\nu} \frac{1}{4\pi}\int_\kappa \int_S f(\mathbf{a}_0, \kappa)\kappa\left(1 + \lambda_f^{-3}\right)a_\nu^0 a_\beta^0 dSd\kappa - \lambda^3 \varepsilon_{\alpha\gamma}\varepsilon_{\beta\nu}y_{\gamma,\nu} \right), \tag{16}$$

where the term $y_{\alpha,\nu}$ has been factored out of the integral as it does not depend on the fiber orientation. Using Eq. (16), the traction vector t_α over a surface of normal n_β can be evaluated as $t_\alpha = P_{\alpha\beta}n_\beta$. Finally, the plane stress quilibrium equations are

$$y_{\alpha,\beta\beta} + y_{\alpha,\nu\beta}\frac{1}{4\pi}\int_\kappa \int_S f(\mathbf{a}_0, \kappa)\kappa\left(1 + \lambda_f^{-3}\right)a_\nu^0 a_\beta^0 dSd\kappa$$
$$+ y_{\alpha,\nu}\frac{1}{4\pi}\int_\kappa \int_S f(\mathbf{a}_0, \kappa)\kappa\left(1 + \lambda_f^{-3}\right)_{,\beta}a_\nu^0 a_\beta^0 dSd\kappa - \lambda^3 \varepsilon_{\alpha\gamma}\varepsilon_{\beta\nu}y_{\gamma,\nu\beta}$$
$$= 0, \tag{17}$$

which are solved under the condition of traction-free crack faces

$$\left(y_{\alpha,\beta} + y_{\alpha,\nu}\frac{1}{4\pi}\int_\kappa \int_S f(\mathbf{a}_0, \kappa)\kappa\left(1 + \lambda_f^{-3}\right)a_\nu^0 a_\beta^0 dSd\kappa - \lambda^3 \varepsilon_{\alpha\gamma}\varepsilon_{\beta\nu}y_{\gamma,\nu} \right)n_\beta$$
$$= 0 \text{ at } x_1 \leq 0, x_2 = 0. \tag{18}$$

4. Asymptotic boundary value problem and its solution

4.1. Asymptotic boundary value problem

We analyze the case of an edge crack lying on the x_1 axis, as depicted in Fig. 1b[1], and we focus on the determination of stress and deformation fields in the vicinity of the crack tip under the condition of traction-free crack faces. We will determine the crack tip fields up to a set of constants, whose value depends on the applied far-field boundary conditions.

Referring to crack tip polar coordinates $r - \theta$ as shown in Fig. 1b, we seek solutions to the equilibrium equations (17) such that the in-plane stretches are singular, i.e. $\lambda_\alpha = O(r^{m-1})$ as $r \to 0$, with $-\pi \leq \theta \leq \pi$, $\alpha, \beta = 1, 2$ and $m \in \mathbb{R}$. Following [43,42], we also require that the out-of-plane stretch behaves asymptotically as $\lambda = J^{-1} = O(r^q)$ as $r \to 0$, with $-\pi \leq \theta \leq \pi$ and $q \in \mathbb{R}$, which simplifies the asymptotic form of the equilibrium equations by forcing some components of the deformation gradient to be unbounded. In particular, the fiber stretch $\lambda_f \to \infty$ and thus $\lambda \to 0$ for $r \to 0$. Thanks to the assumptions made, the asymptotic solution must satisfy

---

[1] Notice that in Fig. 1b the fiber orientation angle ψ is defined with respect to the axis $\mathbf{e}_1$ of undeformed coordinates x_1 in agreement with the spherical coordinates employed in Eq. (1) and defined in Fig. 1a. When working with a 2D system, it is possible to define the fiber orientation angle with respect to the axis $\mathbf{e}_2$ of undeformed coordinates x_2. This is the approach taken in [5], where such angle is referred to as ϕ. Observe that $\phi = \frac{\pi}{2} - \psi$ and thus $\cos\psi = \sin\phi$, $\sin\psi = \cos\phi$.

$$y_{\alpha,\beta\beta} + y_{\alpha,\nu\beta}\frac{1}{4\pi}\int_\kappa\int_S f(\mathbf{a}_0,\kappa)\kappa a_\nu^0 a_\beta^0 dS d\kappa = 0, \tag{19}$$

subject to

$$\left(y_{\alpha,\beta} + y_{\alpha,\nu}\frac{1}{4\pi}\int_\kappa\int_S f(\mathbf{a}_0,\kappa)\kappa a_\nu^0 a_\beta^0 dS d\kappa\right)n_\beta|_{\theta=\pm\pi} = 0. \tag{20}$$

4.2. Transformation to canonical form

The solution to Eq. (19) has been already discussed in detail in [5] for the cases of one and two families of perfectly aligned fibers oriented at different angles, here we will recall only the key concepts important to understand the results presented. In analogy with anisotropic linearly elastic antiplane crack problems [44], we introduce the following notation:

$$c_{44} = 1 + \frac{1}{4\pi}\int_\kappa\int_\phi f(\psi,\kappa)\kappa\sin^2\psi d\psi d\kappa$$

$$c_{45} = \frac{1}{4\pi}\int_\kappa\int_\phi f(\psi,\kappa)\kappa\sin\psi\cos\psi d\psi d\kappa \tag{21}$$

$$c_{55} = 1 + \frac{1}{4\pi}\int_\kappa\int_\phi f(\psi,\kappa)\kappa\cos^2\psi d\psi d\kappa,$$

by which the asymptotic governing equations (19) and boundary conditions (20) are reduced to the following system of equations:

$$\begin{cases} c_{55}y_{\alpha,11} + 2c_{45}y_{\alpha,12} + c_{44}y_{\alpha,22} = 0 \\ (c_{45}y_{\alpha,1} + c_{44}y_{\alpha,2})|_{\theta=\pm\pi} = 0. \end{cases} \tag{22}$$

By introducing the linear transformation $\eta_i = A_{ij}x_j, \frac{\partial\eta_i}{\partial x_j} = A_{ij}$ with

$$\mathbf{A} = \begin{bmatrix} \sqrt{\dfrac{c_{44}}{c_{44}c_{55} - c_{45}^2}} & -\dfrac{c_{45}}{c_{44}}\sqrt{\dfrac{c_{44}}{c_{44}c_{55} - c_{45}^2}} \\ 0 & \sqrt{\dfrac{1}{c_{44}}} \end{bmatrix}, \tag{23}$$

Eq. (22) are transformed, in the plane $\eta_1 - \eta_2$, to their canonical form:

$$\begin{cases} \dfrac{\partial^2 y_\alpha}{\partial\eta_1^2} + \dfrac{\partial^2 y_\alpha}{\partial\eta_2^2} = 0 & \rho = (\eta_1^2 + \eta_2^2)^{\frac{1}{2}} \to 0 \\ \dfrac{\partial y_\alpha}{\partial\eta_2} = 0 & \eta_1 \le 0, \ \eta_2 = 0 \text{ or } \varphi = \tan^{-1}\left(\dfrac{\eta_2}{\eta_1}\right) = \pm\pi, \end{cases} \tag{24}$$

in which we dropped the comma notation for partial derivatives to highlight the change of variables and introduced a system $\rho - \varphi$ of crack tip polar coordinates in the plane $\eta_1 - \eta_2$. It is worth noting that the canonical form 24 correspond to the asymptotic plane stress governing equations for a crack in an isotropic Neo-Hookean sheet [42]. Given the solution $\widetilde{y}_\alpha$ of the isotropic problem [42] in the coordinates ρ, ψ

$$\widetilde{y}_\alpha = \sum_m \rho^{\frac{m}{2}}\widetilde{\nu}_m(\varphi) \quad as \quad \rho \to 0 \tag{25}$$

with

$$\widetilde{\nu}_m = \begin{cases} p_m\sin\left(\dfrac{m}{2}\varphi\right) & for \quad m = 2n-1 \\ q_m\cos\left(\dfrac{m}{2}\varphi\right) & for \quad m = 2n \end{cases} \quad with \quad n \in \mathbb{N}, n > 0, \tag{26}$$

The solution y_α of the anisotropic problem in the coordinates r, θ can found as

$$y_\alpha = \sum_m r^{\frac{m}{2}}\left((A_{11}\cos(\theta) + A_{12}\sin(\theta))^2 + (A_{22}\sin(\theta))^2\right)^{\frac{m}{4}}\nu_m(\theta) \quad as \quad \rho \to 0 \tag{27}$$

with

$$\nu_m = \begin{cases} p_m\sin\left(\dfrac{m}{2}tan^{-1}\left(\dfrac{A_{22}\sin(\theta)}{A_{11}\cos(\theta) + A_{12}\sin(\theta)}\right)\right) & for \quad m = 2n-1 \\ q_m\cos\left(\dfrac{m}{2}tan^{-1}\left(\dfrac{A_{22}\sin(\theta)}{A_{11}\cos(\theta) + A_{12}\sin(\theta)}\right)\right) & for \quad m = 2n \end{cases} \quad with \quad n \\ \in \mathbb{N}, n > 0. \tag{28}$$

5. Crack tip integrals

5.1. Asymptotically path-independent interaction integral

Following [5], it is possible to evaluate all the crack tip parameters by introducing asymptotically path-independent interaction integrals of the type

$$I^{y_\alpha}(x_i) = \lim_{\Gamma\to 0}\int_\Gamma\left(P_{\alpha j}y_j^{aux}n_1 - P_{\alpha j}y_{,1}^{aux}n_j - P_j^{aux}y_{\alpha,1}n_j\right)d\Gamma, \quad \alpha = 1, 2. \tag{29}$$

In the previous equation, y^{aux} is an auxiliary field satisfying the asymptotic boundary value equations and P_j^{aux} is the conjugated auxiliary stress evaluated as $P_j^{aux} = y_{,k}^{aux}D_{kj}$, where D_{kj} are the components of the matrix

$$\mathbf{D} = \begin{bmatrix} c_{55} & c_{45} \\ c_{45} & c_{44} \end{bmatrix} \tag{30}$$

It has been shown [5] that the latter is related to the asymptotic interaction integral $\widetilde{I}^{y_\alpha}(\eta_i)$ in the scaled coordinate system $\eta_1 - \eta_2$ by $P^{y_\alpha}(x_i) = \sqrt{c_{44}}\,\widetilde{I}^{y_\alpha}(\eta_i)$. As in the scaled coordinate system the problem is equivalent to that of an isotropic Neo-Hookean material, it has been shown [4] that

$$\begin{cases} I^{y_\alpha}(x_i) = \sqrt{c_{44}}\,\dfrac{\pi}{2}\mu p_\alpha & for \quad \widetilde{y}^{aux} = \rho^{\frac{1}{2}}\sin\dfrac{\varphi}{2} \\ I^{y_\alpha}(x_i) = -2\sqrt{c_{44}}\,\pi\mu q_\alpha & for \quad \widetilde{y}^{aux} = \ln\rho \end{cases} \tag{31}$$

where p_α, q_α, with $\alpha = 1, 2$ are parameters whose values depend on far-field boundary conditions.

5.2. Numerical realization of crack tip integrals

We realize the crack tip integrals introduced in Section 5.1 in the FEM model (later presented in Section 6.1) in the form of domain integrals [5]. Given a test function g representing an arbitrary virtual displacement of the crack tip, the crack tip integrals have the following domain-integral form:

$$I^{y_\alpha} = \int_A\left(-P_{\alpha j}y_j^{aux}\frac{\partial g}{\partial x_1} + \left(P_{\alpha j}y_{,1}^{aux}n_j + P_j^{aux}y_{\alpha,1}n_j\right)\frac{\partial g}{\partial x_1}\right)dA. \tag{32}$$

It is possible to show [5] that the integrand of the term $\int_A(\cdot)_{,j}gdA$ is asymptotically divergence-free, i.e. if the contours are taken in the region of dominance of the asymptotic crack tip fields. The function g is assumed to be $\frac{r_0-r}{r_0}$, where r_0 is the radius of the circular path of the corresponding contour integral, such that $g = 0$ on the domain boundary and $g = 1$ at the crack tip. Further details can be found in [5].

5.3. Coordinate-based method

Similar to [5], a coordinate-based approach in the form of a P_k contour integral [45] is used to validate the results of the interaction integrals. Accordingly, the coefficients of the asymptotic expansion are evaluated as

$$p_1 = \frac{y_1^n(r_0, \pi) - y_1^n(r_0, -\pi)}{(4A_{11}r_0)^{\frac{1}{2}}} \qquad p_2 = \frac{y_2^n(r_0, \pi) - y_2^n(r_0, -\pi)}{(4A_{11}r_0)^{\frac{1}{2}}} \qquad q_1$$
$$= \frac{y_1^n(r_0, 0)}{A_{11}r_0}, \tag{33}$$

where $y_i^n(r_0, \theta), i = 1, 2$ are the deformed coordinates at the point (r_0, θ) of the Finite Element mesh.

6. Numerical analysis and results

6.1. FEM model

The crack tip fields are evaluated for an edge crack in an initially rectangular strip. The strip has dimensions $L_0 \times H_0$ with $L_0 = 4H_0$ and the initial length of the crack is $0.25L_0$. The strip is subject to far-field Mode I boundary conditions of the type $y_1 = x_1|_{x_2 = \pm \frac{H_0}{2}}$, $y_2 = \lambda_S x_2|_{x_2 = \pm \frac{H_0}{2}}$, where λ_S is the far-field stretch in the x_2 direction. The stiffness of the matrix μ is equal to 1 MPa while the fiber-to-matrix stiffness ratio is a parameter of the analysis. The governing Eq. (18) are solved using the Finite Element Method (FEM) with an in-house code. Implementation details can be found in [5]. The domain is discretized using 8-node quadrilateral elements with 4 four Gauss integration points and the smallest element at the crack tip has a side length of about $10^{-5}H_0$.

6.2. Continuous distributions of fiber

Incorporation of data on fiber orientation in structural models of tissues requires the formulation of a probability model [46–51], i.e. the identification of the statistical distribution $f(\mathbf{a}_0, \kappa)$ that best represents the experimental measurements. In the absence of any prior knowledge, a maximum-entropy distribution should be chosen [52], such as the *Gaussian* distribution for data defined on linear domains or the *π-periodic von Mises* distribution for data defined on circular (periodic) domains [53]. While both distributions are 2-parameter bell-shaped distributions, the *π*-periodicity of the *von Mises* distribution takes into account the natural symmetry of a physical distribution of long continuous fibers and it is thus the best choice to incorporate data on fiber orientation into our material model. Sacks and co-workers obtained a good fit of data of fiber distribution in bovine pericardium and porcine aortic valve obtained using small angle light scattering (SALS) through application of the *Gaussian* distribution [49,50] and used it further in modeling the mechanical response of these tissues [50,54]. The *von Mises* distribution was shown in [48] to be a good fit for data gathered in [46,47] on fibril orientation in adult rabbit medial collateral ligament, and in [51] to accurately model the distribution of collagen fibers in abdominal aortic aneurysms, measured with polarized light microscopy in combination with the universal stage. Although both distributions have found application in the experimental literature, we will focus our attention on the *π-periodic von Mises* distribution, as it represents the best probability model for data defined on circular domains such as fiber orientations.

6.2.1. Von Mises distribution

We analyze a Neo-Hookean matrix reinforced by fibers with orientations distributed according to the standard *π-periodic von Mises* distribution $f_{vM}(\psi)$

$$f_{vM}(\psi) = \frac{e^{b\cos(2(\psi - \psi_0))}}{2\pi I_0(b)}, \tag{34}$$

where

$$I_0(b) = \frac{1}{\pi} \int_0^\pi e^{b\cos\psi} d\psi \tag{35}$$

is the modified Bessel function of the first kind of order zero with

parameter b. Taking into account the normalization condition and considering a constant κ, the distribution $f(\psi)$ of fiber orientations is described by

$$f(\psi) = \frac{f_{vM}(\psi)}{\int_0^\pi f_{vM}(\psi) d\psi} = \frac{e^{b\cos(2(\psi - \psi_0))}}{\int_0^\pi e^{b\cos(2(\psi - \psi_0))} d\psi}. \tag{36}$$

In Eq. (36), the parameter ψ_0 represents the main direction of the fiber family while b controls the dispersion around the main direction ψ_0. Lower values of b correspond to more dispersed fibers, while higher values b corresponds to fibers whose orientations are concentrated around the main direction ψ_0. The corresponding effect on the shape of the distribution funtion $f(\psi)$ in shown in Fig. 2.

The evaluation of the contribution of the fourth invariant to the strain energy density (Eq. (9)) requires, for constant κ, an integration of the individual fiber contribution weighted by the orientation distribution $f(\psi)$ over all possible orientations. In the case of plane stress, taking into account condition (14), Eq. (9) takes the form

$$W(I_4(\psi)) = \frac{1}{2\pi} \int_0^\pi f(\psi)w(I_4(\psi)) d\psi, \tag{37}$$

which can be evaluated numerically using a 12-point Gauss quadrature rule according to

$$W(I_4(\psi)) = \frac{1}{4} \sum_{n=1}^{12} \omega_n f\left(\frac{\pi}{2}(1 + \xi_n)\right) w\left(I_4\left(\frac{\pi}{2}(1 + \xi_n)\right)\right), \tag{38}$$

where ω_n and ξ_n are respectively the Gauss points and weights on the unit interval. The coefficients of Eq. (21) become in plane stress

$$\begin{aligned} c_{44} &= 1 + \frac{\kappa}{2\pi} \int_0^\pi f(\psi)\sin^2\psi d\psi \\ c_{45} &= \frac{\kappa}{2\pi} \int_0^\pi f(\psi)\sin\psi\cos\psi d\psi \\ c_{55} &= 1 + \frac{\kappa}{2\pi} \int_0^\pi f(\psi)\cos^2\psi d\psi, \end{aligned} \tag{39}$$

which are as well evaluated using a 12-point Gauss quadrature rule. In Fig. 3, it is shown the effect of the distribution parameters b and ψ_0 on the coefficients c_{44}, c_{45}, c_{55} of transformation 21.

For a given value of b, it is possible to observe that c_{55} decreases for increasing values of ψ_0, reaching its maximum at $\psi_0 = 0$ and its minimum at $\frac{\pi}{2}$. c_{44} shows the opposite behavior, increasing for increasing values of ψ_0, with the maximum at $\psi_0 = \frac{\pi}{2}$ and its minimum at 0. On the other hand, the coefficient c_{45} reaches its peak value at $\frac{\pi}{4}$ and is equal to zero both at 0 and $\frac{\pi}{2}$. Finally, observe that for $b > 5$ the dependency on the value of b is practically non-existent, which implies that the behavior of the *von Mises* distribution is for practical purposes undistinguishable from the case of perfectly aligned fibers as $c_{ij}(b > 5) \sim c_{ij}(b \to \infty)$, where $b \to \infty$ corresponds to the case of perfectly aligned fibers (see Fig. 3a). To investigate the effect of fiber dispersion, b should be chosen < 5, with most of the variability concentrated in the range $(0, 3)$. As we are on the other hand interested in investigating the effect of the main fiber orientation on the crack tip fields, we will set b to a value higher than 5.

We select in particular $b = 10$ and analyze 3 different cases in which the main fiber orientation ψ_0 is respectively equal to $0, \frac{\pi}{4}, \frac{\pi}{2}$, with an applied stretch $\lambda_S = 2$ and fiber-to-matrix stiffness ratio $\kappa = 2$. As explained in [5], to have an open crack in the case of large deformation, the leading order term $p_2\rho^{\frac{1}{2}}$ of the asymptotic expansion of y_2 must be the dominant one, i.e. it must hold that $p_2\rho^{\frac{1}{2}} >> q_2\rho$, where $q_2\rho$ is the second order term of the expansion. Our numerical analysis confirms that q_2 is approximately 0 in all examples considered and it is thus not reported. We thus evaluate the coefficients p_1, q_1, p_2 of the leading terms of the asymptotic expansion using interaction integrals (denoted by Ξ^I) and the coordinate-based method (denoted by Ξ^C). Results are reported in
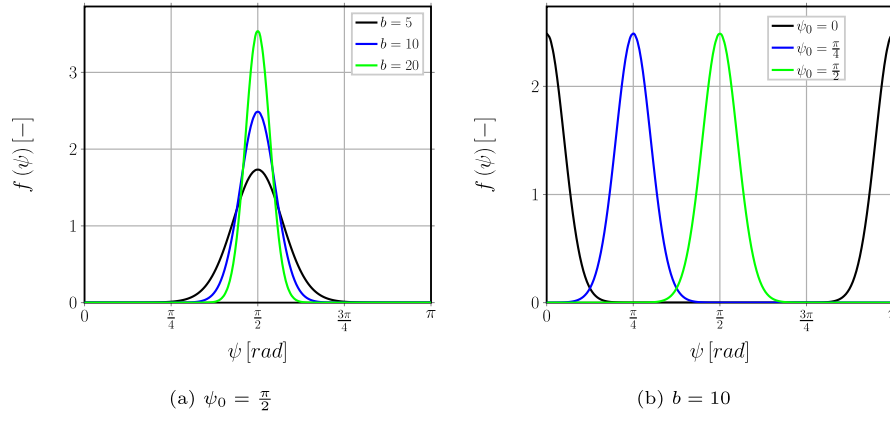
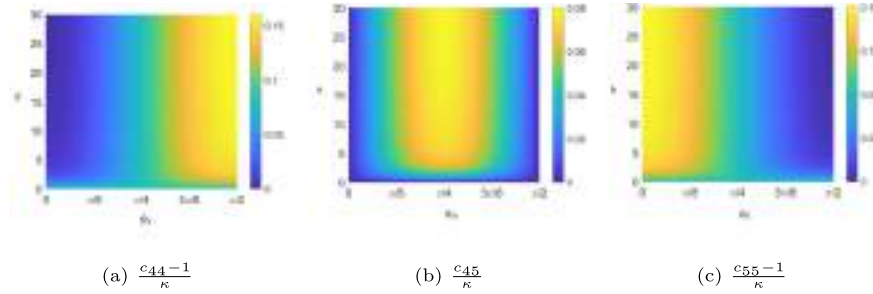Fig. 2. Effect of the parameters b and ψ_0 on the shape of the distribution function $f(\psi)$.

(a) $\psi_0 = \frac{\pi}{2}$

(b) $b = 10$

(a) $\frac{c_{44}-1}{\kappa}$

(b) $\frac{c_{45}}{\kappa}$

(c) $\frac{c_{55}-1}{\kappa}$

Fig. 3. Effect of the parameters b and ψ_0 on the coefficients c_{44}, c_{45}, c_{55} of transformation 21.

Table 1. The agreement between the methods is good (to the second and often to third decimal value) and thus in the following we will use only the values computed with the interaction integrals to evaluate the analytical solution previously determined.

In Fig. 4, it is possible to observe the good agreement between FEM results and analytical predictions for both the circumferential variation (at $\frac{r}{H_0} = 10^{-4}$) and radial variation (at $\theta = \pi$) of the deformed coordinates y_1 and y_2. For $\psi_0 = 0, \frac{\pi}{2}$, notice that $p_1 = 0$ (see Table 1) and $c_{45} = 0$ (see Fig. 3), which imply that in Eq. (23) $A_{11} = \frac{1}{\sqrt{c_{55}}}, A_{12} = 0$, $A_{22} = \frac{1}{\sqrt{c_{44}}}$ and thus that from Eqs. (25) and (26) we have $y_1 \sim q_1 \rho \cos \psi = q_1 \eta_1 = \frac{q_1}{\sqrt{c_{55}}} r \cos \theta$. This is evident, for $\psi_0 = 0, \frac{\pi}{2}$, from the symmetry of $y_1(\theta)$ in Fig. 4a and the $y_1 \sim r$ behavior in Fig. 4c.

The previous observations imply that, under far-field Mode I boundary conditions $y_1 = x_1|_{x_2=\frac{H_0}{2}}, y_2 = \lambda_S x_2|_{x_2=\frac{H_0}{2}}$, the crack tip experiences for $\psi_0 = 0, \frac{\pi}{2}$ a pure Mode I deformation similarly to what occurs for an isotropic Neo-Hookean material. However, notice that the behavior is not isotropic in the region of dominance of the asymptotic solution as $c_{44} \neq c_{55}$ and thus Eq. (22) becomes $c_{55} y_{\alpha,11} + c_{44} y_{\alpha,22} = 0$. Recalling the matrix D introduced in Eq. (30), in the region of asymptotic dominance the first Piola-Kirchhoff and the Cauchy stress tensors are $\mathbf{P} = \mu \mathbf{F} \mathbf{D}$ and $\sigma = \mu \mathbf{F} \mathbf{D} \mathbf{F}^T$. For $\psi_0 = 0, \frac{\pi}{2}$, with $c_{45} = 0, c_{44} \neq c_{55}$, they

can be expressed respectively as $\mathbf{P} = \mu \left[c_{55} \mathbf{y}_{,1} | c_{44} \mathbf{y}_{,2} \right]$ and $\sigma = \mu \left(c_{55} \mathbf{y}_{,1} \mathbf{y}_{,1}^T + c_{44} \mathbf{y}_{,2} \mathbf{y}_{,2}^T \right)$, where $\mathbf{y} = [y_1 \ y_2]^T$ is the position vector of the generic point in the deformed configuration. Thus, for an isotropic deformation field of the type $y_i = \gamma x_i$ the resultant stress field is anisotropic and for $\psi_0 = 0, \frac{\pi}{2}$ the material in the region of asymptotic dominance behaves anisotropically. This result is confirmed by the deformed configurations of the crack tips as shown in Fig. 5. The deformed configuration is symmetric with respect to the crack line $\theta = 0$ for $\psi_0 = 0, \frac{\pi}{2}$ (pure Mode I at the crack tip for far-field Mode I boundary conditions, as $c_{45} = 0$), but the shape is different (anisotropic response). In comparison, for $\psi_0 = \frac{\pi}{8}, \frac{\pi}{4}, \frac{3\pi}{8}$, the deformed configuration is neither symmetric (Mixed Mode at the crack tip for far-field Mode I boundary conditions, as $c_{45} \neq 0$) nor similar to each other (anisotropic response).

Fig. 4b shows that at the crack faces ($\theta = \pm \pi$) the value of y_2 is the lowest for $\psi_0 = 0$ and the highest for $\psi_0 = \frac{\pi}{2}$. A *von Mises* distribution of fibers centered on $\psi_0 = \frac{\pi}{2}$, i.e. normal to the direction of crack propagation, promotes the maximum opening of the crack, as fiber stretch occurs on average normal to crack faces (recall the decomposition of the deformation gradient adopted in the current model following [1–3]) and thus acts to open the crack. On the other hand, for a distribution centered on $\psi_0 = 0$, i.e. parallel to the direction of crack propagation, fiber stretch occurs on average parallel to crack faces and thus does not

Table 1

Asymptotic expansion coefficients p_1, q_1, p_2 in the *von Mises* distribution case evaluted using interaction energy integrals, denoted by Ξ^I, and the coordinate based method, denoted by Ξ^C. Main fiber orientation $\psi_0 = 0, \frac{\pi}{4}, \frac{\pi}{2}$, fiber dispersion $b = 5$, applied stretch $\lambda_S = 2$, ratio of fiber to matrix stiffness $\kappa = 10$.

	$\psi_0 = 0$			$\psi_0 = \frac{\pi}{4}$			$\psi_0 = \frac{\pi}{2}$		
	p_1	p_2	q_1	p_1	p_2	q_1	p_1	p_2	q_1
Ξ^I	0.000	1.204	0.589	0.061	1.567	0.644	0.000	1.393	0.727
Ξ^C	0.000	1.203	0.585	0.061	1.599	0.640	0.000	1.377	0.723
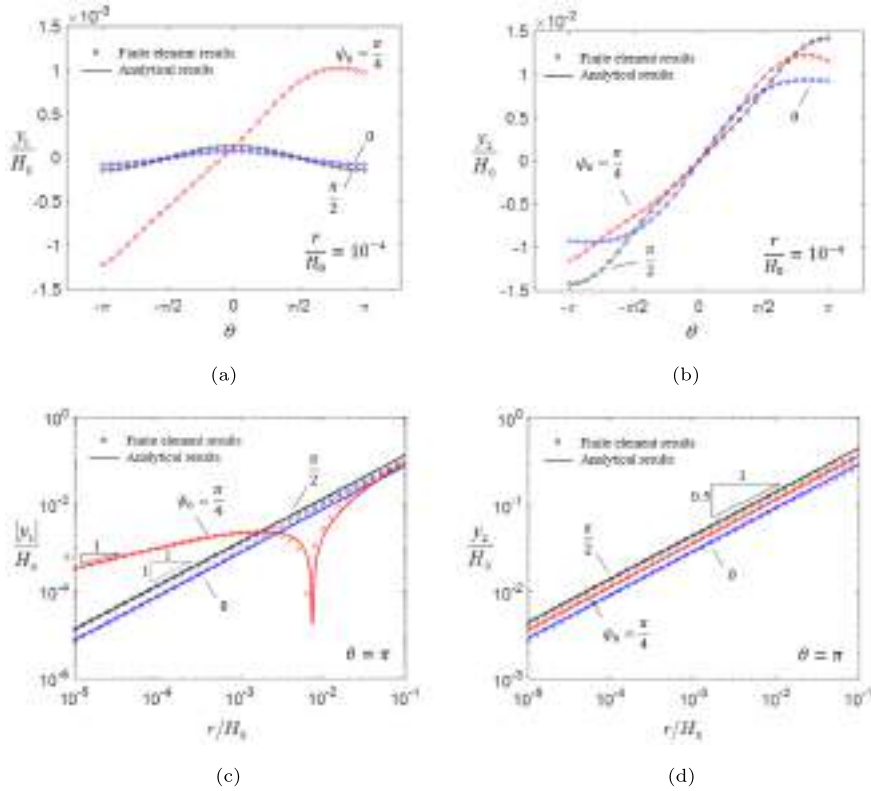
Fig. 4. Circumferential (11, 12) and radial (13, 14) variation of normalized deformed coordinates $\frac{y_1}{H_0}$ (11, 13) and $\frac{y_2}{H_0}$ (12, 14) for main fiber orientation $\psi_0 = 0, \frac{\pi}{4}, \frac{\pi}{2}$, fiber dispersion $b = 5$, applied stretch $\lambda_S = 2$, ratio of fiber to matrix stiffness $\kappa = 10$. Open circles correspond to FEM results, solid line to the analytical prediction based on the results of Eq. (27).

affect their deformation, which is in this case driven by the matrix-dominated shear (the second component of the deformation gradient decomposition of [1–3]).

It was shown in [5] that, in the case of a single family of fibers oriented at $\psi = 0$, there exists a cusp in the variation of y_1 with respect to θ for fiber-to-matrix stiffness ratio $\kappa > 1$. No such cusp can be observed for y_1 in Fig. 4a in the case of a fiber distribution centered on $\psi_0 = 0$. This means, interestingly, that the effect of eigenmodes higher than the second is negligible in the case of a distribution of fibers.

For $\psi_0 = \frac{\pi}{4}$, the slope of y_1 in Fig. 4c is equal to $\frac{1}{2}$, differently from the cases $\psi_0 = 0, \frac{\pi}{2}$. This is due to the fact that $p_1 \neq 0$ (see Table 1) and thus the first order eigenmode plays an important role in the behavior of y_1. In particular, $y_1 \sim p_1 \rho^{\frac{1}{2}} - q_1 \rho \sim p_1 \sqrt{A_{11}} r^{\frac{1}{2}} - q_1 A_{11} r$ which implies that $y_1 \sim 0$ at $r \sim \frac{p_1^2}{q_1^2 A_{11}}$, corresponding to the drop in Fig. 4c.

In Fig. 6, the components P_{21} and P_{22} of the first Piola-Kirchhoff stress and σ_{22} of the Cauchy stress tensor are reported. It can be observed that the agreement between FEM results and analytical predictions is good. P_{21} (Fig. 6a) has its extrema in correspondence of the crack faces at $\theta = \pm \pi$, P_{22} (Fig. 6b) reaches its maximum value always in the range $-\frac{\pi}{2} < \theta < \frac{\pi}{2}$ and is equal to 0 for $\theta = \pm \pi$, verifying the condition of traction-free crack faces. Notice that for $\psi_0 = 0, \frac{\pi}{2}$, P_{21} is an odd function of θ while P_{22} is an even function of θ. Given that $c_{45} = 0$ (see Fig. 3c) for both $\psi_0 = 0, \frac{\pi}{2}$, we have

$$P_{21} = -\frac{1}{2}\mu p_2 \sqrt{c_{55}} \rho^{-\frac{1}{2}} \sin\left(\frac{\varphi}{2}\right) \qquad P_{22} = \frac{1}{2}\mu p_2 \sqrt{c_{44}} \rho^{-\frac{1}{2}} \cos\left(\frac{\varphi}{2}\right) \qquad (40)$$

with

$$\rho = \frac{1}{\sqrt{c_{55}}} r \cos\theta \sqrt{1 + \frac{c_{55}}{c_{44}} \tan^2\theta} \qquad \varphi = \tan^{-1}\left(\sqrt{\frac{c_{55}}{c_{44}}} \tan\theta\right), \qquad (41)$$

which means that φ is a monotonic function of θ, ρ is an even function of

θ (as $\cos\theta, \tan^2\theta, \sqrt{1 + \frac{c_{55}}{c_{44}} \tan^2\theta}$ are all even), and thus P_{21} is an odd function of θ (product of even function $\rho^{-\frac{1}{2}}$ with odd function $\sin\left(\frac{\varphi}{2}\right)$) and P_{22} is an even function of θ (product of even function $\rho^{-\frac{1}{2}}$ with even function $\sin\left(\frac{\varphi}{2}\right)$). Notice that, on the other hand, for $\psi_0 = \frac{\pi}{4}$ no symmetry is present.

It was observed in [5] that the extrema θ_e of σ_{22} satisfy the relationship $\theta_e + \psi_0 = 0, \pm\frac{\pi}{2}, \pm\pi, \cdots$. Interestingly, it remains valid also in the case of a *von Mises* distribution of fiber orientations (see Fig. 6c) with ψ_0 the main direction of alignment of the fibers. Finally, Fig. 6d confirms, at $\theta = 0$, the expectation that $\sigma_{22} \sim r^{-1}$ for $r \rightarrow 0$ and that $\frac{\sigma_{22}}{\mu} = \lambda_S^2 - \frac{\lambda_S^2 \kappa}{2\pi} \int f(\psi)\left(1 - \lambda_f^{-3}\right)\lambda_f^2 \cos^2\psi d\psi$ for $r \rightarrow \infty$.

6.3. Asymptotic isotropy at the crack tip

Recalling transformation 21, if the conditions $c_{45} = 0, c_{55} = c_{44}$ are satisfied, the governing equations are reduced to those of the isotropic problem *without* resorting to the canonical transformation. Furthermore $\mathbf{P} = c_{44}\mu\mathbf{F}$, which implies that, in the vicinity of the crack tip, the material behaves isotropically with a stiffness that is a multiple $c_{44}\mu$ of the matrix stiffness. We thus refer to this regime as *asymptotic isotropy* and we look for fiber distributions such that the conditions for its existence are satisfied.

6.3.1. Discrete case

Consider a discrete distribution of n fibers placed at regular intervals δ such that $\delta \in [0, \pi)$ with constant κ and the first of such fibers placed at a generic angle ψ (referring to the geometry of Fig. 1b). For this configuration, the conditions of asymptotic isotropy can be written as
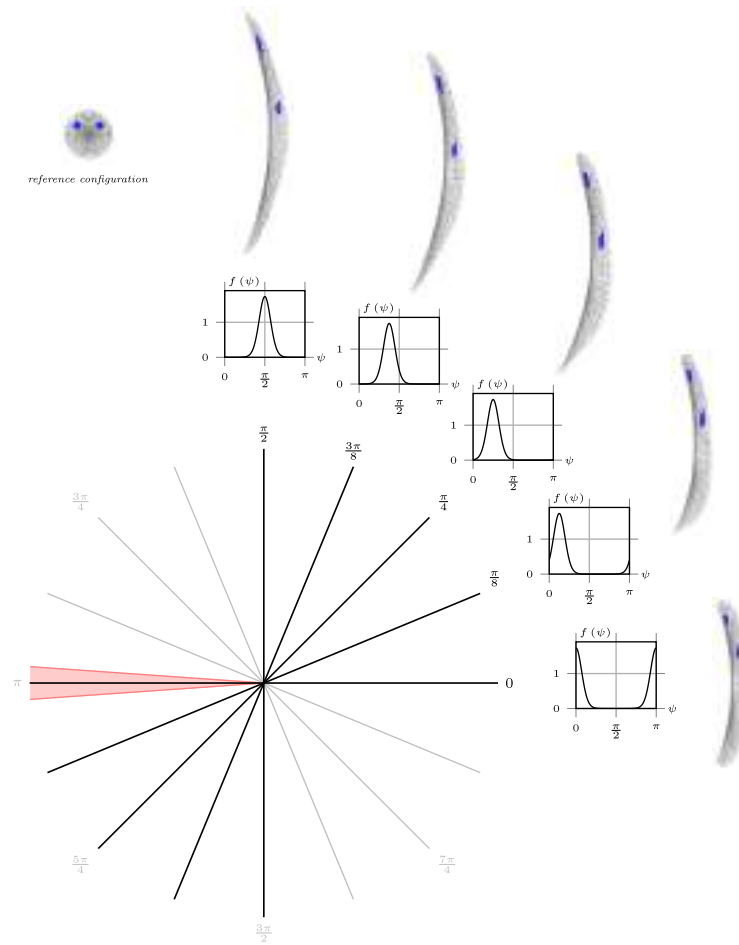
Fig. 5. Crack tip deformation for main fiber orientation (black solid line in the polar plot) $\psi_0 = 0, \frac{\pi}{8}, \frac{\pi}{4}, \frac{3\pi}{8}, \frac{\pi}{2}$, fiber dispersion $b = 5$, applied stretch $\lambda_S = 1.152$, ratio of fiber to matrix stiffness $\kappa = 10$. The position of the crack is highlighted in red in the polar plot. (For interpretation of the references to colour in this figure legend, the reader is referred to the web version of this article.)

$$
\begin{cases}
\sum_{i=1}^{n} sin(\psi + (i-1)\delta) cos(\psi + (i-1)\delta) = 0 \\
\sum_{i=1}^{n} sin^2(\psi + (i-1)\delta) = \sum_{i=1}^{n} cos^2(\psi + (i-1)\delta) \\
\sum_{i=1}^{n} \delta = \pi.
\end{cases}
\tag{42}
$$

Given that $\delta = \frac{\pi}{n}$, after some trigonometric manipulations, we have in matrix–vector form

$$
\sum_{i=1}^{n}
\begin{bmatrix}
\cos(2\psi) & -\sin(2\psi) \\
\sin(2\psi) & \cos(2\psi)
\end{bmatrix}
\begin{bmatrix}
\cos\left(2(i-1)\frac{\pi}{n}\right) \\
\sin\left(2(i-1)\frac{\pi}{n}\right)
\end{bmatrix}
= 0 \qquad \forall \psi.
\tag{43}
$$

Given that Eq. (43) must hold for any value of ψ, the problem is reduced to finding the values of n such that

$$
\sum_{i=1}^{n} \cos\left(2(i-1)\frac{\pi}{n}\right) = 0 \qquad \sum_{i=1}^{n} \sin\left(2(i-1)\frac{\pi}{n}\right) = 0,
\tag{44}
$$

where we recognize the arithmetic progressions of sines and cosines which are identically equal to zero [55,56]. Thus, conditions of *asymptotic isotropy* are satisfied by a discrete distribution of n fibers oriented at regular intervals of $\frac{\pi}{n}$ for any choice of $n > 1$, with $c_{44} = c_{55} = 1 + \kappa \frac{n}{2}$.

6.3.2. Continuous case

Consider a uniform distribution of fiber orientations $f_{uni}(\psi) = 1$ with $\psi \in [0, \pi]$, substituting into Eq. (39) we obtain $c_{44} = c_{55} = 1 + \frac{\kappa}{4}$ and

$c_{45} = 0$, thus satisfying the conditions of *asymptotic isotropy*.

6.3.3. Numerical results

The coefficients p_1, q_1, p_2 of the leading terms of the asymptotic expansion are evaluated using interaction integrals (denoted by Ξ^I) and the coordinate-based method (denoted by Ξ^C) for 6 different cases: ① isotropic Neo-Hookean sheet (for comparison); ② 2 families of fibers, $\psi_0 = 0, \frac{\pi}{4}, \kappa = 1$; ③ 2 families of fibers, $\psi_0 = -\frac{\pi}{4}, \frac{\pi}{4}, \kappa = 1$; ④ 3 families of fibers, $\psi_0 = -\frac{\pi}{3}, 0, \frac{\pi}{3}, \kappa = 1$; ⑤ 4 families of fibers, $\psi_0 = 0, \frac{\pi}{2}$ with $\kappa = 1$ and $\psi_0 = -\frac{\pi}{4}, \frac{\pi}{6}$ with $\kappa = 2$; ⑥ uniform distribution of fibers. Results are reported in Table 2. In agreement with the theoretical prediction, p_1 is equal to 0 for all 6 cases, as a material behaving isotropically for $r \rightarrow 0$ would result in a pure Mode I deformation at the crack tip under pure Mode I far-field boundary conditions. In the case of *asymptotic isotropy*, it is expected that $\sigma_{22} \sim \frac{1}{4} p_2^2 \sqrt{c_{44}} r^{-1}$, which is confirmed by the numerical results reported in Fig. 7.

It is worth pointing out here that the physical origin of the *asymptotic isotropy* lies in the choice of matrix and fiber material models and thus in the form of the strain energy density as discussed in Section 2. A different (non-linear) choice of strain energy density would not have lead to the identification of fiber orientation combinations that correspond to *asymptotic isotropy*.

Finally, notice that the condition of *asymptotic isotropy* is valid in the region of dominance of the asymptotic crack tip fields while far from the crack tip the material behaves anisotropically. To show this, we consider a thin sheet with a circular hole in plane stress subject to a uniform radial stretch $\lambda_R = 0.5$. For an isotropic material, the circular hole in the

(a)

(b)

(c)

(d)
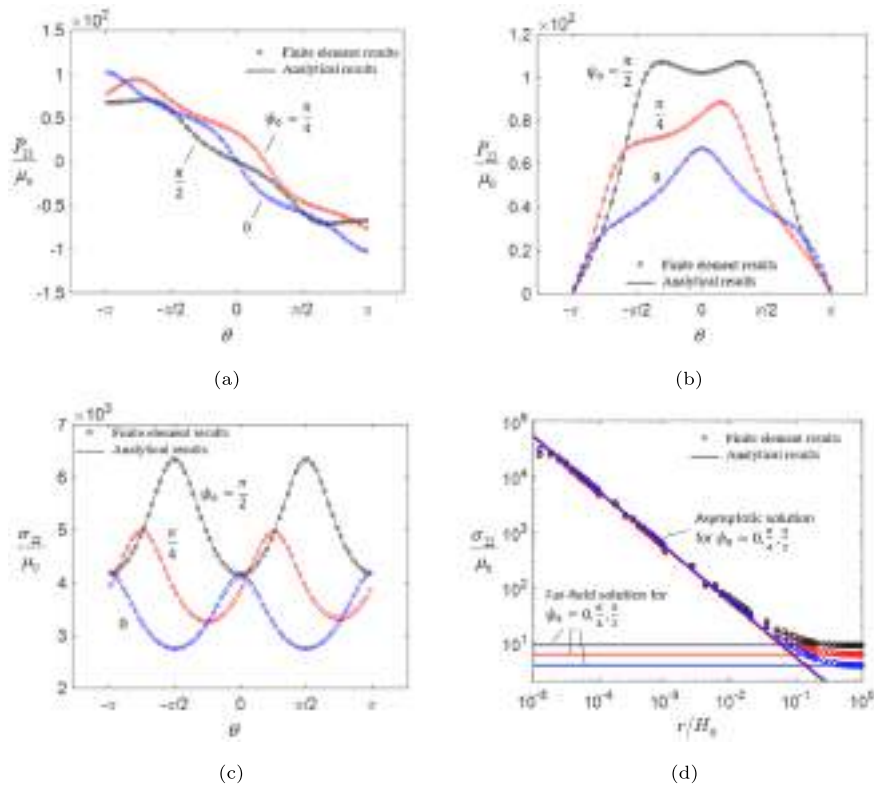
Fig. 6. Circumferential (17, 18 and 19) variation respectively of P_{21}, P_{22}, σ_{22} and radial (20) variation of σ_{22} for main fiber orientation $\psi_0 = 0, \frac{\pi}{4}, \frac{\pi}{2}$, fiber dispersion $b = 5$, applied stretch $\lambda_S = 2$, ratio of fiber to matrix stiffness $\kappa = 10$. Open circles correspond to FEM results, solid line to the analytical prediction based on the results of Eq. (27).

Table 2
Asymptotic expansion coefficients p_1, q_1, p_2 for different cases of *asymptotic isotropy* using interaction energy integrals, denoted by Ξ^I, and the coordinate based method, denoted by Ξ^C. Applied stretch $\lambda_S = 2$.

	① Isotropic (no fiber)			② 2 families of fibers $\psi_0 = 0, \frac{\pi}{2}$ $\kappa = 1 \; \forall \psi_0$			③ 2 families of fibers $\psi_0 = -\frac{\pi}{4}, \frac{\pi}{4}$ $\kappa = 1 \; \forall \psi_0$		
	p_1	p_2	q_1	p_1	p_2	q_1	p_1	p_2	q_1
Ξ^I	0.000	1.086	0.595	0.000	0.955	0.681	0.000	1.836	0.649
Ξ^C	0.000	1.091	0.598	0.000	0.988	0.692	0.000	1.824	0.652

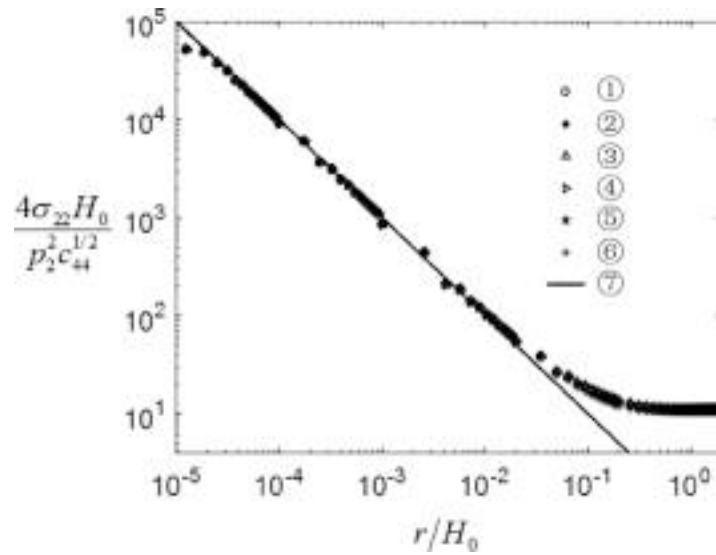|	④ 3 families of fibers $\psi_0 = -\frac{\pi}{3}, 0, \frac{\pi}{3}$ $\kappa = 1 \; \forall \psi_0$			⑤ 4 families of fibers $\psi_0 = 0, \frac{\pi}{2}, \kappa = 1$ $\psi_0 = -\frac{\pi}{4}, \frac{\pi}{4}, \kappa = 2$			⑥ Uniform distribution		
	p_1	p_2	q_1	p_1	p_2	q_1	p_1	p_2	q_1
Ξ^I	0.000	1.692	0.689	0.000	2.281	0.759	0.000	2.108	0.746
Ξ^C	0.000	1.673	0.693	0.000	2.275	0.763	0.000	2.106	0.750

deformed configuration is enlarged and remains circular (black solid line in Fig. 8). For an anisotropic material, the shape of the initially circular hole will changes (red solid line in Fig. 8, for the case of 2 families of fibers at $23°, 39°$). The deviation from circularity can thus be used as a proxy of the degree of anisotropy of the material. Observation of Fig. 8 shows that a matrix reinforced with 2 families of fibers at $0°, 90°$ or at $\pm45°$ is indeed anisotropic, and thus that the isotropic behavior shown in Fig. 7 occurs only in the region of dominance of the asymptotic fields.

### 6.4. Asymptotic universal one-to-one mapping

It is possible to interpret the transformation to canonical form introduced in Section 4.2 in a mechanical sense. Introducing the scaled deformation $\widetilde{y}_2$

$$\widetilde{y}_2 = \frac{y_2}{p_2\left((A_{11}\cos\theta + A_{12}\sin\theta)^2 + (A_{22}\sin\theta)^2\right)^{\frac{1}{4}}\sin\left(\frac{1}{2}\tan^{-1}\left(\frac{A_{22}\sin\theta}{A_{11}\cos\theta + A_{12}\sin\theta}\right)\right)}$$

(45)

and scaled Cauchy stress component $\widetilde{\sigma}_{22}$

Fig. 7. Asymptotic radial behavior of normalized $\frac{4\sigma_{22}H_0}{p_2^2 c_{44}^{1/2}}$. Angular position $\theta = \pi$, applied stretch $\lambda_S = 2$. ① isotropic Neo-Hookean sheet (for comparison); ② 2 families of fibers, $\psi_0 = 0, \frac{\pi}{2}, \kappa = 1$; ③ 2 families of fibers, $\psi_0 = -\frac{\pi}{4}, \frac{\pi}{4}, \kappa = 1$; ④ 3 families of fibers, $\psi_0 = -\frac{\pi}{3}, 0, \frac{\pi}{3}, \kappa = 1$; ⑤ 4 families of fibers, $\psi_0 = 0, \frac{\pi}{2}$ with $\kappa = 1$ and $\psi_0 = -\frac{\pi}{4}, \frac{\pi}{6}$ with $\kappa = 2$; ⑥ uniform distribution of fibers; ⑦ r^{-1}
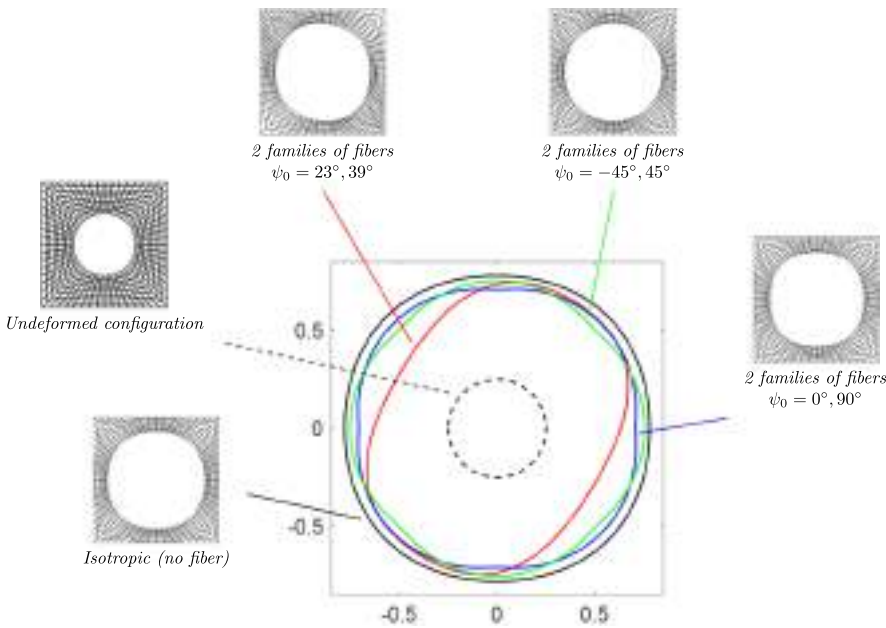
Fig. 8. Behavior of the unnotched material. Radial stretch $\lambda_R = 0.5$ applied to the outer boundary. In the main graph, the deformed configuration of the inner ring is compared between the different cases and with the undeformed configuration. *Black, dashed*: undeformed configuration; *black, solid*: isotropic Neo-Hookean sheet; *blue, solid*: 2 families of fibers, $\psi_0 = 0°, 90°$; *green, solid*: 2 families of fibers, $\psi_0 = -45°, 45°$; *red, solid*: 2 families of fibers, $\psi_0 = 23°, 39°$. $\kappa = 10$. (For interpretation of the references to colour in this figure legend, the reader is referred to the web version of this article.)

$$\widetilde{\sigma}_{22} = \frac{\sigma_{22}}{\frac{1}{4}\mu p_2^2 \left((A_{11}\cos\theta + A_{12}\sin\theta)^2 + (A_{22}\sin\theta)^2 \right)^{-\frac{1}{2}}}, \tag{46}$$

it is shown in Fig. 9 that the scaled variables present an asymptotic behavior identical to that of the isotropic sheet in plane stress, i.e. $\widetilde{y}_2 \sim r^{\frac{1}{2}}$ and $\widetilde{\sigma}_{22} \sim r^{-1}$ for every value of θ and any distribution of fiber orientation and elastic properties.

von Mises distribution, $\psi_0 = \frac{\pi}{4}, b = 5, \kappa = 10$ 2 families of fibers, $\psi_0 = 23°, 39°, \kappa = 1$; isotropic Neo-Hookean sheet; 2 families of fibers, $\psi_0 = 0, \frac{\pi}{2}, \kappa = 1$; uniform distribution of fibers, $\kappa = 1$.

Thus, the canonical transformation of Section 4.2 provides an *asymptotic universal one-to-one mapping* that maps the asymptotic mechanical response of an anisotropic Neo-Hookean fiber-reinforced composite to that of an isotropic Neo-Hookean thin sheet. The mapping depends on the geometry and boundary conditions of the specific

anisotropic problem and thus pairs one anisotropic with one isotropic configuration (*one-to-one*). As such, this mapping does not provide any significant advantage in computational cost, but it provides an interesting mechanical insight. Inspecting the structure of the linear transformation of Eq. (23), it is possible to argue that asymptotically the mechanical effect of the reinforcement in the anisotropic material is equivalent to a bi-axial stretch and in-plane shear applied to the isotropic Neo-Hookean thin sheet, i.e. to a geometric deformation of the isotropic material.

7. Conclusions

In this paper, we consider the large deformations at the crack tip of Neo-Hookean fiber reinforced composite sheet, where the orientation and elastic properties of the reinforcement are described by discrete and continuous spatial distributions. We adopt the material behavior
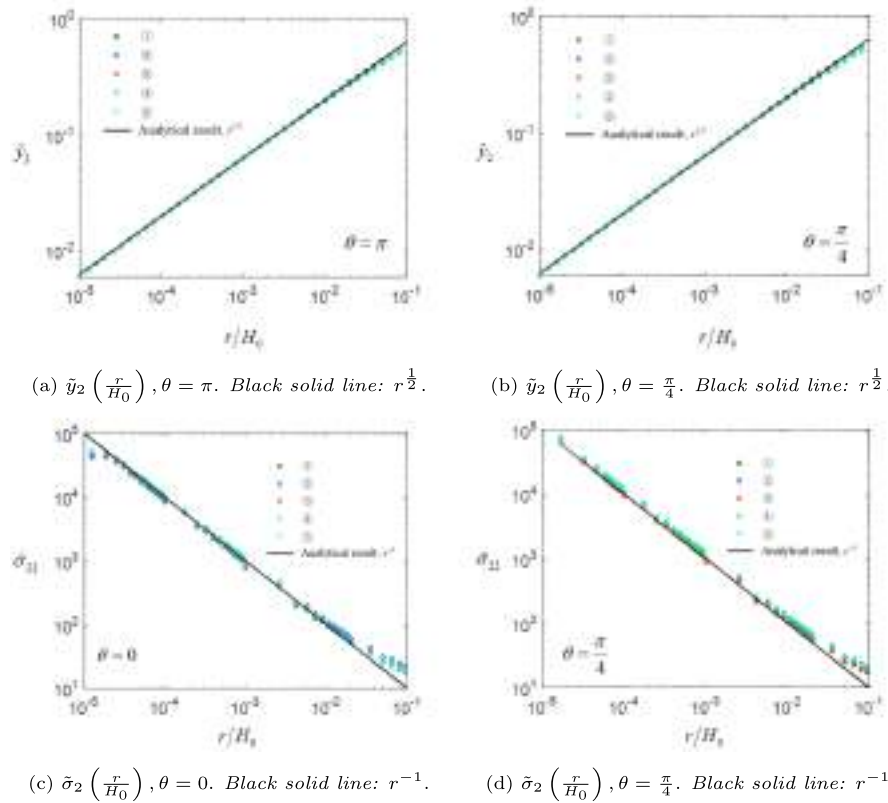
(a) $\tilde{y}_2\left(\frac{r}{H_0}\right), \theta = \pi$. *Black solid line:* $r^{\frac{1}{2}}$.

(b) $\tilde{y}_2\left(\frac{r}{H_0}\right), \theta = \frac{\pi}{4}$. *Black solid line:* $r^{\frac{1}{2}}$.

(c) $\tilde{\sigma}_2\left(\frac{r}{H_0}\right), \theta = 0$. *Black solid line:* r^{-1}.

(d) $\tilde{\sigma}_2\left(\frac{r}{H_0}\right), \theta = \frac{\pi}{4}$. *Black solid line:* r^{-1}.

Fig. 9. Radial behavior of scaled deformation $\tilde{y}_2$ (Eq. (45)) and scaled Cauchy stress component $\tilde{\sigma}_{22}$ (Eq. (46)).

introduced in [1–3] and use the crack tip integrals developed in [4,5] to evaluate the coefficients of the asymptotic expansion of the elastic fields at the crack tip. It is observed that the canonical transformation of the asymptotic boundary value problem maps the general anisotropic case to the isotropic problem [42].

Several cases of discrete and continuous distributions of fibers are considered and good agreement is always found between the numerical results and the analytical predictions. Given its use in the experimental literature, the *von Mises* distribution is analyzed in detail and conditions for a pure Mode I crack are found and discussed. It is then observed that specific distributions of orientations correspond to an isotropic material response in the region of dominance of the asymptotic fields, which we call conditions of *asymptotic isotropy*. Mathematically, it corresponds to the fact that the asymptotic boundary value problem becomes identical to the isotropic case [42] *without* resorting to the canonical transformation. A set of discrete and continuous distributions are found to obey the conditions of *asymptotic isotropy*. Numerical analysis of the asymptotic elastic fields confirms the theoretical predictions. Finally, it is shown that the canonical transformation of the asymptotic boundary value problem can be interpreted as an *asymptotic universal one-to-one mapping* between anisotropic and isotropic Neo-Hookean thin sheets under conditions of plane stress.

CRediT authorship contribution statement

Luca Di Stasioa: Conceptualization, Data curation, Formal analysis, Methodology, Visualization, Writing - original draft, Writing - review & editing. **Yin Liua:** Conceptualization, Data curation, Formal analysis, Methodology, Software, Validation, Visualization, Writing - review & editing. **Brian Morana:** Conceptualization, Data curation, Formal analysis, Methodology, Funding acquisition, Project administration, Resources, Supervision, Writing - review & editing.

Declaration of Competing Interest

The authors declare that they have no known competing financial interests or personal relationships that could have appeared to influence the work reported in this paper.

References

[1] Z. Guo, X. Peng, B. Moran, A composites-based hyperelastic constitutive model for soft tissue with application to the human annulus fibrosus, J. Mech. Phys. Solids 54 (9) (2006) 1952–1971, https://doi.org/10.1016/j.jmps.2006.02.006.

[2] Z. Guo, X. Peng, B. Moran, Mechanical response of neo-hookean fiber reinforced incompressible nonlinearly elastic solids, Int. J. Solids Struct. 44 (6) (2007) 1949–1969, https://doi.org/10.1016/j.ijsolstr.2006.08.018.

[3] Z. Guo, X. Peng, B. Moran, Large deformation response of a hyperelastic fibre reinforced composite: Theoretical model and numerical validation, Compos. A Appl. Sci. Manuf. 38 (8) (2007) 1842–1851, https://doi.org/10.1016/j.compositesa.2007.04.004.

[4] Y. Liu, B. Moran, Asymptotic path-independent integrals for the evaluation of crack-tip parameters in a neo-hookean material, Int. J. Fract. 224 (2020) 133–150, https://doi.org/10.1007/s10704-020-00452-4.

[5] Y. Liu, B. Moran, Large deformation near a crack tip in a fiber-reinforced neo-hookean sheet, J. Mech. Phys. Solids 143 (2020) 104049, https://doi.org/10.1016/j.jmps.2020.104049.

[6] S. Federico, W. Herzog, Towards an analytical model of soft biological tissues, J. Biomech. 41 (16) (2008) 3309–3313, https://doi.org/10.1016/j.jbiomech.2008.05.039.

[7] K.M. Meek, T. Blamires, G.F. Elliott, T.J. Gyi, C. Nave, The organisation of collagen fibrils in the human corneal stroma: A synchrotron x-ray diffraction study, Curr. Eye Res. 6 (7) (1987) 841–846, https://doi.org/10.3109/02713688709034853.

[8] P.B. Canham, H.M. Finlay, J.A. Kiernan, G.G. Ferguson, Layered structure of saccular aneurysms assessed by collagen birefringence, Neurol. Res. 21 (7) (1999) 618–626, https://doi.org/10.1080/01616412.1999.11740986.

[9] H.M. Finlay, L. McCullough, P.B. Canham, Three-dimensional collagen organization of human brain arteries at different transmural pressures, J. Vasc. Res. 32 (5) (1995) 301–312, https://doi.org/10.1159/000159104.

[10] J.-L. Gennisson, T. Deffieux, E. Macé, G. Montaldo, M. Fink, M. Tanter, Viscoelastic and anisotropic mechanical properties of in vivo muscle tissue assessed by supersonic shear imaging, Ultrasound Med. Biol. 36 (5) (2010) 789–801, https://doi.org/10.1016/j.ultrasmedbio.2010.02.013.

[11] S. Sherifova, G.A. Holzapfel, Biomechanics of aortic wall failure with a focus on dissection and aneurysm: A review, Acta Biomater. 99 (2019) 1–17, https://doi.org/10.1016/j.actbio.2019.08.017. doi: 10.1016/j.actbio.2019.08.017.

[12] A.D. Freed, D.R. Einstein, I. Vesely, Invariant formulation for dispersed transverse isotropy in aortic heart valves, Biomech. Model. Mechanobiol. 4 (2–3) (2005) 100–117, https://doi.org/10.1007/s10237-005-0069-8.

[13] T. Nakajima, T. Kurokawa, S. Ahmed, W. Li Wu, J.P. Gong, Characterization of internal fracture process of double network hydrogels under uniaxial elongation, Soft Matter 9 (6) (2013) 1955–1966, https://doi.org/10.1039/c2sm27232f.

[14] J.A. Stella, A. D'Amore, W.R. Wagner, M.S. Sacks, On the biomechanical function of scaffolds for engineering load-bearing soft tissues, Acta Biomater. 6 (7) (2010) 2365–2381, https://doi.org/10.1016/j.actbio.2010.01.001.

[15] A.S. Gladman, E.A. Matsumoto, R.G. Nuzzo, L. Mahadevan, J.A. Lewis, Biomimetic 4d printing, Nat. Mater. 15 (4) (2016) 413–418, https://doi.org/10.1038/nmat4544.

[16] T.C. Gasser, R.W. Ogden, G.A. Holzapfel, Hyperelastic modelling of arterial layers with distributed collagen fibre orientations, J. R. Soc. Interface 3 (6) (2005) 15–35, https://doi.org/10.1098/rsif.2005.0073.

[17] P. J. Flory, Thermodynamic relations for high elastic materials, Transactions of the Faraday Society 57 829. doi:10.1039/tf9615700829.

[18] R. Ogden, Nearly isochoric elastic deformations: Application to rubberlike solids, J. Mech. Phys. Solids 26 (1) (1978) 37–57, https://doi.org/10.1016/0022-5096(78)90012-1.

[19] J. Simo, R. Taylor, K. Pister, Variational and projection methods for the volume constraint in finite deformation elasto-plasticity, Comput. Methods Appl. Mech. Eng. 51 (1–3) (1985) 177–208, https://doi.org/10.1016/0045-7825(85)90033-7.

[20] C. Sansour, On the physical assumptions underlying the volumetric-isochoric split and the case of anisotropy, Eur. J. Mech. A. Solids 27 (1) (2008) 28–39, https://doi.org/10.1016/j.euromechsol.2007.04.001.

[21] S. Federico, T.C. Gasser, Nonlinear elasticity of biological tissues with statistical fibre orientation, J. R. Soc. Interface 7 (47) (2010) 955–966, https://doi.org/10.1098/rsif.2009.0502.

[22] Y. Lanir, Constitutive equations for fibrous connective tissues, J. Biomech. 16 (1) (1983) 1–12, https://doi.org/10.1016/0021-9290(83)90041-6.

[23] G.A. Holzapfel, R.W. Ogden, Constitutive modelling of arteries, Proc. Roy. Soc. A: Mathe., Phys. Eng. Sci. 466 (2118) (2010) 1551–1597, https://doi.org/10.1098/rspa.2010.0058.

[24] G. Chagnon, M. Rebouah, D. Favier, Hyperelastic energy densities for soft biological tissues, a review, J. Elast. 120 (2) (2014) 129–160, https://doi.org/10.1007/s10659-014-9508-z.

[25] G.A. Holzapfel, R.W. Ogden, S. Sherifova, On fibre dispersion modelling of soft biological tissues: a review, Proc. Roy. Soc. A: Mathe., Phys. Eng. Sci. 475 (2224) (2019) 20180736, https://doi.org/10.1098/rspa.2018.0736.

[26] K. Volokh, Modeling failure of soft anisotropic materials with application to arteries, J. Mech. Behav. Biomed. Mater. 4 (8) (2011) 1582–1594, https://doi.org/10.1016/j.jmbbm.2011.01.002.

[27] K. Volokh, Prediction of arterial failure based on a microstructural bi-layer fiber–matrix model with softening, J. Biomech. 41 (2) (2008) 447–453, https://doi.org/10.1016/j.jbiomech.2007.08.001.

[28] T.C. Gasser, An irreversible constitutive model for fibrous soft biological tissue: A 3-d microfiber approach with demonstrative application to abdominal aortic aneurysms, Acta Biomater. 7 (6) (2011) 2457–2466, https://doi.org/10.1016/j.actbio.2011.02.015.

[29] D. Li, A.M. Robertson, G. Lin, M. Lovell, Finite element modeling of cerebral angioplasty using a structural multi-mechanism anisotropic damage model, Int. J. Numer. Meth. Eng. 92 (5) (2012) 457–474, https://doi.org/10.1002/nme.4342.

[30] A. Ferrara, A. Pandolfi, Numerical modelling of fracture in human arteries, Comput. Methods Biomech. Biomed. Eng. 11 (5) (2008) 553–567, https://doi.org/10.1080/10255840701771743.

[31] E. Peña, J.A. Peña, M. Doblaré, On the mullins effect and hysteresis of fibered biological materials: A comparison between continuous and discontinuous damage models, Int. J. Solids Struct. 46 (7–8) (2009) 1727–1735, https://doi.org/10.1016/j.ijsolstr.2008.12.015.

[32] D. Balzani, S. Brinkhues, G.A. Holzapfel, Constitutive framework for the modeling of damage in collagenous soft tissues with application to arterial walls, Comput. Methods Appl. Mech. Eng. 213–216 (2012) 139–151, https://doi.org/10.1016/j.cma.2011.11.015.

[33] E. Maher, A. Creane, C. Lally, D.J. Kelly, An anisotropic inelastic constitutive model to describe stress softening and permanent deformation in arterial tissue,
J. Mech. Behav. Biomed. Mater. 12 (2012) 9–19, https://doi.org/10.1016/j.jmbbm.2012.03.001.

[34] T. Schmidt, D. Balzani, G.A. Holzapfel, Statistical approach for a continuum description of damage evolution in soft collagenous tissues, Comput. Methods Appl. Mech. Eng. 278 (2014) 41–61, https://doi.org/10.1016/j.cma.2014.04.011.

[35] R.J. Nims, K.M. Durney, A.D. Cigan, A. Dusséaux, C.T. Hung, G.A. Ateshian, Continuum theory of fibrous tissue damage mechanics using bond kinetics: application to cartilage tissue engineering, Interface Focus 6 (1) (2016) 20150063, https://doi.org/10.1098/rsfs.2015.0063.

[36] O. Gültekin, S.P. Hager, H. Dal, G.A. Holzapfel, Computational modeling of progressive damage and rupture in fibrous biological tissues: application to aortic dissection, Biomech. Model. Mechanobiol. 18 (6) (2019) 1607–1628, https://doi.org/10.1007/s10237-019-01164-y.

[37] W. Li, Damage models for soft tissues: A survey, J. Med. Biol. Eng. 36 (3) (2016) 285–307, https://doi.org/10.1007/s40846-016-0132-1.

[38] A.J.M. Spencer (Ed.), Continuum Theory of the Mechanics of Fibre-Reinforced Composites, Springer Vienna, 1984. doi:10.1007/978-3-7091-4336-0.

[39] J.A. Rogers, T. Someya, Y. Huang, Materials and mechanics for stretchable electronics, Science 327 (5973) (2010) 1603–1607, https://doi.org/10.1126/science.1182383.

[40] S. Lin, H. Yuk, T. Zhang, G.A. Parada, H. Koo, C. Yu, X. Zhao, Stretchable hydrogel electronics and devices, Adv. Mater. 28 (22) (2015) 4497–4505, https://doi.org/10.1002/adma.201504152.

[41] C. Yang, Z. Suo, Hydrogel ionotronics, Nat. Rev. Mater. 3 (6) (2018) 125–142, https://doi.org/10.1038/s41578-018-0018-7.

[42] J.K. Knowles, E. Sternberg, Large deformations near a tip of an interface-crack between two neo-hookean sheets, J. Elast. 13 (3) (1983) 257–293, https://doi.org/10.1007/bf00042997.

[43] F.S. Wong, R.T. Shield, Large plane deformations of thin elastic sheets of neo-hookean material, Zeitschrift für angewandte Mathematik und Physik ZAMP 20 (2) (1969) 176–199, https://doi.org/10.1007/BF01595559.

[44] G. Sih, P. Paris, G. Irwin, On cracks in rectilinearly anisotropic bodies, Int. J. Fracture Mech. 1 (3) (1965), https://doi.org/10.1007/bf00186854.

[45] J. Chang, J. Li, Evaluation of asymptotic stress field around a crack tip for neo–hookean hyperelastic materials, Int. J. Eng. Sci. 42 (15–16) (2004) 1675–1692, https://doi.org/10.1016/j.ijengsci.2004.03.009.

[46] C. Frank, B. MacFarlane, P. Edwards, R. Rangayyan, Z.-Q. Liu, S. Walsh, R. Bray, A quantitative analysis of matrix alignment in ligament scars: A comparison of movement versus immobilization in an immature rabbit model, J. Orthop. Res. 9 (2) (1991) 219–227, https://doi.org/10.1002/jor.1100090210.

[47] C. Frank, D. McDonald, D. Bray, R. Bray, R. Rangayyan, D. Chimich, N. Shrive, Collagen fibril diameters in the healing adult rabbit medial collateral ligament, Connect. Tissue Res. 27 (4) (1992) 251–263, https://doi.org/10.3109/03008209209007000.

[48] C. Hurschler, B. Loitz-Ramage, R. Vanderby, A structurally based stress-stretch relationship for tendon and ligament, J. Biomech. Eng. 119 (4) (1997) 392–399, https://doi.org/10.1115/1.2798284.

[49] M.S. Sacks, D.B. Smith, E.D. Hiester, The aortic valve microstructure: Effects of transvalvular pressure, J. Biomed. Mater. Res. 41 (1) (1998) 131–141, https://doi.org/10.1002/(sici)1097-4636(199807)41:1<131::aid-jbm16>3.0.co;2-q.

[50] M.S. Sacks, Incorporation of experimentally-derived fiber orientation into a structural constitutive model for planar collagenous tissues, J. Biomech. Eng. 125 (2) (2003) 280–287, https://doi.org/10.1115/1.1544508.

[51] M. Landuyt, G. A. Holzapfel, P. Verdonck, Structural quantification of collagen fibers in abdominal aortic aneurysms , Master's thesis, Department of Solid Mechanics, Royal Institute of Technology in Stockholm and Department of Civil Engineering, Ghent University, Master Thesis in electromechanical engineering, option biomedical engineering. 2006. URL https://lib.ugent.be/catalog/rug01:001311703.

[52] R.D. Rosenkrantz (Ed.), E.T. Jaynes: Papers on Probability, Statistics and Statistical Physics, Springer Netherlands, 1983. doi:10.1007/978-94-009-6581-2.

[53] N.I. Fisher, Statistical Analysis of Circular Data, Cambridge University Press, 1993. doi:10.1017/cbo9780511564345.

[54] K.L. Billiar, M.S. Sacks, Biaxial mechanical properties of the native and glutaraldehyde-treated aortic valve cusp: Part II—a structural constitutive model, J. Biomech. Eng. 122 (4) (2000) 327–335, https://doi.org/10.1115/1.1287158.

[55] J.A. Holdener, Math bite: Sums of sines and cosines, 126–126, Math. Mag. 82 (2) (2009), https://doi.org/10.1080/0025570x.2009.11953606.

[56] M.P. Knapp, Sines and cosines of angles in arithmetic progression, Math. Mag. 82 (5) (2009) 371–372, https://doi.org/10.4169/002557009x478436.

Finite Element solution of the fiber/matrix interface crack problem: Convergence properties and mode mixity of the Virtual Crack Closure Technique

Luca Di Stasio [a,b,*], Zoubir Ayadi [b]

[a] *Luleå University of Technology, University Campus, SE-97187, Luleå, Sweden*
[b] *Université de Lorraine, EEIGM, IJL, 6 Rue Bastien Lepage, F-54010, Nancy, France*

ARTICLE INFO

ABSTRACT

The bi-material interface arc crack has been the focus of interest in the composite community, where it is usually referred to as the fiber-matrix interface crack. In this work, we investigate the convergence properties of the Virtual Crack Closure Technique (VCCT) when applied to the evaluation of the Mode I, Mode II and total Energy Release Rate of the fiber-matrix interface crack in the context of the Finite Element Method (FEM). We first propose a synthetic vectorial formulation of the VCCT. Thanks to this formulation, we study the convergence properties of the method, both analytically and numerically. It is found that Mode I and Mode II Energy Release Rate (ERR) possess a logarithmic dependency with respect to the size of the elements in the crack tip neighborhood, while the total ERR is independent of element size.

1. Introduction

Bi-material interfaces represent the basic load transfer mechanism at the heart of Fiber Reinforced Polymer Composite (FRPC) materials. They are present at the macroscale, in the form of adhesive joints; at the mesoscale, as interfaces between layers with different orientations; at the microscale, as fiber-matrix interfaces. Bi-material interfaces have for long attracted the attention of researchers in Fracture Mechanics [1,2], due to their hidden complexity.

The problem was first addressed in the 1950's by Williams [3], who derived through a linear elastic asymptotic analysis the stress distribution around an *open* crack (i.e. with crack faces nowhere in contact for any size of the crack) between two infinite half-planes of dissimilar materials. He found the existence of a strong oscillatory behavior in the stress singularity at the crack tip of the form

$$r^{-\frac{1}{2}} \sin\left(\varepsilon \log r\right) \quad \text{with} \quad \varepsilon = \frac{1}{2\pi} \log\left(\frac{1-\beta}{1+\beta}\right), \tag{1}$$

in both Mode I and Mode II. In Eq. (1), β is one of the two parameters introduced by Dundurs [4] to characterize bi-material interfaces:

$$\beta = \frac{\mu_2 \left(\kappa_1 - 1\right) - \mu_1 \left(\kappa_2 - 1\right)}{\mu_2 \left(\kappa_1 + 1\right) + \mu_1 \left(\kappa_2 + 1\right)} \tag{2}$$

where $\kappa = 3 - 4\nu$ in plane strain and $\kappa = \frac{3-4\nu}{1+\nu}$ in plane stress, μ is the shear modulus, ν Poisson's coefficient, and indexes $1, 2$ refer to the two bulk materials joined at the interface. Defining a as the length of the crack, it was found that the size of the oscillatory region is in the order of $10^{-6}a$ [5]. Given the oscillatory behavior of the crack tip singularity of Eq. (1), the definition of Stress Intensity Factor (SIF) $\lim_{r\to 0} \sqrt{2\pi r}\sigma$ diverges and ceases to be valid [1]. It implies that the Mode mixity problem at the crack tip is ill-posed.

It was furthermore observed, always in the context of Linear Elastic Fracture Mechanics (LEFM), that an interpenetration zone exists close to the crack tip [6,7] with a length in the order of $10^{-4}a$ [6]. Following conclusions firstly proposed in Ref. [7], the presence of a *contact zone* in the crack tip neighborhood, of a length to be determined from the solution of the elastic problem, was introduced in Ref. [8] and shown to provide a physically consistent solution to the straight bi-material interface crack problem.

The curved bi-material interface crack, more often referred to as the fiber-matrix interface crack (or debond) due to its relevance in FRPCs, was first treated by England [9] and by Perlman and Sih [10], who provided the analytical solution of stress and displacement fields for a circular inclusion with respectively a single debond and an arbitrary number of debonds. Building on their work, Toya [11] particularized

* Corresponding author. Luleå University of Technology, University Campus, SE-97187, Luleå, Sweden.
E-mail address: luca.di.stasio@ltu.se (L. Di Stasio).

the solution and provided the expression of the Energy Release Rate (ERR) at the crack tip. The same problems exposed previously for the *open* straight bi-material crack were shown to exist also for the *open* fiber-matrix interface crack: the presence of strong oscillations in the crack tip singularity and onset of crack face interpenetration at a critical flaw size.[1]

In order to treat cases more complex than the single partially debonded fiber in an infinite matrix of [9–11], numerical studies followed. In the 1990's, París and collaborators [12] developed a Boundary Element Method (BEM) with the use of discontinuous singular elements at the crack tip and the Virtual Crack Closure Integral (VCCI) [13] for the evaluation of the Energy Release Rate (ERR). They validated their results [12] with respect to Toya's analytical solution [11] and analyzed the effect of BEM interface discretization on the stress field in the neighborhood of the crack tip [14]. Following Comninou's work on the straight crack [8], they furthermore recognized the importance of contact to retrieve a physical solution avoiding interpenetration [12] and studied the effect of the contact zone on debond ERR [15]. Their algorithm was then applied to investigate the fiber-matrix interface crack under different geometrical configurations and mechanical loadings [16–22].

Recently the Finite Element Method (FEM) was also applied to the solution of the fiber-matrix interface crack problem [23–25], in conjunction with the Virtual Crack Closure Technique (VCCT) [26,27] for the evaluation of the ERR at the crack tip. In Ref. [23], the authors validated their model with respect to the BEM results of [12], but no analysis of the effect of the discretization in the crack tip neighborhood comparable to Ref. [14] was proposed. Thanks to the interest in evaluating the ERR of interlaminar delamination, different studies exist in the literature on the effect of mesh discretization on Mode I and Mode II ERR of the straight bi-material interface crack when evaluated with the VCCT in the context of the FEM (see for example [28] for a review). An early result on the problem is available in Ref. [29]. Here the authors evaluated with the Virtual Crack Closure Technique Mode I and Mode II Energy Release Rate of both a central crack and an edge crack at the interface between two 2D plates of different isotropic materials subjected to tensile loading. They showed analytically that the total ERR G is well defined while Mode I and Mode II ERR, respectively G_I and G_{II}, do not converge. They confirmed their analytical derivations numerically by solving the two problems with the Finite Element Method and evaluating the ERR with the VCCT. Referring to the crack length as a and to the length of an element at the crack tip as Δa, they found that the total ERR was independent of normalized element size $\Delta a/a$ while G_I and G_{II} were dependent on assumed crack extension, i.e. element size at the crack tip. In particular, they showed a decreasing G_I and an increasing G_{II} with decreasing element size for both crack configurations. The same analysis was conducted, and analogous results obtained, in Ref. [30] for a central crack under either far-field tensile or shear loading between two orthotropic materials in 2D and in Ref. [31] for a central crack subjected to far-field tension between two orthotropic solids in 3D. The convergence of VCCT-based mode decomposition was analyzed in Ref. [32] for edge delaminations in laminated composites subjected to tensile loading coplanar and normal to crack propagation direction in a quasi-3D setting. Again, it was observed that the total ERR was independent of mesh size while Mode I and Mode II ERR showed dependency and no convergence could be established. In this configuration however, it was found that G_I increases and G_{II} decreases with decreasing element size. The application of the VCCT to the problem of composite skin-stiffener debonding was considered in Ref. [33] in conjunction with 2D plate elements, where the authors studied the effect of different combinations of adherends' layup, thick-

ness and fiber orientation at the interface on Mode decomposition. Only in the case of skin and stiffener with the same layup, same thickness and identical fiber orientation at the interface, Mode I and Mode II were found to be independent of mesh size. In all other cases, G_I and G_{II} were dependent on assumed crack extension and showed a trend similar to the one in Ref. [32]. The absence of a converging Mode-decomposed solution with the VCCT has motivated proposals for alternative solution. In Ref. [34], the authors analyze several proposals of mode-mixity parameters and suggest a correction to the VCCT-based mode-mixity ratio by assuming a reference characteristic length. The authors themselves however admit that this characteristic length has no physical interpretation. In Ref. [35], the problem of Mode-decomposition is solved through the development of analytical relations based on Euler and Timoshenko beam models. It is however well suited only for those configurations that can be split into beam elements, such as the Double Cantilever Beam (DCB) specimen.

No comparable analysis can be found in the literature on Mode separation and convergence analysis of the VCCT when applied to the fiber-matrix interface crack (circular bi-material interface crack) problem in the context of a linear elastic FEM solution. In the present article, we first present the FEM formulation of the problem, together with the main geometrical characteristics, material properties, boundary conditions and loading. We then propose a vectorial formulation of the VCCT and express Mode I and Mode II ERR in terms of FEM natural variables. Differently from the usual approach found in the literature, we do not express G_I and G_{II} as functions of stress and displacement fields using the results from complex analysis. We instead focus on the mathematical structure of the 1-step VCCT in the context of the Finite Element Method and write the crack tip forces as a linear combination of the crack faces displacements at the crack tip (plus a term representing the influence of the rest of the model). The ERR is consequently a quadratic function of the crack faces displacements. Given that, if the FEM solution is converging, stress and displacement fields are characterized by the oscillating singularity of Equation (1), it is possible to evaluate the behavior of the VCCT-calculated Energy Release Rate in the limit of crack tip element size going to zero. We are thus able to derive analytically a functional form of the dependency of the ERR on crack tip element size. Finally, the functional form thus derived is compared to the numerical results obtained with the Finite Element Method.

2. FEM formulation of the fiber-matrix interface crack problem

In order to investigate the fiber-matrix interface crack problem, a 2-dimensional model of a single fiber inserted in a rectangular matrix element is considered (see Fig. 1). Total element length and height are respectively $2L$ and L, where L is determined by the fiber radius R_f and the fiber volume fraction V_f by

$$L = \frac{R_f}{2}\sqrt{\frac{\pi}{V_f}}. \qquad (3)$$

The fiber radius R_f is assumed to be equal to 1 μm. This choice is not dictated by physical considerations but for simplicity. It is thus useful to remark that, in a linear elastic solution as the one considered in the present work, the ERR is proportional to the geometrical dimensions of the model and, consequently, recalculation of the ERR for fibers of any size requires a simple multiplication.

As shown in Fig. 1, the debond is placed symmetrically with respect to the x axis and its size is characterized by the angle $\Delta\theta$ (which makes the full debond size equal to $2\Delta\theta$ and the full crack length equal to $R_f 2\Delta\theta$). A region $\Delta\Phi$ of unknown size appears at the crack tip for large debond sizes (at least $\geq 60°$–$80°$), in which the crack faces are in contact with each other and free to slide. Frictionless contact is thus considered between the two crack faces to allow free sliding and avoid interpenetration. Symmetry with respect to the x axis is applied on the lower boundary while the upper surface is left free. Kinematic coupling on the x-displacement is applied along the left and right sides of the model

---

[1] For the fiber-matrix interface crack, flaw size is measured in terms of the angle $\Delta\theta$ subtended by half of the arc-crack, i.e. $a = 2\Delta\theta R_f$ where R_f is the inclusion (fiber) radius and $\Delta\theta$ is expressed in radians.
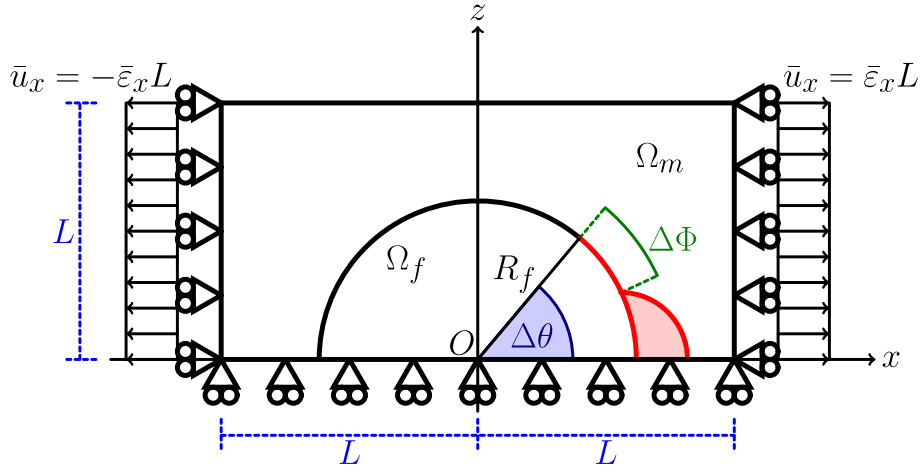
Fig. 1. Schematic of the model with its main parameters.

Table 1

Summary of the mechanical properties of fiber and matrix. E stands for Young's modulus, μ for shear modulus and ν for Poisson's ratio.

Material	$E\,[GPa]$	$\mu\,[GPa]$	$\nu\,[-]$
Glass fiber	70.0	29.2	0.2
Epoxy	3.5	1.25	0.4

in the form of a constant x-displacement $\pm\bar{\varepsilon}_x L$, which corresponds to transverse strain $\bar{\varepsilon}_x$ equal to 1% in the results here presented.

The model problem is solved with the Finite Element Method (FEM) within the Abaqus environment, a commercial FEM software [36]. The model is meshed with second order, 2D, plane strain triangular (CPE6) and rectangular (CPE8) elements. A regular mesh of rectangular elements with almost unitary aspect ratio is used at the crack tip. The angular size δ of an element in the crack tip neighborhood represents the main parameter of the numerical analysis. The crack faces are modeled as element-based surfaces and a small-sliding contact pair interaction with no friction is imposed between them. The Mode I, Mode II and total Energy Release Rates (ERRs) (respectively referred to as G_I, G_{II} and G_{TOT}) are evaluated using the VCCT [27], implemented in a in-house Python routine. A glass fiber-epoxy system is considered in the present work, and it is assumed that their response lies always in the linear elastic domain. The elastic properties of glass fiber and epoxy are reported in Table 1.

3. Vectorial formulation of the Virtual Crack Closure Technique (VCCT)

In order to express the VCCT formulation of the ERR in terms of FEM variables, we need to introduce a few rotation matrices in order to represent the discretized representation (FE mesh) of a crack along a circular interface. The position of the crack tip is characterized by the angular size of the crack (see Sec. 2 and Fig. 1 for reference) and the rotation corresponding to the crack tip reference frame is represented by the matrix $\underline{\underline{R}}_{\Delta\theta}$ defined as

$$\underline{\underline{R}}_{\Delta\theta} = \begin{bmatrix} \cos(\Delta\theta) & \sin(\Delta\theta) \\ -\sin(\Delta\theta) & \cos(\Delta\theta) \end{bmatrix}. \tag{4}$$

Nodes belonging to the elements sharing the crack tip are involved in the VCCT estimation of the ERR and it is assumed that, given a sufficiently fine discretization, they are aligned with the crack propagation
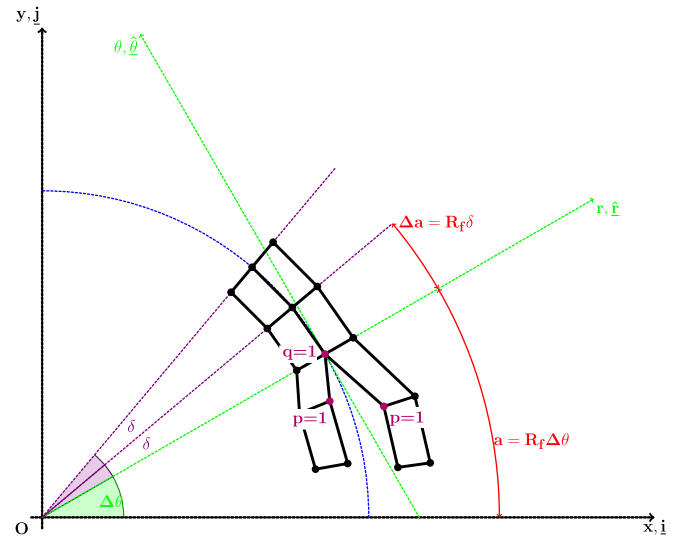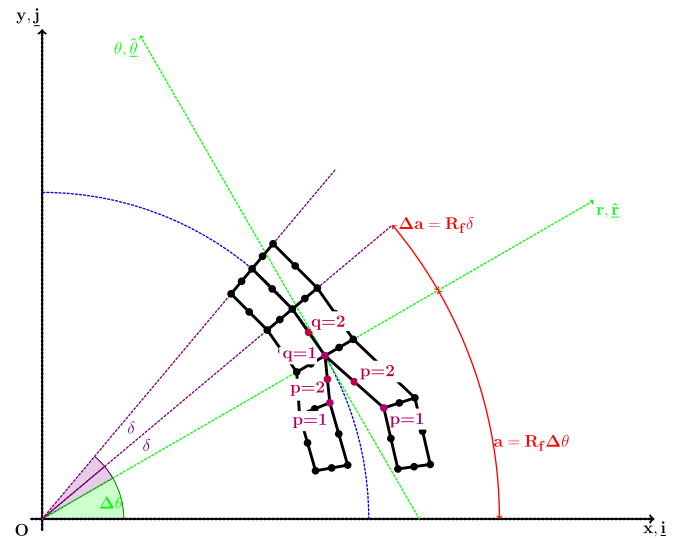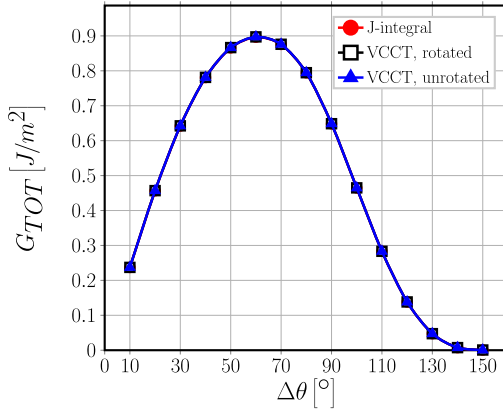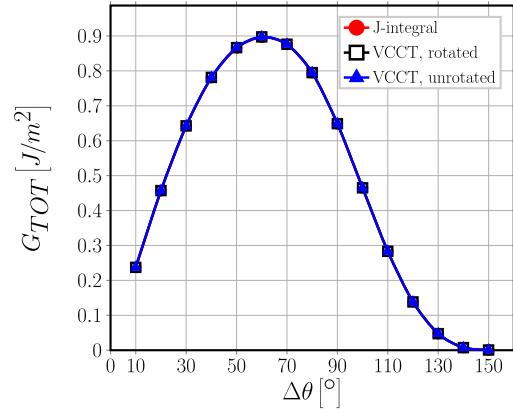

(a) Elements with 1st order shape functions: $m = 1$ and $p, q = 1$.

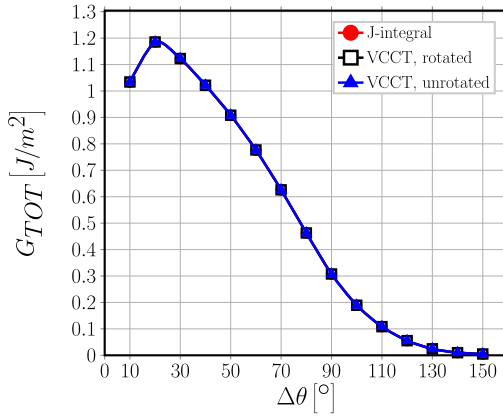(b) Elements with 2nd order shape functions: $m = 2$ and $p, q = 1, 2$.

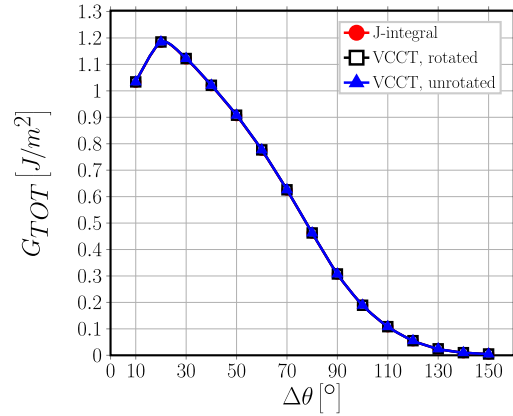**Fig. 2.** Schematic of the mesh at the fiber/matrix interface crack tip.

(a) $V_f = 0.1\%$, 1st order elements, $\delta = 0.05°$.

(b) $V_f = 0.1\%$, 2nd order elements, $\delta = 0.05°$.

(c) $V_f = 40\%$, 1st order elements, $\delta = 0.05°$.

(d) $V_f = 40\%$, 2nd order elements, $\delta = 0.05°$.

Fig. 3. Numerical invariance of the total Energy Release Rate: G_{TOT} computed with the VCCT with rotated forces and displacements (label *rotated*), with the VCCT with forces and displacements in the global reference frame (label *unrotated*) and with J-integral method (label *J-integral*).

direction defined at the crack tip.

However, irrespectively of how small the elements in the crack tip neighborhood are, a misalignment always exists with respect to the assumed crack propagation direction (in the crack tip reference frame). This is measured by the matrices $\underline{\underline{P}}_\delta (p)$, defined as

$$\underline{\underline{P}}_\delta (p) = \begin{bmatrix} \cos\left(\left(1 + \dfrac{1-p}{m}\right)\delta\right) & \sin\left(\left(1 + \dfrac{1-p}{m}\right)\delta\right) \\ -\sin\left(\left(1 + \dfrac{1-p}{m}\right)\delta\right) & \cos\left(\left(1 + \dfrac{1-p}{m}\right)\delta\right) \end{bmatrix} \tag{5}$$

and $\underline{\underline{Q}}_\delta (q)$, equal to

$$\underline{\underline{Q}}_\delta (q) = \begin{bmatrix} \cos\left(\dfrac{q-1}{m}\delta\right) & \sin\left(\dfrac{q-1}{m}\delta\right) \\ -\sin\left(\dfrac{q-1}{m}\delta\right) & \cos\left(\dfrac{q-1}{m}\delta\right) \end{bmatrix}, \tag{6}$$

respectively for the free and bonded nodes involved in the VCCT estimation. In Eqs. (5) and (6), δ is the angular size of an element in the crack tip neighborhood (see Sec. 2 and Fig. 1), m is the order of the element shape functions and $p, q = 1, \ldots, m$ are indices referring to the nodes belonging respectively to free and bonded elements sharing the crack tip. Fig. 2 shows the p, q-based numbering of nodes at the crack

tip in the case of elements with linear and quadratic (serendipity) shape functions. Introducing the permutation matrix

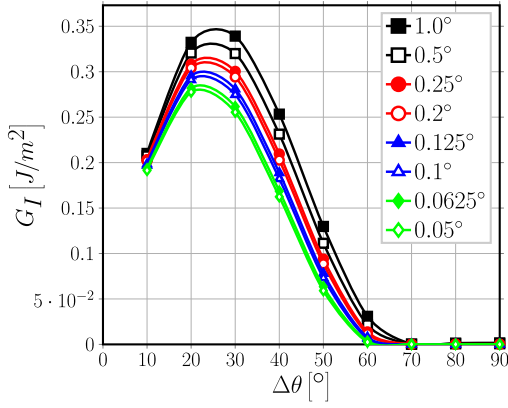$$\underline{\underline{P}}_\pi = \begin{bmatrix} 0 & 1 \\ -1 & 0 \end{bmatrix}, \tag{7}$$

it is possible to express the derivatives of rotation matrices $\underline{\underline{R}}_{\Delta\theta}, \underline{\underline{P}}_\delta$ and $\underline{\underline{Q}}_\delta$ with respect to their argument:

$$\frac{\partial \underline{\underline{R}}_{\Delta\theta}}{\partial \Delta\theta} = \underline{\underline{P}}_\pi \cdot \underline{\underline{R}}_{\Delta\theta}, \qquad \frac{\partial \underline{\underline{P}}_\delta}{\partial \delta} = \left(1 + \frac{1-p}{m}\right)\underline{\underline{P}}_\pi \cdot \underline{\underline{P}}_\delta,$$

$$\frac{\partial \underline{\underline{Q}}_\delta}{\partial \delta} = \frac{q-1}{m}\underline{\underline{P}}_\pi \cdot \underline{\underline{Q}}_\delta. \tag{8}$$

By means of Eqs. (5) and (6), we can express the crack tip forces $\underline{F}_{xy} = \begin{bmatrix} F_x \\ F_y \end{bmatrix}$ and crack displacements $\underline{u}_{xy} = \begin{bmatrix} u_x \\ u_y \end{bmatrix}$ in the crack tip reference frame (where the tangential direction θ correspond to the direction of crack propagation) while taking into account the misalignment to the finite discretization as

$$\underline{F}_{r\theta} = \underline{\underline{Q}}_\delta \underline{\underline{R}}_{\Delta\theta} \underline{F}_{xy} \qquad \underline{u}_{r\theta} = \underline{\underline{P}}_\delta \underline{\underline{R}}_{\Delta\theta} \underline{u}_{xy} \tag{9}$$

4

(a) $V_f = 0.1\%$, 1st order elements.
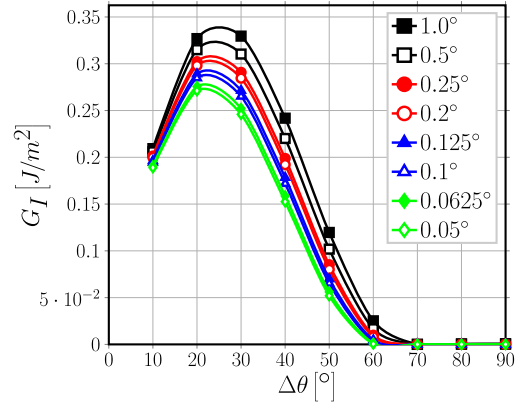
(b) $V_f = 0.1\%$, 2nd order elements.
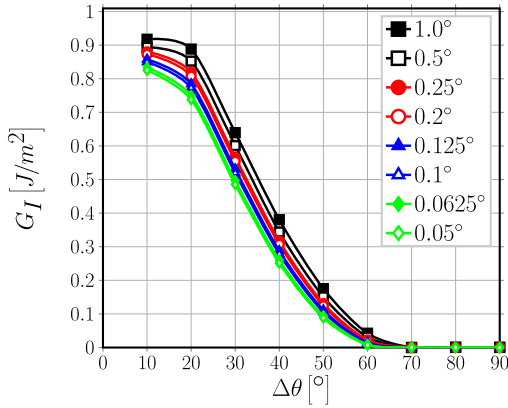
(c) $V_f = 40\%$, 1st order elements.
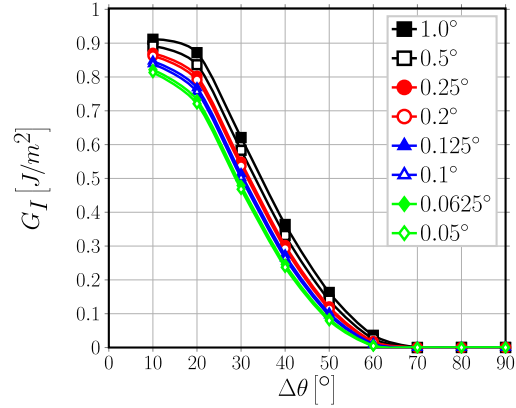
(d) $V_f = 40\%$, 2nd order elements.

Fig. 4. Effect of the size δ of an element at the crack tip on Mode I ERR.

where $\underline{F}_{r\theta} = \begin{bmatrix} F_r \\ F_\theta \end{bmatrix}$ and $\underline{u}_{r\theta} = \begin{bmatrix} u_r \\ u_\theta \end{bmatrix}$.

The crack tip forces can be expressed as a function of the crack opening displacement as

$$\underline{F}_{xy} = \underline{\underline{K}}_{xy}\,\underline{u}_{xy} + \widetilde{\underline{F}}_{xy}, \tag{10}$$

where $\underline{\underline{K}}_{xy}$ is in general a full matrix of the form $\underline{\underline{K}}_{xy} = \begin{bmatrix} K_{xx} K_{xy} \\ K_{yx} K_{yy} \end{bmatrix}$ and $\widetilde{\underline{F}}_{xy}$ represents the effect of the rest of the FE solution through the remaining nodes of the elements attached to the crack tip. As such, the term $\widetilde{\underline{F}}_{xy}$ can be expressed as a linear combination of the solution vector $\underline{u}_N$ of nodal displacements of the form $\widetilde{\underline{\underline{K}}}_N\,\underline{u}_N$. Equation (10) thus become

$$\underline{F}_{xy} = \underline{\underline{K}}_{xy}\,\underline{u}_{xy} + \widetilde{\underline{\underline{K}}}_N\,\underline{u}_N. \tag{11}$$

An exemplifying derivation of the relationships expressed in Equations (10) and (11) can be found in Appendix A. It is worthwhile to observe that another author [37,38] proposes a similar relationship, but in terms of flexibility $\underline{u} = \underline{\underline{C}}F$. In Refs. [37,38], Valvo expresses the forces at the crack tip as a (linear) function of the crack faces displacements at the same point. The technique analyzed in Refs. [37,38] is the 2-steps VCCT [27]: given a structure with a crack of length a, a first simulation is run to compute the forces at the crack tip and, in the case, at the internal nodes of the first bonded element for *p*-refined meshes; then, a second simulation is conducted with the crack extended by Δa, where in practice Δa is the length of the element at the crack

tip, and crack faces displacements are evaluated at the same nodes, now released, where previously forces were extracted. The Energy Release Rate is computed as the product of forces and displacements evaluated at the same nodes. The 2-steps VCCT adheres more strictly to the principle of the crack closure integral [13,39]: the work needed to open the crack by δa (Energy Release Rate) is equal in magnitude to the work required to close it by the same amount. Forces and displacements should be thus evaluated at the same point respectively in the closed and open crack configuration. In this paper, we consider on the other hand the 1-step VCCT [27]: if the size of the elements at the crack tip is sufficiently small, the error committed by approximating the crack faces displacements at the crack tip with those one element before is negligible. This in turn eliminates the need for a second simulation and thus cut the required computational time by a half. Following the principle of the crack closure integral [13,39], Valvo's proposal is based on the observation that the crack face displacements at the crack tip for a virtual crack extension will be equal in magnitude and opposite in sign due the displacements caused by the application of crack tip forces. Thus, namely: $u_{open\ crack} = -u_{closed\ crack} = f(F_{closed\ crack})$, and for linear elastic materials $f(F_{closed\ crack})$ would be linear, hence the introduction of a flexibility matrix [38]. Given that we instead work with the 1-step VCCT, we start from the observation that, in a Finite Element solution, the forces at a point can be expressed as a linear combination of all the displacements of the model through the global stiffness matrix. We have followed a stiffness approach and we have proceeded to isolate the contribution of crack faces displacements on crack tip forces. This leaves an additional term $\widetilde{\underline{\underline{K}}}_N\,\underline{u}_N$ in Equation (11), which represents the contribution of the rest of the model and that is not present in Valvo's

(a) $V_f = 0.1\%$, 1st order elements.

(b) $V_f = 0.1\%$, 2nd order elements.

(c) $V_f = 40\%$, 1st order elements.

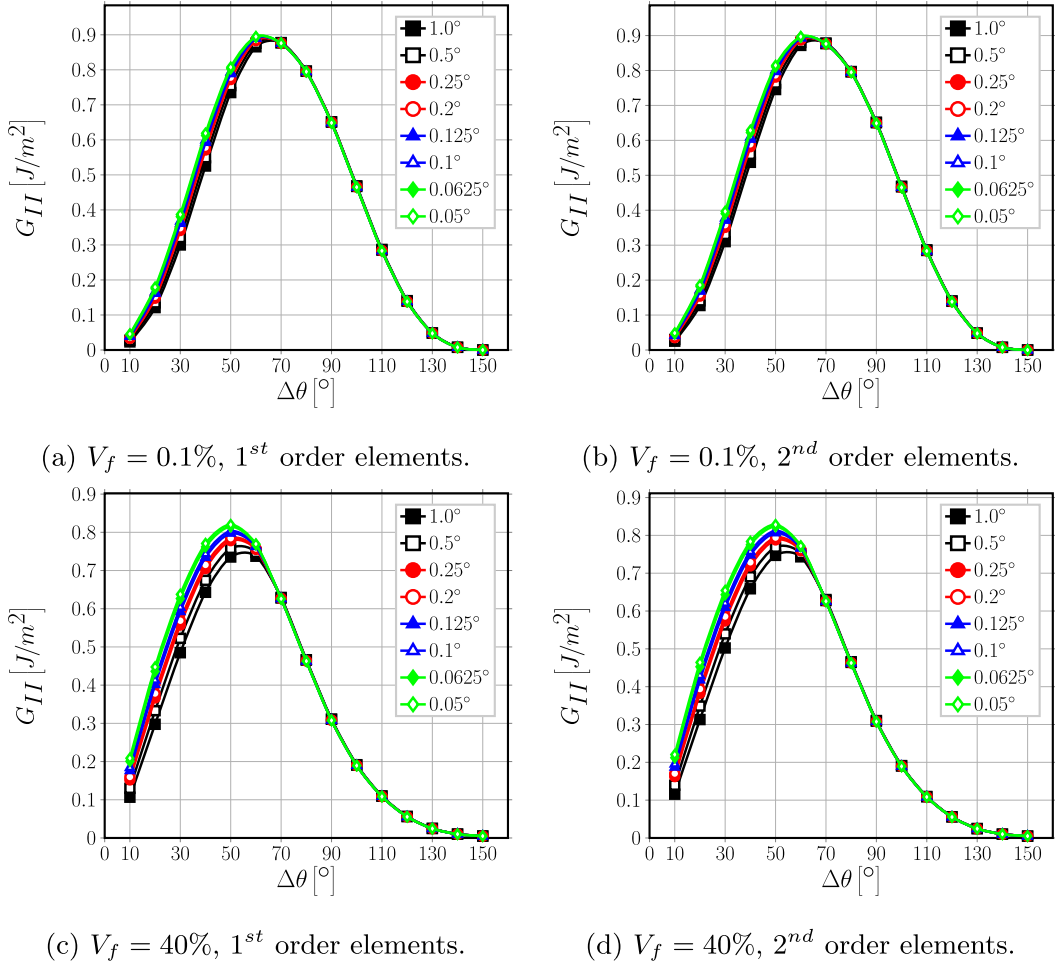(d) $V_f = 40\%$, 2nd order elements.

Fig. 5. Effect of the size δ of an element at the crack tip on Mode II ERR.

proposal. Notice that the linearity of Equation (11) does not stem from material linearity, but from the structure of the FEM solution. It can thus, in principle, be applied to non-linear materials, although as part of a secant- or tangent-based linearization. Notice that both the stiffness matrix of Equation (11) and Valvo's flexibility matrix possess out-of-diagonal elements, which represent the contribution of Poisson's effect.

Based upon the work of Raju [40], we introduce the matrix $\underset{=pq}{T}$ to represent the weights needed in the VCCT to account for the use of singular elements. As already done previously, indices p and q refer to nodes placed respectively on the free (crack face) and bonded side of the crack tip. Nodes are enumerated so that the crack tip has always index 1, i.e. the higher the index the further the node is from the crack tip. Matrix $\underset{=pq}{T}$ has always a size of $d \times d$, where $d = 2$ for a 2D problem and $d = 3$ for a 3D problem. An element $\underset{=pq}{T}(i,j)$ with $i,j = 1, \ldots, d$ represents the weight to be assigned to the product of component i of the displacement extracted at node p with component j of the force extracted at node q. The expression of $\underset{=pq}{T}$ for quadrilateral elements with or without singularity is reported in Appendix B. Notice that, given m is the order of the element shape functions, the element side has $m + 1$ nodes and this represents the upper limit of indices p and q.

By using matrix $\underset{=pq}{T}$, it is possible to express the total ERR G evaluated with the VCCT as

$$G_{TOT} = \frac{1}{2R_f\delta} \sum_{p=1}^{m+1} \sum_{q=1}^{m+1} Tr\left(\underline{F}_{r\theta,q} \underline{u}_{r\theta,p}^T \underset{=pq}{T} \right), \tag{12}$$

where the symbol Tr stands for the *Trace* operator, which sums together the elements on the matrix main diagonal (first matrix invariant). Introducing the vector $\underline{G} = \begin{bmatrix} G_I \\ G_{II} \end{bmatrix}$ of fracture mode ERRs, Mode I and Mode II ERR evaluated with the VCCT can be expressed as

$$\underline{G} = \frac{1}{2R_f\delta} \sum_{p=1}^{m+1} \sum_{q=1}^{m+1} Diag\left(\underline{F}_{r\theta,q} \underline{u}_{r\theta,p}^T \underset{=pq}{T} \right), \tag{13}$$

where $Diag()$ is the function that extracts the main diagonal of the input matrix as a column vector. Substituting Equations (9) and (11) in Equations (12) and (13), we can express the Mode I, Mode II and total Energy Release Rate as a function of the crack displacements and the FE solution (more details in Appendix A) as

$$G_{TOT} = \frac{1}{2R_f\delta} \sum_{p=1}^{m+1} \sum_{q=1}^{m+1} Tr\left(\underset{=\delta}{Q} \underset{=\Delta\theta}{R} \underset{=xy,q}{K} \underline{u}_{xy,q} \underline{u}_{xy,p}^T \underset{=\Delta\theta}{R}^T \underset{=\delta}{P}^T \underset{=pq}{T}^T \right)$$

$$+ \frac{1}{2R_f\delta} \sum_{p=1}^{m+1} \sum_{q=1}^{m+1} Tr\left(\underset{=\delta}{Q} \underset{=\Delta\theta}{R} \underset{=xy,q}{\widetilde{F}} \underline{u}_{xy,p}^T \underset{=\Delta\theta}{R}^T \underset{=\delta}{P}^T \underset{=pq}{T}^T \right) \tag{14}$$

and

$$\underline{G} = \begin{bmatrix} G_I \\ G_{II} \end{bmatrix} = \frac{1}{2R_f\delta} \sum_{p=1}^{m+1} \sum_{q=1}^{m+1} Diag\left(\underset{=\delta}{Q} \underset{=\Delta\theta}{R} \underset{=xy,q}{K} \underline{u}_{xy,q} \underline{u}_{xy,p}^T \underset{=\Delta\theta}{R}^T \underset{=\delta}{P}^T \underset{=pq}{T}^T \right)$$

$$+ \frac{1}{2R_f\delta} \sum_{p=1}^{m+1} \sum_{q=1}^{m+1} Diag\left(\underset{=\delta}{Q} \underset{=\Delta\theta}{R} \underset{=N,q}{\widetilde{K}} \underline{u}_N \underline{u}_{xy,p}^T \underset{=\Delta\theta}{R}^T \underset{=\delta}{P}^T \underset{=pq}{T}^T \right) \tag{15}$$

(a) $V_f = 0.1\%$, 1st order elements.

(b) $V_f = 0.1\%$, 2nd order elements.

(c) $V_f = 40\%$, 1st order elements.

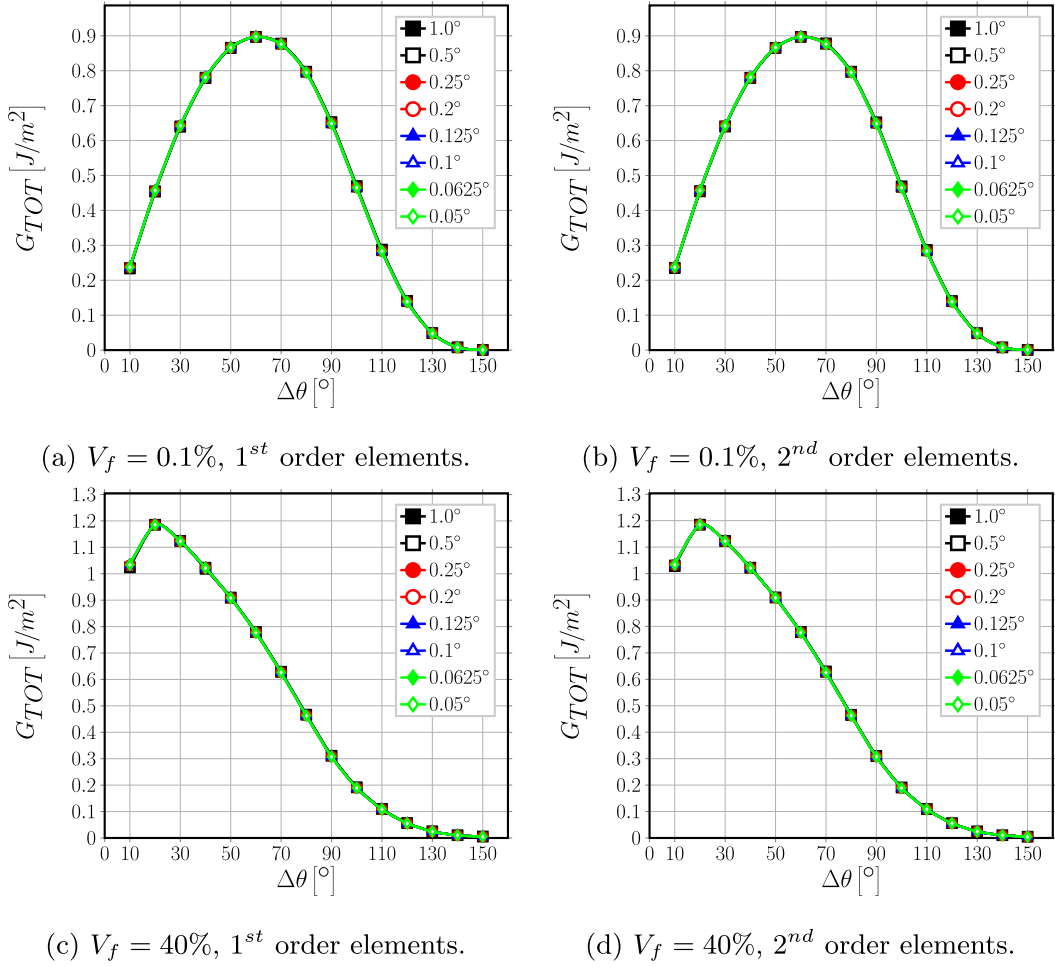(d) $V_f = 40\%$, 2nd order elements.

Fig. 6. Effect of the size δ of an element at the crack tip on total ERR.

Notice that the matrix appearing in Equation (14) and Equation (15) has the dimension of ERR, i.e. J/m^2, and is in general full. Equation (14) states that the total Energy Release Rate is the first invariant of the matrix, i.e. its trace. Equation (15) states on the other hand that the elements on its diagonal are the Mode I and Mode II ERR. The off-diagonal components represent an interaction Energy Release Rate, mention of which can be already found in Ref. [41]. However, in Ref. [41] the existence of the interaction ERR is assumed based on physical assumptions, here it is derived from the mathematical structure of the VCCT in the context of the Finite Element Method. Valvo [37,38] derives as well the existence of an interaction ERR from the presence of non-zero off-diagonal elements in his flexibility matrix. He then considers that correct Mode-decomposition is provided when the off-diagonal terms are zero and thus derives a correction to the VCCT. A different perspective is offered here. Dimensional analysis suggests that the Energy Release Rate (J/m^2), i.e. the energy required to cause a unit increase in the crack surface size, is dimensionally equivalent to the Crack Driving Force (N/m), which is the force required to grow the crack along its path by a unit length. It is then possible to infer a physical interpretation of the elements of the ERR matrix of Equation (14) and Equation (15): the diagonal elements are respectively the Mode I (Mode II) force required to propagate the crack by a unit length in Mode I (Mode II); the off-diagonal elements are respectively the Mode I (Mode II) force required to propagate the crack by a unit length in Mode II (Mode I). The off-diagonal elements capture an interaction due to Poisson's effect and the mismatch of elastic properties between phases that is peculiar of bi-material interface cracks. The assumption by Valvo

[37,38] that correct Mode-decomposition is recovered by imposing that off-diagonal elements be equal to zero seems thus open to further reflection. A deeper analysis of this issue is however beyond the scope of this paper and it will be left to a future work.

4. Rotational invariance of G_{TOT}

Recalling Equation (14) and observing that matrix $\underline{\underline{T}}_{pq}$ is always equal to the identity matrix pre-multiplied by a suitable real constant (see Eq. (B.1) in Appendix B), the total Energy Release Rate can be rewritten as

$$
\begin{aligned}
G_{TOT} &= \frac{1}{2R_f\delta} \sum_{p=1}^{m+1} \sum_{q=1}^{m+1} Tr \\
&\quad \times \left(\underline{\underline{Q}}_\delta \underline{\underline{R}}_{\Delta\theta} \left(\underline{\underline{K}}_{xy,q} \underline{u}_{xy,q} + \widetilde{\underline{F}}_{xy,q} \right) \underline{u}_{xy,p}^T \underline{\underline{T}}_{pq}^T \underline{\underline{R}}_{\Delta\theta}^T \underline{\underline{P}}_\delta^T \right) \\
&= \frac{1}{2R_f\delta} \sum_{p=1}^{m+1} \sum_{q=1}^{m+1} Tr \left(\underline{\underline{Q}}_\delta \underline{\underline{R}}_{\Delta\theta} \underline{F}_{xy,q} \underline{u}_{xy,p}^T \underline{\underline{T}}_{pq} \underline{\underline{R}}_{\Delta\theta} \underline{\underline{P}}_\delta^T \right),
\end{aligned}
\tag{16}
$$

where $\underline{F}_{xy}$ and $\underline{u}_{xy}$ are the vectors of respectively the crack tip forces and crack displacements in the global $(x - y)$ reference frame. Given that $\underline{\underline{Q}}_\delta$, $\underline{\underline{P}}_\delta$ and $\underline{\underline{R}}_{\Delta\theta}$ all represent a linear transformation (a rigid rotation in particular), the invariance of the trace to linear transformations ensures
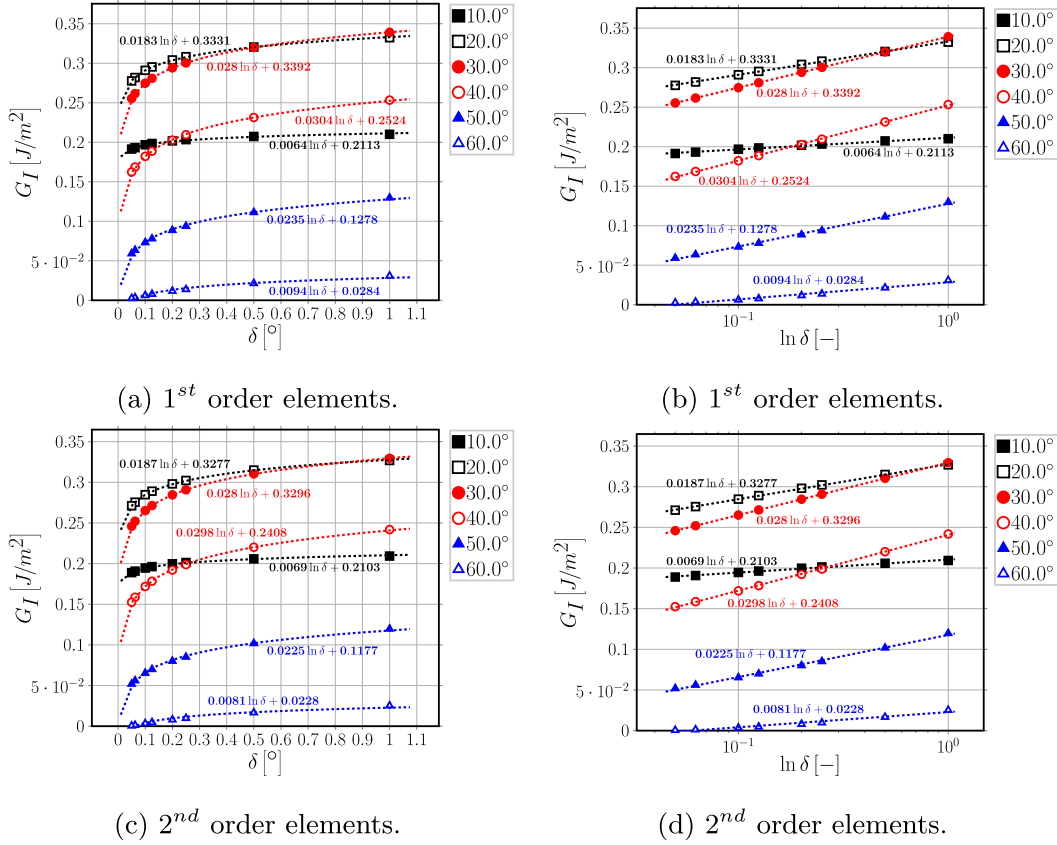
(a) 1st order elements.

(b) 1st order elements.

(c) 2nd order elements.

(d) 2nd order elements.

Fig. 7. Logarithmic dependence on δ of Mode I ERR: interpolation of numerical results for $V_f = 0.1\%$.

that

$$G_{TOT} = \frac{1}{2R_f\delta} \sum_{p=1}^{m+1} \sum_{q=1}^{m+1} Tr\left(\underline{\underline{Q}}_\delta \underline{\underline{R}}_{\Delta\theta} \underline{F}_{xy,q} \underline{u}_{xy,p}^T \underline{\underline{T}}_{pq}^T \underline{\underline{R}}_{\Delta\theta}^T \underline{\underline{P}}_\delta^T\right) =$$

$$= \frac{1}{2R_f\delta} \sum_{p=1}^{m+1} \sum_{q=1}^{m+1} Tr\left(\underline{F}_{xy,q} \underline{u}_{xy,p}^T \underline{\underline{T}}_{pq}^T\right). \tag{17}$$

As G_{TOT} was defined according to Equation (12) and given that $Tr(AB) = Tr(BA)$, it holds that

$$G_{TOT} = \frac{1}{2R_f\delta} \sum_{p=1}^{m+1} \sum_{q=1}^{m+1} \underline{u}_{r\theta,p}^T \underline{\underline{T}}_{pq}^T \underline{F}_{r\theta,q}$$

$$= \frac{1}{2R_f\delta} \sum_{p=1}^{m+1} \sum_{q=1}^{m+1} Tr\left(\underline{F}_{r\theta,q} \underline{u}_{r\theta,p}^T \underline{\underline{T}}_{pq}^T\right)$$

$$= \frac{1}{2R_f\delta} \sum_{p=1}^{m+1} \sum_{q=1}^{m+1} Tr\left(\underline{F}_{xy,q} \underline{u}_{xy,p}^T \underline{\underline{T}}_{pq}^T\right) \tag{18}$$

$$= \frac{1}{2R_f\delta} \sum_{p=1}^{m+1} \sum_{q=1}^{m+1} \underline{u}_{xy,p}^T \underline{\underline{T}}_{pq}^T \underline{F}_{xy,q}$$

which shows that the total Energy Release Rate is invariant to rigid rotations and can be calculated equivalently with forces and displacements expressed in the local crack tip reference frame or the global reference frame. The analytical result is confirmed by the numerical solution of the fiber-matrix interface crack with different element orders and model fiber volume fractions, as shown in Fig. 3.

The result of Equation (18) has also physical implications:

– given that stress and displacement fields at the crack tip are the same, two cracks with different crack paths are energeti-

cally equivalent with respect to the total Energy Release Rate;
– given that laws of the type $G_{TOT} \geq G_c$ govern crack propagation, if G_c do not depend on mode ratio, crack orientation will not affect its growth.

5. Convergence analysis

5.1. Analytical considerations

Substituting Equation (8) in the derivative of Equation (13), we can investigate the dependency of Mode I and Mode II ERR with respect to the size δ of an element in the crack tip neighborhood through

$$\frac{\partial \underline{G}}{\partial \delta} = -\frac{1}{2R_f\delta^2} \sum_{p=1}^{m+1} \sum_{q=1}^{m+1} Diag\left(\underline{\underline{Q}}_\delta \underline{\underline{R}}_{\Delta\theta} \underline{\underline{K}}_{xy} \underline{u}_{xy} \underline{u}_{xy}^T \underline{\underline{R}}_{\Delta\theta}^T \underline{\underline{P}}_\delta^T \underline{\underline{T}}_{pq}^T\right)$$

$$-\frac{1}{2R_f\delta^2} \sum_{p=1}^{m+1} \sum_{q=1}^{m+1} Diag\left(\underline{\underline{Q}}_\delta \underline{\underline{R}}_{\Delta\theta} \underline{\underline{\widetilde{K}}}_N \underline{u}_N \underline{u}_{xy}^T \underline{\underline{R}}_{\Delta\theta}^T \underline{\underline{P}}_\delta^T \underline{\underline{T}}_{pq}^T\right)$$

$$+\frac{1}{2R_f\delta} \sum_{p=1}^{m+1} \sum_{q=1}^{m+1} Diag\left(\underline{\underline{Q}}_\delta \underline{\underline{R}}_{\Delta\theta} \underline{\underline{K}}_{xy} \underline{u}_{xy} \underline{u}_{xy}^T \underline{\underline{R}}_{\Delta\theta}^T \underline{\underline{P}}_\delta^T \underline{\underline{D}}^T \underline{\underline{T}}_{pq}^T\right)$$

$$+\frac{1}{2R_f\delta} \sum_{p=1}^{m+1} \sum_{q=1}^{m+1} Diag\left(\underline{\underline{Q}}_\delta \underline{\underline{R}}_{\Delta\theta} \underline{\underline{\widetilde{K}}}_N \underline{u}_N \underline{u}_{xy}^T \underline{\underline{R}}_{\Delta\theta}^T \underline{\underline{P}}_\delta^T \underline{\underline{D}}^T \underline{\underline{T}}_{pq}^T\right)$$

$$+\frac{1}{2R_f\delta} \sum_{p=1}^{m+1} \sum_{q=1}^{m+1} Diag\left(\underline{\underline{DQ}}_\delta \underline{\underline{R}}_{\Delta\theta} \underline{\underline{K}}_{xy} \underline{u}_{xy} \underline{u}_{xy}^T \underline{\underline{R}}_{\Delta\theta}^T \underline{\underline{P}}_\delta^T \underline{\underline{T}}_{pq}^T\right)$$

$$+\frac{1}{2R_f\delta} \sum_{p=1}^{m+1} \sum_{q=1}^{m+1} Diag\left(\underline{\underline{DQ}}_\delta \underline{\underline{R}}_{\Delta\theta} \underline{\underline{\widetilde{K}}}_N \underline{u}_N \underline{u}_{xy}^T \underline{\underline{R}}_{\Delta\theta}^T \underline{\underline{P}}_\delta^T \underline{\underline{T}}_{pq}^T\right)$$

$$+ \frac{1}{2R_f\delta} \sum_{p=1}^{m+1} \sum_{q=1}^{m+1} Diag \left(\underline{\underline{Q}}_\delta \underline{\underline{R}}_{\Delta\theta} \underline{\underline{K}}_{xy} \frac{\partial \underline{u}_{xy}}{\partial \delta} \underline{u}_{xy}^T \underline{\underline{R}}_{\Delta\theta}^T \underline{\underline{P}}_\delta^T \underline{\underline{T}}_{pq}^T \right)$$

$$+ \frac{1}{2R_f\delta} \sum_{p=1}^{m+1} \sum_{q=1}^{m+1} Diag \left(\underline{\underline{Q}}_\delta \underline{\underline{R}}_{\Delta\theta} \underline{\widetilde{\underline{K}}}_N \frac{\partial \underline{u}_N}{\partial \delta} \underline{u}_{xy}^T \underline{\underline{R}}_{\Delta\theta}^T \underline{\underline{P}}_\delta^T \underline{\underline{T}}_{pq}^T \right)$$

$$+ \frac{1}{2R_f\delta} \sum_{p=1}^{m+1} \sum_{q=1}^{m+1} Diag \left(\underline{\underline{Q}}_\delta \underline{\underline{R}}_{\Delta\theta} \underline{\underline{K}}_{xy} \underline{u}_{xy} \frac{\partial \underline{u}_{xy}^T}{\partial \delta} \underline{\underline{R}}_{\Delta\theta}^T \underline{\underline{P}}_\delta^T \underline{\underline{T}}_{pq}^T \right)$$

$$+ \frac{1}{2R_f\delta} \sum_{p=1}^{m+1} \sum_{q=1}^{m+1} Diag \left(\underline{\underline{Q}}_\delta \underline{\underline{R}}_{\Delta\theta} \underline{\widetilde{\underline{K}}}_N \underline{u}_N \frac{\partial \underline{u}_{xy}^T}{\partial \delta} \underline{\underline{R}}_{\Delta\theta}^T \underline{\underline{P}}_\delta^T \underline{\underline{T}}_{pq}^T \right); \tag{19}$$

which, after refactoring, provides

$$\frac{\partial \underline{G}}{\partial \delta} = \frac{1}{\delta} \underline{G} + \frac{1}{2R_f\delta} \sum_{p=1}^{m+1} \sum_{q=1}^{m+1} Diag$$

$$\times \left(\underline{\underline{Q}}_\delta \underline{\underline{R}}_{\Delta\theta} \left(\underline{\underline{K}}_{xy} \underline{u}_{xy} + \underline{\widetilde{\underline{K}}}_N \underline{u}_N \right) \underline{u}_{xy}^T \underline{\underline{R}}_{\Delta\theta}^T \underline{\underline{P}}^T \underline{\underline{D}} \underline{\underline{T}}_{pq}^T \right)$$

$$+ \frac{1}{2R_f\delta} \sum_{p=1}^{m+1} \sum_{q=1}^{m+1} Diag$$

$$\times \left(\underline{\underline{D}}\underline{\underline{Q}}_\delta \underline{\underline{R}}_{\Delta\theta} \left(\underline{\underline{K}}_{xy} \underline{u}_{xy} + \underline{\widetilde{\underline{K}}}_N \underline{u}_N \right) \underline{u}_{xy}^T \underline{\underline{R}}_{\Delta\theta}^T \underline{\underline{P}}_\delta^T \underline{\underline{T}}_{pq}^T \right)$$

$$+ \frac{1}{R_f\delta} \sum_{p=1}^{m+1} \sum_{q=1}^{m+1} Diag \left(\underline{\underline{Q}}_\delta \underline{\underline{R}}_{\Delta\theta} \underline{\underline{K}}_{xy} \frac{\partial \underline{u}_{xy}}{\partial \delta} \underline{u}_{xy}^T \underline{\underline{R}}_{\Delta\theta}^T \underline{\underline{P}}_\delta^T \underline{\underline{T}}_{pq}^T \right)$$

$$+ \frac{1}{2R_f\delta} \sum_{p=1}^{m+1} \sum_{q=1}^{m+1} Diag \left(\underline{\underline{Q}}_\delta \underline{\underline{R}}_{\Delta\theta} \underline{\widetilde{\underline{K}}}_N \frac{\partial \underline{u}_N}{\partial \delta} \underline{u}_{xy}^T \underline{\underline{R}}_{\Delta\theta}^T \underline{\underline{P}}_\delta^T \underline{\underline{T}}_{pq}^T \right)$$

$$+ \frac{1}{2R_f\delta} \sum_{p=1}^{m+1} \sum_{q=1}^{m+1} Diag \left(\underline{\underline{Q}}_\delta \underline{\underline{R}}_{\Delta\theta} \underline{\widetilde{\underline{K}}}_N \underline{u}_N \frac{\partial \underline{u}_{xy}^T}{\partial \delta} \underline{\underline{R}}_{\Delta\theta}^T \underline{\underline{P}}_\delta^T \underline{\underline{T}}_{pq}^T \right). \tag{20}$$

Following the asymptotic analysis of [1,3], in the case of an *open crack* the displacement in the crack tip neighborhood will have a functional form of the type

$$u(\delta) \sim \sqrt{\delta} (\sin, \cos) (\epsilon \log \delta) \quad \text{with} \quad \epsilon = \frac{1}{2\pi} \log \left(\frac{1-\beta}{1+\beta} \right) \tag{21}$$

and β is Dundurs' parameter introduced in Section 1. Application of Equation (21) to the terms on the right hand side of Eq. (20) provides:

$$\underline{u}_{xy}, \underline{u}_N \sim u(\delta) \sim \sqrt{\delta} (\sin, \cos) (\epsilon \log \delta) \xrightarrow{\delta \to 0} 0; \tag{22}$$

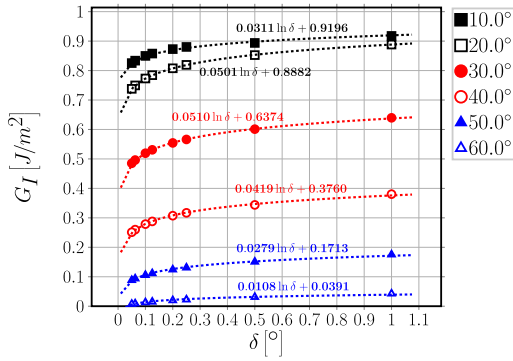$$\underline{u}_{xy}\underline{u}_{xy}^T, \underline{u}_N\underline{u}_{xy}^T \sim u^2(\delta) \sim \delta (\sin^2, \cos^2, \sin \cdot \cos) (\epsilon \log \delta) \xrightarrow{\delta \to 0} 0; \tag{23}$$

$$\frac{\partial \underline{u}_{xy}}{\partial \delta} \underline{u}_{xy}^T, \frac{\partial \underline{u}_N}{\partial \delta} \underline{u}_{xy}^T \sim -\frac{1}{2} (\sin^2, \cos^2, \sin \cdot \cos) (\epsilon \log \delta)$$

$$+ (-\sin^2, \cos^2, \pm \sin \cdot \cos) (\epsilon \log \delta) \xrightarrow{\delta \to 0} finite; \tag{24}$$
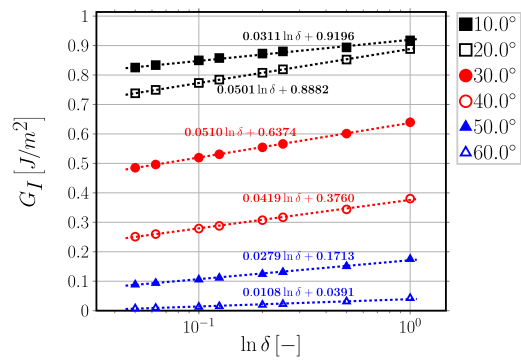
$$\underline{G} \sim \frac{1}{\delta} \underline{u}_{xy}\underline{u}_{xy}^T \sim \frac{1}{\delta} u^2(\delta) \sim (\sin^2, \cos^2, \sin \cdot \cos) (\epsilon \log \delta) \xrightarrow{\delta \to 0} finite. \tag{25}$$

In Equations (22)–(25), the multiplication by a trigonometric function of the type $(\sin, \cos, \sin^2, \cos^2, \sin \cdot \cos)$ prevents the divergence of the asymptote. Recalling Eqs. (5) and (6), in the limit of $\delta \to 0$ the rotation matrices become equal to the identity matrix:
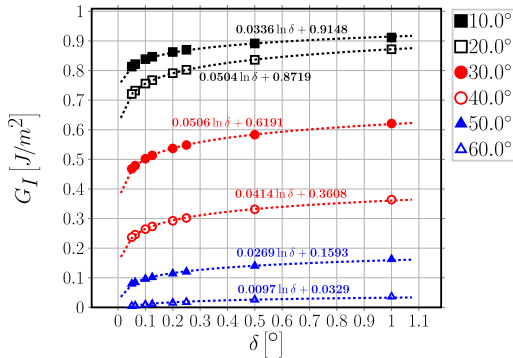
$$\underline{\underline{P}}_\delta, \underline{\underline{Q}}_\delta \xrightarrow{\delta \to 0} \begin{bmatrix} 1 & 0 \\ 0 & 1 \end{bmatrix}. \tag{26}$$

(a) 1st order elements.
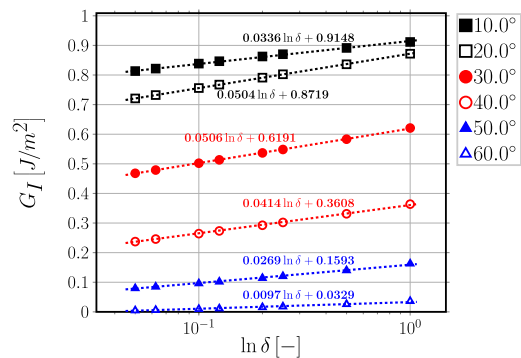

(b) 1st order elements.

(c) 2nd order elements.

(d) 2nd order elements.

Fig. 8. Logarithmic dependence on δ of Mode I ERR: interpolation of numerical results for $V_f = 40\%$.

(a) 1st order elements.

(b) 1st order elements.

(c) 2nd order elements.
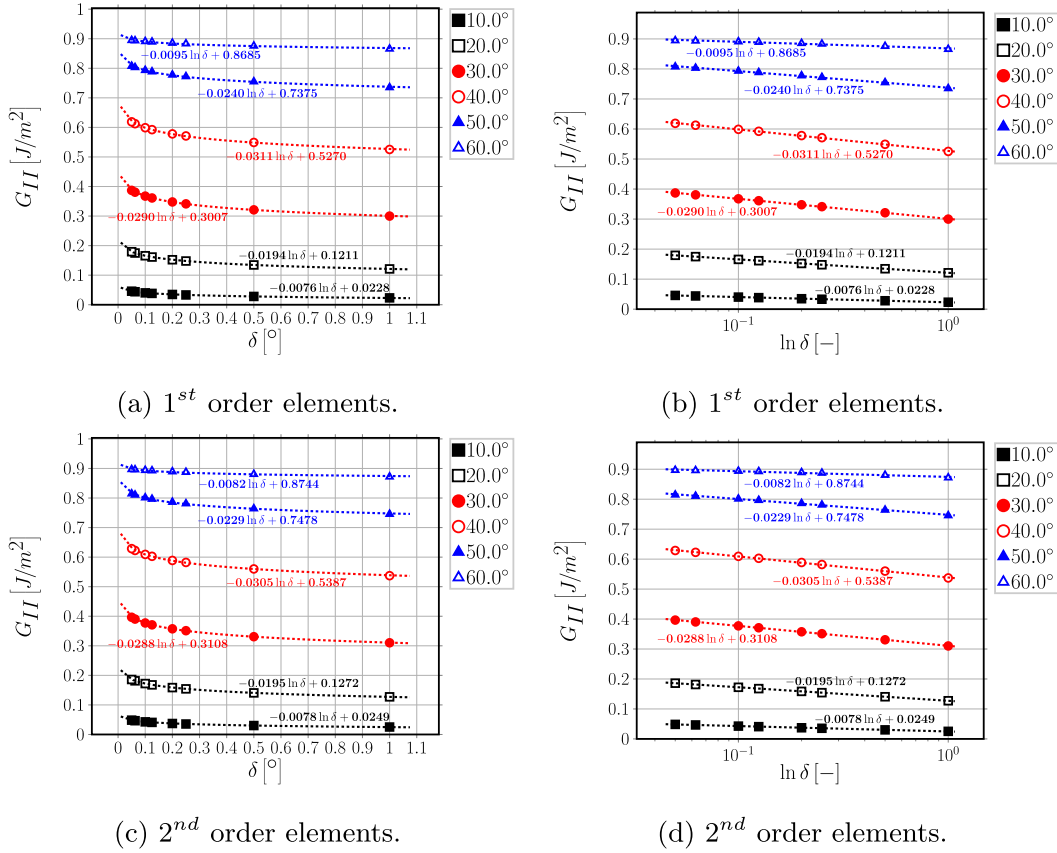

(d) 2nd order elements.

Fig. 9. Logarithmic dependence on δ of Mode II ERR: interpolation of numerical results for $V_f = 0.1\%$.

Applying the results of Equations (22)–(26) to Eq. (20), it can be shown that the derivative of $\underline{G}$ can be split in a factor that goes to 0 in the limit of $\delta \to 0$ and in a factor independent of δ:

$$\lim_{\delta \to 0} \frac{\partial \underline{G}}{\partial \delta} \sim \frac{1}{\delta} \left(\cancelto{0}{\underline{F(\delta)}} + \underline{C} \right). \tag{27}$$

Thus, asymptotically, the Mode I and Mode II Energy Release Rate behave like the logarithm of the angular size δ of the elements in the crack tip neighborhood:

$$\lim_{\delta \to 0} \frac{\partial \underline{G}}{\partial \delta} \sim \frac{1}{\delta} \xrightarrow{\int d\delta} \lim_{\delta \to 0} \underline{G} \sim \underline{A} \log(\delta) + \underline{B}. \tag{28}$$

5.2. Numerical results

Evaluations of the Mode I, Mode II and total Energy Release Rate using the VCCT applied to the FE solution of the fiber-matrix interface crack in the single fiber model of Sec. 2 are reported respectively in Figs. 4–6.

Results for Mode I ERR in Fig. 4 show clearly the transition from the *open* crack regime, where Mode I ERR is different from zero, to the *closed* crack regime of the debond, where $G_I = 0$. Looking at Fig. 4, the crack is *open* for $\Delta\theta \leq 60°$ and it is *closed*, i.e. a contact zone is present, for $\Delta\theta \geq 70°$. As expected from the analysis of the previous section, and given that Mode I ERR is different from zero only in the *open* crack regime, a significant dependence on the element size δ can be observed in Fig. 4 when using both 1st and 2nd order elements and with both an effectively infinite ($V_f = 0.1\%$) and finite size ($V_f = 40\%$) matrix. At first sight, it is immediate to see from Fig. 4 that a decrease in δ leads to a decrease in G_I. However, two further effects can be observed due to the refinement of the mesh at the crack tip, i.e. the decrease of the element size δ. First, the occurrence of the peak G_I is shifted to

lower angles for very low volume fractions: it occurs at $\Delta\theta = 30°$ with $\delta = 1.0°, 0.5°$ and at $\Delta\theta = 20°$ with $\delta \leq 0.25°$ for both 1st and 2nd order elements and $V_f = 0.1\%$. Second, the appearance of the contact zone, i.e. the switch to the *closed* crack regime, is anticipated to smaller debonds: it occurs at $\Delta\theta = 70°$ with $\delta \geq 0.2°$ and at $\Delta\theta = 60°$ with $\delta < 0.2°$ for both 1st and 2nd order elements and both $V_f = 0.1\%$ and $V_f = 40\%$.

Observing Fig. 5, it possible to notice the existence of two distinct regimes in the behavior of G_{II} with respect to the element size δ. For $\Delta\theta \leq 60° G_{II}$ depends on the value of δ, while $\Delta\theta \geq 70°$ it is effectively independent of the element size at the crack tip for both 1st and 2nd order elements and both an effectively infinite ($V_f = 0.1\%$) and finite size ($V_f = 40\%$) matrix. Comparing the value of $\Delta\theta$ at which the change from the δ-dependency regime to the δ-independency regime occurs for G_{II} with Mode I ERR in Fig. 4, it is possible to observe that the δ-dependency regime change of Mode II ERR coincides with the onset of the contact zone, i.e. the transition from *open* crack regime to the *closed* crack regime. The result confirms the analytical considerations of the previous section: for an *open* crack both Mode I and Mode II ERR depend on the element size δ at the crack tip.

Further observation of Fig. 5 reveals that, in the *open* crack regime, decreasing the element size δ causes an increase of Mode II ERR. Similarly to Mode I ERR, a shift of the peak G_{II} can also observed for $V_f = 0.1\%$: the maximum value of G_{II} occurs at $\Delta\theta = 70°$ for $\delta > 0.25°$ for 1st order elements and for $\delta > 0.5°$ for 2nd order elements, while it is shifted to $\Delta\theta = 60°$ for $\delta \leq 0.25°$ for 1st order elements and for $\delta \leq 0.5°$ for 2nd order elements.

Analysis of the total ERR in Fig. 6 leads to an observation that was not predicted by the considerations of the previous section: G_{TOT} is effectively independent of the element size δ in both the *open* and the *closed* crack regimes, at least for reasonably small elements ($\delta \leq 1.0°$). Given that $G_{II} = G_{TOT}$ for the *closed* crack, it explains the independency of G_{II} from δ after the onset of the contact zone.
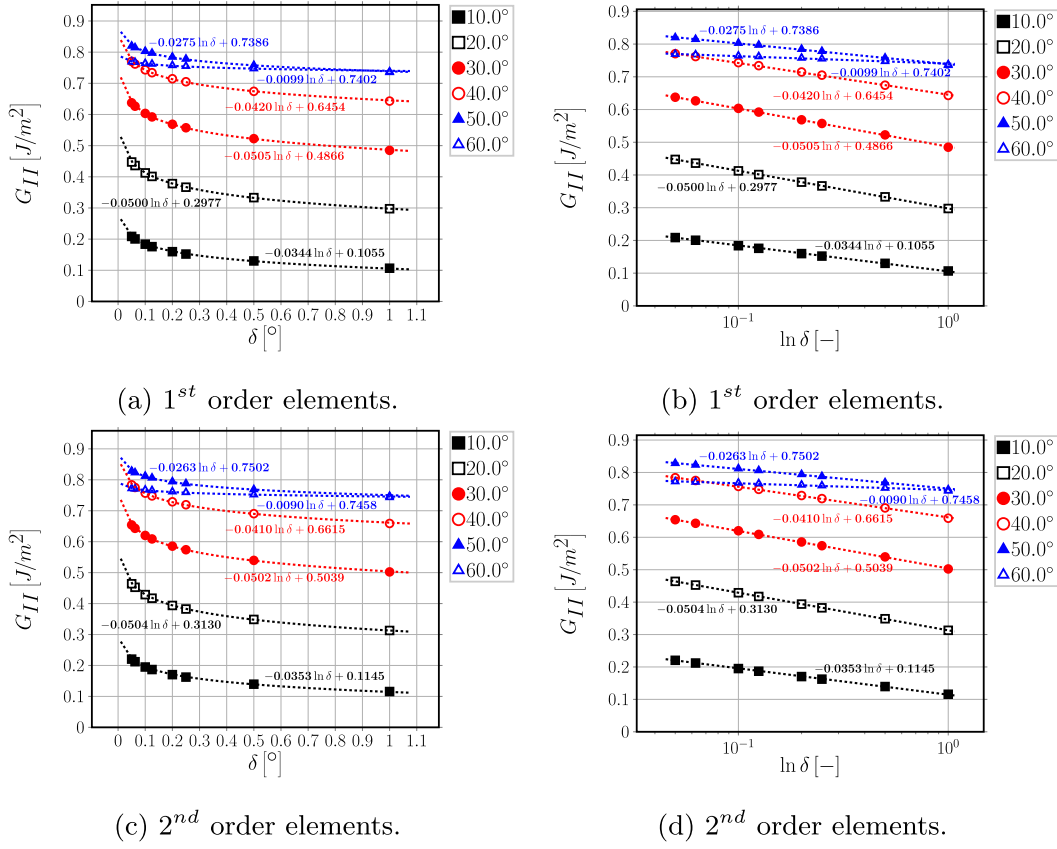
(a) 1st order elements.

(b) 1st order elements.

(c) 2nd order elements.

(d) 2nd order elements.

Fig. 10. Logarithmic dependence on δ of Mode II ERR: interpolation of numerical results for $V_f = 40\%$.

Table 2
Summary of linear regression results and main statistical tests for Mode I ERR.

$V_{f[\%]}$	Order	$\Delta\theta[°]$	$A\left[\frac{J}{m}^2\right]$	$B\left[\frac{J}{m}^2\right]$	$r[-]$	$r^{2[-]}$	$p(A)[-]$	$p(B)[-]$
0.1	1	10.0	0.0064	0.2113	0.9933	0.9866	7.48E-07	3.49E-14
		20.0	0.0183	0.3331	0.9996	0.9992	1.44E-10	2.40E-16
		30.0	0.0280	0.3392	1.0000	1.0000	2.25E-16	4.26E-21
		40.0	0.0304	0.2524	0.9997	0.9995	4.38E-11	7.94E-15
		50.0	0.0235	0.1278	0.9985	0.9970	8.61E-09	2.01E-11
		60.0	0.0094	0.0284	0.9854	0.9709	7.75E-06	6.14E-07
0.1	2	10.0	0.0069	0.2103	0.9962	0.9924	1.36E-07	1.03E-14
		20.0	0.0187	0.3277	0.9997	0.9994	7.85E-11	1.62E-16
		30.0	0.0280	0.3296	1.0000	1.0000	3.28E-16	7.29E-21
		40.0	0.0298	0.2408	0.9997	0.9995	4.82E-11	1.04E-14
		50.0	0.0225	0.1177	0.9984	0.9967	1.10E-08	3.27E-11
		60.0	0.0081	0.0228	0.9811	0.9626	1.66E-05	2.17E-06
40	1	10.0	0.0311	0.9196	0.9963	0.9927	1.03E-07	9.33E-15
		20.0	0.0501	0.8882	1.0000	0.9999	1.21E-13	2.33E-19
		30.0	0.0510	0.6374	0.9998	0.9996	1.66E-11	2.58E-16
		40.0	0.0419	0.3760	0.9988	0.9976	4.56E-09	5.25E-13
		50.0	0.0279	0.1713	0.9980	0.9961	2.22E-08	2.52E-11
		60.0	0.0108	0.0391	0.9901	0.9804	3.44E-06	9.46E-08
40	2	10.0	0.0336	0.9148	0.9988	0.9977	3.45E-09	5.09E-16
		20.0	0.0504	0.8719	1.0000	1.0000	3.70E-14	8.26E-20
		30.0	0.0506	0.6191	0.9999	0.9997	7.63E-12	1.35E-16
		40.0	0.0414	0.3608	0.9994	0.9989	4.95E-10	6.80E-14
		50.0	0.0269	0.1593	0.9982	0.9964	1.66E-08	2.31E-11
		60.0	0.0097	0.0329	0.9890	0.9781	4.96E-06	1.99E-07

Analysis of Figs. 4–6 has shown the dependency of Mode I and Mode II ERR on the element size δ. Following the derivations of the previous section, we model the dependency of G_I and G_{II} with respect to δ as

$$G_{(\cdot)} = A(\Delta\theta)\ln\delta + B(\Delta\theta),\qquad(29)$$

where $A(\Delta\theta)$ and $B(\Delta\theta)$ are parameters dependent on $\Delta\theta$ estimated through linear regression (with $x = \ln\delta$) of the numerical results.

As shown in Figs. 7–10 both in linear and logarithmic scales of δ, the result is remarkable: both the correlation coefficient r and the r^2 ratio (of explained to total variance) are always greater than 0.95 and the p-values of the coefficients A and B are at least $< 1E - 6$ and often $< 1E - 11$ (see Table 2 for G_I and Table 3 for G_{II}). The results of the linear regression confirm the analytical derivations of the previous section, which showed the logarithmic behavior of Mode I and

11

Table 3
Summary of linear regression results and main statistical tests for Mode II ERR.

$V_{f[\%]}$	Order	$\Delta\theta$ [°]	$A\left[\frac{J}{m}^2\right]$	$B\left[\frac{J}{m}^2\right]$	r [−]	r^2 [−]	p(A) [−]	p(B) [−]
0.1	1.0	10.0	−0.0076	0.0228	−0.9996	0.9991	2.09E-10	1.64E-11
		20.0	−0.0194	0.1211	−1.0000	1.0000	1.99E-15	2.02E-18
		30.0	−0.0290	0.3007	−0.9999	0.9998	4.12E-12	1.97E-16
		40.0	−0.0311	0.5270	−0.9995	0.9989	4.13E-10	1.05E-15
		50.0	−0.0240	0.7375	−0.9979	0.9958	2.32E-08	1.66E-15
		60.0	−0.0095	0.8685	−0.9835	0.9672	1.12E-05	1.22E-15
0.1	2.0	10.0	−0.0078	0.0249	−0.9996	0.9992	1.91E-10	1.06E-11
		20.0	−0.0196	0.1272	−1.0000	1.0000	3.48E-15	2.78E-18
		30.0	−0.0288	0.3108	−0.9999	0.9998	1.45E-12	5.47E-17
		40.0	−0.0305	0.5387	−0.9995	0.9990	3.32E-10	6.55E-16
		50.0	−0.0229	0.7478	−0.9979	0.9959	2.17E-08	1.09E-15
		60.0	−0.0082	0.8744	−0.9806	0.9615	1.81E-05	8.26E-16
40.0	1.0	10.0	−0.0344	0.1055	−0.9997	0.9995	3.82E-11	2.73E-12
		20.0	−0.0500	0.2977	−1.0000	0.9999	4.22E-14	5.66E-17
		30.0	−0.0505	0.4866	−0.9999	0.9997	6.44E-12	4.82E-16
		40.0	−0.0420	0.6454	−0.9996	0.9991	2.12E-10	9.66E-16
		50.0	−0.0275	0.7386	−0.9985	0.9971	9.01E-09	1.44E-15
		60.0	−0.0099	0.7402	−0.9926	0.9853	1.41E-06	5.13E-16
40.0	2.0	10.0	−0.0353	0.1145	−0.9998	0.9995	2.92E-11	1.50E-12
		20.0	−0.0504	0.3130	−1.0000	0.9999	4.00E-14	4.17E-17
		30.0	−0.0502	0.5039	−0.9999	0.9998	2.87E-12	1.69E-16
		40.0	−0.0410	0.6615	−0.9996	0.9992	2.02E-10	6.89E-16
		50.0	−0.0263	0.7502	−0.9987	0.9973	6.87E-09	7.76E-16
		60.0	−0.0090	0.7458	−0.9921	0.9842	1.79E-06	3.37E-16

Mode II ERR. Similar conclusions were reached in Refs. [29,31] for a straight bi-material crack with respect to the parameter $\Delta a/a$; however, no functional expression of $G_{(\cdot)}$ was proposed.

6. Conclusions & outlook

The application of the Virtual Crack Closure Technique to the calculation of Mode I, Mode II and total Energy Release Rate was analyzed in the context of the Finite Element solution of the bi-material circular arc crack, or fiber-matrix interface crack. A synthetic vectorial formulation of the VCCT has been proposed and its usefulness exemplified in the analysis of the mesh dependency. By both analytical considerations and numerical simulations, it has been shown that:

- the total ERR is invariant to rotations of the reference frame (and more in general to linear transformations), which implies that rotation of crack tip forces and displacement is actually not required in the use of the VCCT for the calculation of G_{TOT};
- the total ERR does not depend on the size δ of the elements at the crack tip, at least for reasonably small elements ($\delta \leq 1.0°$);
- as a consequence, Mode II ERR for the *closed* interface crack does not depend on δ, as $G_{II} = G_{TOT}$ after the onset of the contact zone;
- for the *open* interface crack, Mode I and Mode II ERR depend on the element size δ through a logarithmic law of the type $A(\Delta\theta)\ln\delta + B(\Delta\theta)$;
- the sign of the logarithm is always positive for G_I, i.e. it decreases when δ decreases, and negative for G_{II}, i.e. it increases when δ decreases.

The conclusion is significant: as the behavior of Mode I and Mode II is logarithmic with respect to mesh size, there exists no asymptotic limit and thus no convergence of the values. A convergence analysis based on the reduction of the error between successive iterations would not provide a reliable assessment of the accuracy of the FE solution of Mode I and Mode II Energy Release Rate of the fiber-matrix interface crack. A validation is thus required with respect to data obtained through a different method, be it analytical, numerical or experimental.

tal. Moreover, it has been shown that: first, the same behavior appears when using 1st as well as 2nd order elements; second, no improvement is expected with the use of singular elements, as the logarithmic dependency of G_I and G_{II} is governed by the definition of ERR itself together with the asymptotic behavior of the displacement field at the crack tip. These two conclusions put into discussion recommendations often provided by manuals of commercial FEM packages such as Abaqus [36]. The latter for example, in the context of VCCT-based crack propagation (Section 11.4.2 of the *Abaqus Analysis User's Guide*), suggests that *in most cases mesh refinement will help with obtaining a realistic result,* that *results with nonlinear materials are more sensitive to meshing than results with small-strain linear elasticity* and that *first-order elements generally work best for crack propagation analysis*. The previous considerations might apply for cracks in isotropic mediums; however, the VCCT-based crack propagation technique is proposed in Abaqus as a suitable technique for surface-based simulation of bi-material interface debonding. We have shown that, for a circular interface crack: mesh-refinement (h-refinement) does not guarantee convergence of Mode I and Mode II ERR, as their dependency on element size is logarithmic; sensitivity to meshing is actually very significant in small-strain linear elasticity and depends on the nature of the linear elastic solution at the crack tip; no difference in convergence trends is observable between first and second order elements (p-refinement). This closing considerations are not meant to be a critique *per se* to commercial software, but rather as a source of reflection on the best use of software tools. Apart from the scientific merit of the results proposed, the conclusions presented here stand as an invitation to the practitioner to avoid black-box thinking and blind application of built-in software solutions.

Declaration of competing interest

No conflict of interests exists.

Acknowledgements

Appendix A. Derivation of the relationship between crack tip forces and displacements for first order quadrilateral elements

Appendix A.1. Foundational relations

We review and present in this Section the foundational relations of the isoparametric formulation of the Finite Element Method. The objective here is to provide a theoretical foundation to the expressions in Equation (10) and Equation (11) and a reference for the explicit calculation of the nodal stiffness matrices proposed in Eq. (10) and Eq. (11). We propose a general treatment, valid for 2- and 3-dimensional problems, so that the interested reader could evaluate the nodal stiffness matrices for both a 2- and a 3-dimensional crack. However, in order to clarify the structure of some specific objects, we explicitly write their 2-dimensional form, which is of interest for the problem of this paper.

Denoting by d the number of geometrical dimensions of the problem ($d = 2$ in the present work), the element Jacobian J and its inverse J^{-1} can be expressed in general as

$$J_{ij} = \left(\underline{e}_{\xi_j} \right)_i = \frac{\partial x_i}{\partial \xi_j} \quad J_{ij}^{-1} = \left(e^{x_j} \right)_i = \frac{\partial \xi_i}{\partial x_j} \quad i, j = 1, \dots, d \tag{A.1}$$

where $\left(\underline{e}_{\xi_j} \right)$ and $\left(e^{x_j} \right)$ are respectively the covariant and contravariant basis vectors of the mapping between global $\{x_i\}$ and local element $\{\xi_i\}$ coordinates.

In 2D, assuming the global coordinates are $\{x, y\}$ and the local element coordinates are $\{\xi, \eta\}$, the covariant and contravariant basis vectors assume the form

$$\underline{e}_\xi = \begin{bmatrix} \dfrac{\partial x}{\partial \xi} \\ \dfrac{\partial y}{\partial \xi} \end{bmatrix} \quad \underline{e}_\eta = \begin{bmatrix} \dfrac{\partial x}{\partial \eta} \\ \dfrac{\partial y}{\partial \eta} \end{bmatrix}, \tag{A.2}$$

$$\underline{e}_x = \begin{bmatrix} \dfrac{\partial \xi}{\partial x} \\ \dfrac{\partial \eta}{\partial x} \end{bmatrix} \quad \underline{e}_y = \begin{bmatrix} \dfrac{\partial \xi}{\partial y} \\ \dfrac{\partial \eta}{\partial y} \end{bmatrix}. \tag{A.3}$$

and the element Jacobian J and its inverse J^{-1} can be computed for a 2D problem as

$$\underline{\underline{J}} = \left[\underline{e}_\xi | \underline{e}_\eta \right] = \begin{bmatrix} \dfrac{\partial x}{\partial \xi} & \dfrac{\partial x}{\partial \eta} \\ \dfrac{\partial y}{\partial \xi} & \dfrac{\partial y}{\partial \eta} \end{bmatrix} \quad \underline{\underline{J}}^{-1} = \left[\underline{e}^x | \underline{e}^y \right] = \begin{bmatrix} \dfrac{\partial \xi}{\partial x} & \dfrac{\partial \xi}{\partial y} \\ \dfrac{\partial \eta}{\partial x} & \dfrac{\partial \eta}{\partial y} \end{bmatrix}. \tag{A.4}$$

Denoting by $\underline{p}$ the $d \times 1$ position vector in global coordinates, we can formally introduce the $3(d-1) \times d$ matrix operator of partial differentiation $\underline{\underline{\widetilde{B}}}$ such that

$$\underline{\varepsilon} \left(\underline{p} \right) = \underline{\underline{\widetilde{B}}} \cdot \underline{u} \left(\underline{p} \right), \tag{A.5}$$

where $\underline{u}$ and $\underline{\varepsilon}$ are respectively the $d \times 1$ displacement vector and the $3(d-1) \times 1$ strain vector in Voigt notation. Denoting by n the number of nodes of a generic element, it holds that $n = s \times m$ where s represents the number of sides of the element (3 for a triangle, 4 for a rectangle, …) and m the order of the shape functions (1 for linear shape functions, 2 for quadratic shape functions, …). We can now introduce the $d \times d \cdot n$ matrix N of shape functions such that

$$\underline{u} = \underline{\underline{N}} \cdot \underline{u}_N, \tag{A.6}$$

where $\underline{u}_N$ is the $d \cdot n \times 1$ vector of element nodal variables. Having introduced $\underline{\underline{\widetilde{B}}}$ and $\underline{\underline{N}}$ in Equations (A.5) and (A.6) respectively, it is possible to define the $3(d-1) \times d \cdot n$ matrix $\underline{\underline{B}}$ of derivatives (with respect to global coordinates) of shape functions as

$$\underline{\underline{B}} = \underline{\underline{\widetilde{B}}} \cdot \underline{\underline{N}}. \tag{A.7}$$

We introduce the linear elastic material behavior in the form of the $3(d-1) \times 3(d-1)$ rigidity matrix $\underline{\underline{D}}$ such that

$$\underline{\sigma} = \underline{\underline{D}} \cdot \underline{\varepsilon}, \tag{A.8}$$

where $\underline{\sigma}$ the $3(d-1) \times 1$ stress vector in Voigt notation. It is finally possible to define the $n \times n$ element stiffness matrix $\underline{\underline{k}}_e$ as

$$\underline{\underline{k}}_e = \int_{V_e(x_i)} \left(\underline{\underline{B}}^T \underline{\underline{D}} \cdot \underline{\underline{B}} \right) dV_e(x_i) = \int_{V_e(\xi_i)} \left(\underline{\underline{B}}^T \underline{\underline{D}} \cdot \underline{\underline{B}} \right) \sqrt{g} dV_e(\xi_i), \tag{A.9}$$

where $g = det \left(\underline{\underline{J}}^T \underline{\underline{J}} \right)$ and V_e is the element volume. Given that isoparametric elements are always defined between -1 and 1 in each dimension, Equation (A.9) can simplified to

$$\underline{\underline{k}}_e = \int_{-1}^{1} \cdots \int_{-1}^{1} \left(\underline{\underline{B}}^T \underline{\underline{D}} \cdot \underline{\underline{B}} \right) \sqrt{g} d\xi_i, \tag{A.10}$$

which is amenable to numerical integration by means of a Gaussian quadrature of the form

$$
\underline{\underline{k}}_e \approx \underbrace{\sum_{k=1}^{N} \cdots \sum_{h=1}^{N}}_{d \text{ times}} w_k \cdots w_h \left(\underline{\underline{B}}^T \left(\xi_i \left(k, \dots, h \right) \right) \cdot \underline{\underline{D}} \cdot \underline{\underline{B}} \left(\xi_i \left(k, \dots, h \right) \right) \sqrt{g} \right), \tag{A.11}
$$

where $\xi_i(k, \dots, h)$ are the coordinates of the N Gaussian quadrature points. The element stiffness matrix as evaluated in Eq. (A.11) is in general a full symmetric matrix in the case of linear elasticity. For 2D rectangular elements with quadratic shape functions (8-nodes serendipity elements), the element stiffness matrix has the form

$$
k_e = \begin{bmatrix}
k_{e|11} & k_{e|12} & k_{e|13} & k_{e|14} & k_{e|15} & k_{e|16} & k_{e|17} & k_{e|18} \\
k_{e|12} & k_{e|22} & k_{e|23} & k_{e|24} & k_{e|25} & k_{e|26} & k_{e|27} & k_{e|28} \\
k_{e|13} & k_{e|23} & k_{e|33} & k_{e|34} & k_{e|35} & k_{e|36} & k_{e|37} & k_{e|38} \\
k_{e|14} & k_{e|24} & k_{e|34} & k_{e|44} & k_{e|45} & k_{e|46} & k_{e|47} & k_{e|48} \\
k_{e|15} & k_{e|25} & k_{e|35} & k_{e|45} & k_{e|55} & k_{e|56} & k_{e|57} & k_{e|58} \\
k_{e|16} & k_{e|26} & k_{e|36} & k_{e|46} & k_{e|56} & k_{e|66} & k_{e|67} & k_{e|68} \\
k_{e|17} & k_{e|27} & k_{e|37} & k_{e|47} & k_{e|57} & k_{e|67} & k_{e|77} & k_{e|78} \\
k_{e|18} & k_{e|28} & k_{e|38} & k_{e|48} & k_{e|58} & k_{e|68} & k_{e|78} & k_{e|88}
\end{bmatrix}. \tag{A.12}
$$

Appendix A.2. Calculation of displacements and reaction forces

With reference to Fig. A.11, we define:

$u_{x,M}$, $u_{x,F}$ the x-displacement of the nodes belonging to the free side of the first element belonging to the crack, respectively on the matrix (bulk) and fiber (inclusion) side;

$u_{y,M}$, $u_{y,F}$ the y-displacement of the nodes belonging to the free side of the first element belonging to the crack, respectively on the matrix (bulk) and fiber (inclusion) side;

$u_{r,M}$, $u_{r,F}$ the r-displacement of the nodes belonging to the free side of the first element belonging to the crack, respectively on the matrix (bulk) and fiber (inclusion) side;

$u_{\theta,M}$, $u_{\theta,F}$ the θ-displacement of the nodes belonging to the free side of the first element belonging to the crack, respectively on the matrix (bulk) and fiber (inclusion) side;

$F_{x,CT}$, $F_{y,CT}$ respectively the x- and y-component of the reaction force at the crack tip;

$F_{r,CT}$, $F_{\theta,CT}$ respectively the r- and θ-component of the reaction force at the crack tip.

The $x - y$ reference frame is the global reference frame, while the $r - \theta$ reference frame is such that the θ direction coincides with the crack propagation direction at the crack tip and r the in-plane normal to the propagation direction. For an arc-crack as the present one, the r-direction coincides with the radial direction of the inclusion.
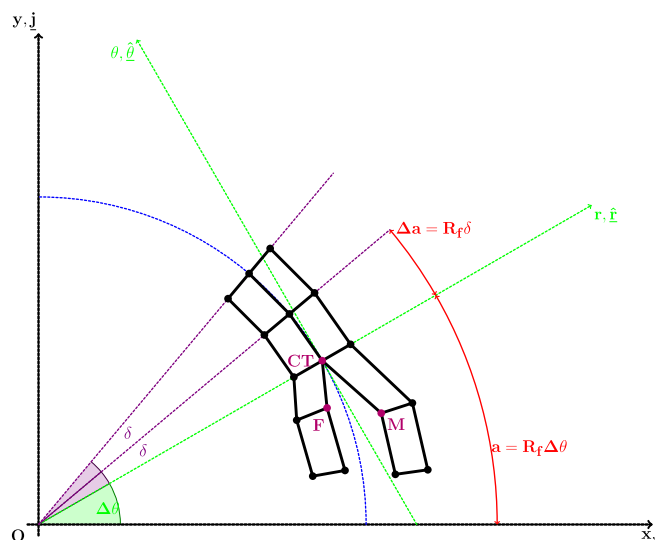

Fig. A.11 Schematic representation of the discretized crack tip geometry for 1st order quadrilateral elements.

The crack opening displacement u_r and the crack shear displacement u_θ at the crack tip can thus be written as

$$
u_r = \cos\left(\Delta\theta \right) u_x + \sin\left(\Delta\theta \right) u_y \quad u_\theta = -\sin\left(\Delta\theta \right) u_x + \cos\left(\Delta\theta \right) u_y, \tag{A.13}
$$

where u_x and u_y are defined as

$$
u_x = u_{x,M} - u_{x,F} \quad u_y = u_{y,M} - u_{y,F} \tag{A.14}
$$

and $2\Delta\theta$ is total angular size of the debond. The corresponding forces at the crack tip are

$$F_r = \cos(\Delta\theta) F_{x,CT} + \sin(\Delta\theta) F_{y,CT} \quad F_\theta = -\sin(\Delta\theta) F_{x,CT} + \cos(\Delta\theta) F_{y,CT}. \tag{A.15}$$

At the crack tip, the FE mesh possesses two coincident points, labeled *FCT* and *MCT*. Continuity of the displacements at the crack tip must be ensured. Furthermore, in order to measure the force at the crack tip, a fully-constraint dummy node needs to be created and formally linked to the two nodes at the crack tip by the conditions

$$\begin{cases} u_{x,FCT} - u_{x,MCT} - u_{x,DUMMY} = 0 \\ u_{y,FCT} - u_{y,MCT} - u_{y,DUMMY} = 0 \\ u_{x,DUMMY} = 0 \\ u_{y,DUMMY} = 0 \end{cases}, \tag{A.16}$$

which can be simplified to

$$\begin{cases} u_{x,FCT} = u_{x,MCT} \\ u_{y,FCT} = u_{y,MCT} \\ R_{x,DUMMY} = R_{x,FCT} = -R_{x,MCT} = F_{x,CT} \\ R_{y,DUMMY} = R_{y,FCT} = -R_{y,MCT} = F_{y,CT} \end{cases}. \tag{A.17}$$

Making use of Eq. (A.12), four equations can be written in the four displacement $u_{x,FCT}$, $u_{x,MCT}$, $u_{y,FCT}$ and $u_{y,MCT}$:

$$\begin{cases} (k_{e,M|11} + k_{e,M|33}) u_{x,MCT} + (k_{e,M|12} + k_{e,M|34}) u_{y,MCT} \\ + k_{e,M|13} u_{x,M} + k_{e,M|14} u_{y,M} + (k_{M|17} + k_{M|35}) u_{N,MC|7} + (k_{M|18} + k_{M|36}) u_{N,MC|8} \\ + \sum_{i=5}^{6} k_{M|1i} u_{N,MC|i} + \sum_{i=7}^{8} k_{M|3i} u_{N,MB|i} + k_{M|31} u_{x,NCOI} + k_{M|32} u_{y,NCOI} = 0 \\ (k_{e,M|21} + k_{e,M|43}) u_{x,MCT} + (k_{e,M|22} + k_{e,M|44}) u_{y,MCT} \\ + k_{e,M|23} u_{x,M} + k_{e,M|24} u_{y,M} + (k_{M|27} + k_{M|45}) u_{N,MC|7} + (k_{M|28} + k_{M|46}) u_{N,MC|8} \\ + \sum_{i=5}^{6} k_{M|2i} u_{N,MC|i} + \sum_{i=7}^{8} k_{M|4i} u_{N,MB|i} + k_{M|41} u_{x,NCOI} + k_{M|42} u_{y,NCOI} = 0 \\ (k_{e,F|77} + k_{e,F|55}) u_{x,FCT} + (k_{e,F|78} + k_{e,F|56}) u_{y,FCT} \\ + k_{e,F|75} u_{x,F} + k_{e,F|76} u_{y,F} + (k_{F|71} + k_{F|53}) u_{N,FC|1} + (k_{F|72} + k_{F|54}) u_{N,FC|2} \\ + \sum_{i=2}^{3} k_{F|7i} u_{N,FC|i} + \sum_{i=1}^{2} k_{F|5i} u_{N,FB|i} + k_{F|57} u_{x,NCOI} + k_{F|58} u_{y,NCOI} = 0 \\ (k_{e,F|87} + k_{e,F|65}) u_{x,FCT} + (k_{e,F|88} + k_{e,F|66}) u_{y,FCT} \\ + k_{e,F|85} u_{x,F} + k_{e,F|86} u_{y,F} + (k_{F|81} + k_{F|63}) u_{N,FC|1} + (k_{F|82} + k_{F|64}) u_{N,FC|2} \\ + \sum_{i=2}^{3} k_{F|8i} u_{N,FC|i} + \sum_{i=1}^{2} k_{F|6i} u_{N,FB|i} + k_{F|67} u_{x,NCOI} + k_{F|68} u_{y,NCOI} = 0 \end{cases}. \tag{A.18}$$

Solving for $u_{y,FCT}$ and $u_{y,MCT}$ the third and fourth relations in Eq. (A.18) and substituting in the first two expressions of Eq. (A.18), we get

$$\begin{cases} (k_{e,M|11} + k_{e,M|33} + k_{e,F|77} + k_{e,F|55}) u_{x,MCT} + (k_{e,M|12} + k_{e,M|34} + k_{e,F|78} + k_{e,F|56}) u_{y,MCT} + \\ + k_{e,M|13} u_{x,M} + k_{e,M|14} u_{y,M} + k_{e,F|75} u_{x,F} + k_{e,F|76} u_{y,F} + \\ + (k_{M|31} + k_{F|57}) u_{x,NCOI} + (k_{M|32} + k_{F|58}) u_{y,NCOI} + \\ + (k_{M|17} + k_{M|35}) u_{N,MC|7} + (k_{M|18} + k_{M|36}) u_{N,MC|8} + (k_{F|71} + k_{F|53}) u_{N,FC|1} + (k_{F|72} + k_{F|54}) u_{N,FC|2} + \\ + \sum_{i=5}^{6} k_{M|1i} u_{N,MC|i} + \sum_{i=7}^{8} k_{M|3i} u_{N,MB|i} + \sum_{i=2}^{3} k_{F|7i} u_{N,FC|i} + \sum_{i=1}^{2} k_{F|5i} u_{N,FB|i} = 0 \\ \\ (k_{e,M|21} + k_{e,M|43} + k_{e,F|87} + k_{e,F|65}) u_{x,MCT} + (k_{e,M|22} + k_{e,M|44} + k_{e,F|88} + k_{e,F|66}) u_{y,MCT} + \\ + k_{e,M|23} u_{x,M} + k_{e,M|24} u_{y,M} + k_{e,F|85} u_{x,F} + k_{e,F|86} u_{y,F} + \\ + (k_{M|41} + k_{F|67}) u_{x,NCOI} + (k_{M|42} + k_{F|68}) u_{y,NCOI} + \\ + (k_{M|27} + k_{M|45}) u_{N,MC|7} + (k_{M|28} + k_{M|46}) u_{N,MC|8} + (k_{F|81} + k_{F|63}) u_{N,FC|1} + (k_{F|82} + k_{F|64}) u_{N,FC|2} + \\ + \sum_{i=2}^{3} k_{F|8i} u_{N,FC|i} + \sum_{i=1}^{2} k_{F|6i} u_{N,FB|i} + \sum_{i=5}^{6} k_{M|2i} u_{N,MC|i} + \sum_{i=7}^{8} k_{M|4i} u_{N,MB|i} = 0 \end{cases} \tag{A.19}$$

Solving the system of two equations and observing that $u_{x,F}, u_{y,F} \sim 0$ for a stiffer inclusion as a fiber in a polymeric composite, we can express $u_{x,MCT}$ as a function of u_x and u_y (see Eq. (A.14)) as

$$\left[\left(k_{e,M|21} + k_{e,M|43} + k_{e,F|87} + k_{e,F|65} \right) + \frac{k_{e,M|11} + k_{e,M|33} + k_{e,F|77} + k_{e,F|55}}{k_{e,M|12} + k_{e,M|34} + k_{e,F|78} + k_{e,F|56}} \left(k_{e,M|22} + k_{e,M|44} + k_{e,F|88} + k_{e,F|66} \right) \right] u_{x,MCT} +$$

$$+ \left(k_{e,M|23} - \frac{k_{e,M|22} + k_{e,M|44} + k_{e,F|88} + k_{e,F|66}}{k_{e,M|12} + k_{e,M|34} + k_{e,F|78} + k_{e,F|56}} k_{e,M|13} \right) u_x +$$

$$+ \left(k_{e,M|24} - \frac{k_{e,M|22} + k_{e,M|44} + k_{e,F|88} + k_{e,F|66}}{k_{e,M|12} + k_{e,M|34} + k_{e,F|78} + k_{e,F|56}} k_{e,M|14} \right) u_y +$$

$$+ \left(k_{e,M|23} + k_{e,F|85} - \frac{k_{e,M|22} + k_{e,M|44} + k_{e,F|88} + k_{e,F|66}}{k_{e,M|12} + k_{e,M|34} + k_{e,F|78} + k_{e,F|56}} \left(k_{e,M|13} + k_{e,M|75} \right) \right) \underbrace{u_{x,F}}_{\approx 0} +$$

$$+ \left(k_{e,M|24} + k_{e,F|86} - \frac{k_{e,M|22} + k_{e,M|44} + k_{e,F|88} + k_{e,F|66}}{k_{e,M|12} + k_{e,M|34} + k_{e,F|78} + k_{e,F|56}} \left(k_{e,M|14} + k_{e,M|76} \right) \right) \underbrace{u_{y,F}}_{\approx 0} +$$

$$+ \left[\left(k_{M|41} + k_{F|67} \right) - \frac{k_{e,M|22} + k_{e,M|44} + k_{e,F|88} + k_{e,F|66}}{k_{e,M|12} + k_{e,M|34} + k_{e,F|78} + k_{e,F|56}} \left(k_{M|31} + k_{F|57} \right) \right] u_{x,NCOI} +$$

$$+ \left[\left(k_{M|42} + k_{F|68} \right) - \frac{k_{e,M|22} + k_{e,M|44} + k_{e,F|88} + k_{e,F|66}}{k_{e,M|12} + k_{e,M|34} + k_{e,F|78} + k_{e,F|56}} \left(k_{M|32} + k_{F|58} \right) \right] u_{y,NCOI} +$$

$$+ \left(k_{M|27} + k_{M|45} \right) u_{N,MC|7} + \left(k_{M|28} + k_{M|46} \right) u_{N,MC|8} + \left(k_{F|81} + k_{F|63} \right) u_{N,FC|1} + \left(k_{F|82} + k_{F|64} \right) u_{N,FC|2} +$$

$$- \frac{k_{e,M|22} + k_{e,M|44} + k_{e,F|88} + k_{e,F|66}}{k_{e,M|12} + k_{e,M|34} + k_{e,F|78} + k_{e,F|56}} \left[\left(k_{M|17} + k_{M|35} \right) u_{N,MC|7} + \left(k_{M|18} + k_{M|36} \right) u_{N,MC|8} \right] +$$

$$- \frac{k_{e,M|22} + k_{e,M|44} + k_{e,F|88} + k_{e,F|66}}{k_{e,M|12} + k_{e,M|34} + k_{e,F|78} + k_{e,F|56}} \left[\left(k_{F|71} + k_{F|53} \right) u_{N,FC|1} + \left(k_{F|72} + k_{F|54} \right) u_{N,FC|2} \right]$$

$$+ \sum_{i=2}^{3} k_{F|8i} u_{N,FC|i} + \sum_{i=1}^{2} k_{F|6i} u_{N,FB|i} + \sum_{i=5}^{6} k_{M|2i} u_{N,MC|i} + \sum_{i=7}^{8} k_{M|4i} u_{N,MB|i} +$$

$$- \frac{\sum_{i=5}^{6} k_{M|1i} u_{N,MC|i} + \sum_{i=7}^{8} k_{M|3i} u_{N,MB|i} + \sum_{i=2}^{3} k_{F|7i} u_{N,FC|i} + \sum_{i=1}^{2} k_{F|5i} u_{N,FB|i}}{k_{e,M|12} + k_{e,M|34} + k_{e,F|78} + k_{e,F|56}} = 0, \tag{A.20}$$

(A.20)

while the reaction forces at the crack tip can be expressed as

$$\begin{cases} F_{x,CT} &= R_{x,FCT} = \\ &= \left(k_{e,F|77} + k_{e,F|55} \right) u_{x,FCT} + \left(k_{e,F|78} + k_{e,F|56} \right) u_{y,FCT} + \\ &\quad + k_{e,F|75} \underbrace{u_{x,F}}_{\approx 0} + k_{e,F|76} \underbrace{u_{y,F}}_{\approx 0} + \\ &\quad + \sum_{i=1}^{4} k_{e,F|7i} u_{N,FC|i} + \sum_{i=1,i\neq(5,6)}^{8} k_{e,F|5i} u_{N,FB|i} \\ F_{y,CT} &= R_{y,FCT} = \\ &= \left(k_{e,F|87} + k_{e,F|65} \right) u_{x,FCT} + \left(k_{e,F|88} + k_{e,F|66} \right) u_{y,FCT} + \\ &\quad + k_{e,F|85} \underbrace{u_{x,F}}_{\approx 0} + k_{e,F|86} \underbrace{u_{y,F}}_{\approx 0} + \\ &\quad + \sum_{i=1}^{4} k_{e,F|8i} u_{N,FC|i} + \sum_{i=1,i\neq(5,6)}^{8} k_{e,F|6i} u_{N,FB|i} \end{cases} \tag{A.21}$$

Substituting Eq. (A.18) in Eqs. (A.19)–(A.21) and solving, we obtain an expression of the form

$$\begin{cases} F_{x,CT} &= K_{xx} u_x + K_{xy} u_y \\ &\quad + \sum_{i=1}^{4} K_{FC,x|i} u_{N,FC|i} + \sum_{i=1,i\neq(3,4,5,6)}^{8} K_{FB,x|i} u_{N,FB|i} \\ &\quad + \sum_{i=5}^{8} K_{FC,x|i} u_{N,MC|i} + \sum_{i=7}^{8} K_{MB,x|i} u_{N,FB|i} \\ F_{y,CT} &= K_{yx} u_x + K_{yy} u_y \\ &\quad + \sum_{i=1}^{4} K_{FC,y|i} u_{N,FC|i} + \sum_{i=1,i\neq(3,4,5,6)}^{8} K_{FB,y|i} u_{N,FB|i} \\ &\quad + \sum_{i=5}^{8} K_{FC,y|i} u_{N,MC|i} + \sum_{i=7}^{8} K_{MB,y|i} u_{N,FB|i} \end{cases}, \tag{A.22}$$

which can be reformulated synthetically as

$$\begin{cases} F_{x,CT} &= K_{xx} u_x + K_{xy} u_y + \widetilde{F}_x, \\ F_{y,CT} &= K_{yx} u_x + K_{yy} u_y + \widetilde{F}_y, \end{cases} \tag{A.23}$$

where $\widetilde{F}_x$ and $\widetilde{F}_y$ represent the influence of the FE solution through the nodes of the elements sharing the crack tip that do not belong to any of the phase interfaces, i.e. the nodes of the elements sharing the crack tip that belong to the bulk of each phase.

Appendix B. Expression of $\underset{=pq}{T}$ for quadrilateral elements with or without singularity

The expression of $\underset{=pq}{T}$ for quadrilateral elements with or without singularity is

$$\underline{\underline{T}}_{pq} = \begin{cases} \underline{\underline{I}} \ for \ p = q < 2 \\ \underline{\underline{0}} \ otherwise \end{cases}$$

$\times$ for 1st order quadrilateral elements

$$= \begin{cases} \underline{\underline{I}} \ for \ p = q < 3 \\ \underline{\underline{0}} \ otherwise \end{cases}$$

$\times$ for 2nd order quadrilateral elements

$$= \begin{cases} \underline{\underline{I}} \ for \ p = q < 4 \\ \underline{\underline{0}} \ otherwise \end{cases} \quad for \ 3^{rd} \ order \ quadrilateral \ elements$$

$$= \begin{cases} \left(14 - \frac{33\pi}{8}\right)\underline{\underline{I}} \ for \ p = 1, q = 1 \\ \left(-52 + \frac{33\pi}{2}\right)\underline{\underline{I}} \ for \ p = 1, q = 2 \\ \left(17 - \frac{21\pi}{4}\right)\underline{\underline{I}} \ for \ p = 2, q = 1 \\ \left(-\frac{7}{2} + \frac{21\pi}{16}\right)\underline{\underline{I}} \ for \ p = 2, q = 2 \\ \left(8 - \frac{21\pi}{8}\right)\underline{\underline{I}} \ for \ p = 1, q = 3 \\ \left(-32 + \frac{21\pi}{2}\right)\underline{\underline{I}} \ for \ p = 2, q = 3 \\ \underline{\underline{0}} \ otherwise \end{cases}$$

$\times$ for 2nd order quarter $-$ point quadrilateral elements   (B.1)

$$= \begin{cases} \left(-11187 + \frac{7155\pi}{2}\right)\underline{\underline{I}} \ for \ p = 1, q = 1 \\ \left(38556 - \frac{24543\pi}{2}\right)\underline{\underline{I}} \ for \ p = 1, q = 2 \\ \left(-53055 + \frac{33777\pi}{2}\right)\underline{\underline{I}} \ for \ p = 1, q = 3 \\ \left(\frac{11396}{3} - \frac{9575\pi}{8}\right)\underline{\underline{I}} \ for \ p = 2, q = 1 \\ \left(-12936 + \frac{33003\pi}{8}\right)\underline{\underline{I}} \ for \ p = 2, q = 2 \\ \left(17988 - \frac{45837\pi}{8}\right)\underline{\underline{I}} \ for \ p = 2, q = 3 \\ \left(-\frac{8453}{3} + \frac{3595\pi}{4}\right)\underline{\underline{I}} \ for \ p = 3, q = 1 \\ \left(9804 - \frac{12411\pi}{4}\right)\underline{\underline{I}} \ for \ p = 3, q = 2 \\ \left(-13587 + \frac{17289\pi}{4}\right)\underline{\underline{I}} \ for \ p = 3, q = 3 \\ \left(6948 - \frac{17685\pi}{8}\right)\underline{\underline{I}} \ for \ p = 1, q = 4 \\ \left(-23976 + \frac{60993\pi}{8}\right)\underline{\underline{I}} \ for \ p = 2, q = 4 \\ \left(33372 - \frac{84807\pi}{8}\right)\underline{\underline{I}} \ for \ p = 3, q = 4 \\ \underline{\underline{0}} \ otherwise \end{cases}$$

$\times$ for 3rd order quarter $-$ point quadrilateral elements

where $\underline{\underline{I}}$ is the identity matrix.

References

[1] M. Comninou, An overview of interface cracks, Eng. Fract. Mech. 37 (1) (1990) 197–208, https://doi.org/10.1016/0013-7944(90)90343-f.

[2] D. Hills, J. Barber, Interface cracks, Int. J. Mech. Sci. 35 (1) (1993) 27–37, https://doi.org/10.1016/0020-7403(93)90062-y.

[3] M.L. Williams, The stresses around a fault or crack in dissimilar media, Bull. Seismol. Soc. Am. 49 (2) (1959) 199.

[4] J. Dundurs, Discussion: edge-bonded dissimilar orthogonal elastic wedges under normal and shear loading (Bogy, D. B., 1968, ASME J. Appl. Mech., 35, pp. 460466), J. Appl. Mech. 36 (3) (1969) 650, https://doi.org/10.1115/1.3564739.

[5] F. Erdogan, Stress distribution in a nonhomogeneous elastic plane with cracks, J. Appl. Mech. 30 (2) (1963) 232, https://doi.org/10.1115/1.3636517.

[6] A.H. England, A crack between dissimilar media, J. Appl. Mech. 32 (2) (1965) 400, https://doi.org/10.1115/1.3625813.

[7] B. Malyshev, R. Salganik, The strength of adhesive joints using the theory of cracks, Int. J. Fract. Mech. 11 (2) (1965), https://doi.org/10.1007/bf00186749, https://doi.org/10.1007/bf00186749.

[8] M. Comninou, The interface crack, J. Appl. Mech. 44 (4) (1977) 631, https://doi.org/10.1115/1.3424148, https://doi.org/10.1115/1.3424148.

[9] A.H. England, An arc crack around a circular elastic inclusion, J. Appl. Mech. 33 (3) (1966) 637, https://doi.org/10.1115/1.3625132.

[10] A. Perlman, G. Sih, Elastostatic problems of curvilinear cracks in bonded dissimilar materials, Int. J. Eng. Sci. 5 (11) (1967) 845–867, https://doi.org/10.1016/0020-7225(67)90009-2.

[11] M. Toya, A crack along the interface of a circular inclusion embedded in an infinite solid, J. Mech. Phys. Solids 22 (5) (1974) 325–348, https://doi.org/10.1016/0022-5096(74)90002-7.

[12] F. Pars, J.C. Cao, J. Varna, The fiber-matrix interface crack a numerical analysis using boundary elements, Int. J. Fract. 82 (1) (1996) 11–29, https://doi.org/10.1007/bf00017861.

[13] G.R. Irwin, Fracture, in: Elasticity and Plasticity/Elastizitt und Plastizitt, Springer Berlin Heidelberg, 1958, pp. 551–590, https://doi.org/10.1007/978-3-642-45887-3_5.

[14] J.C.D. Cao, F. Pars, On stress singularities induced by the discretization in curved receding contact surfaces: a bem analysis, Int. J. Numer. Methods Eng. 40 (12) (1997) 2301–2320, https://doi.org/10.1002/(sici)1097-0207(19970630)40:12<2301::aid-nme166>3.0.co;2-8.

[15] J. Varna, F. Pars, J.C. Cao, The effect of crack-face contact on fiber/matrix debonding in transverse tensile loading, Compos. Sci. Technol. 57 (5) (1997) 523–532, https://doi.org/10.1016/s0266-3538(96)00175-3.

[16] F. Pars, E. Correa, V. Manti, Kinking of transversal interface cracks between fiber and matrix, J. Appl. Mech. 74 (4) (2007) 703, https://doi.org/10.1115/1.2711220.

[17] E. Correa, E. Gamstedt, F. Pars, V. Manti, Effects of the presence of compression in transverse cyclic loading on fibrematrix debonding in unidirectional composite plies, Compos. Part A Appl. Sci. Manuf. 38 (11) (2007) 2260–2269, https://doi.org/10.1016/j.compositesa.2006.11.002.

[18] E. Correa, V. Manti, F. Pars, Effect of thermal residual stresses on matrix failure under transverse tension at micromechanical level: a numerical and experimental analysis, Compos. Sci. Technol. 71 (5) (2011) 622–629, https://doi.org/10.1016/j.compscitech.2010.12.027.

[19] E. Correa, F. Pars, V. Manti, Effect of the presence of a secondary transverse load on the inter-fibre failure under tension, Eng. Fract. Mech. 103 (2013) 174–189, https://doi.org/10.1016/j.engfracmech.2013.02.026.

[20] E. Correa, F. Pars, V. Manti, Effect of a secondary transverse load on the inter-fibre failure under compression, Compos. Part B Eng. 65 (2014) 57–68, https://doi.org/10.1016/j.compositesb.2014.01.005.

[21] C. Sandino, E. Correa, F. Pars, Numerical analysis of the influence of a nearby fibre on the interface crack growth in composites under transverse tensile load, Eng. Fract. Mech. 168 (2016) 58–75, https://doi.org/10.1016/j.engfracmech.2016.01.022.

[22] C. Sandino, E. Correa, F. Pars, Interface crack growth under transverse compression: nearby fibre effect, in: Proceeding of the 18th European Conference on Composite Materials (ECCM-18), 2018.

[23] L. Zhuang, A. Pupurs, J. Varna, R. Talreja, Z. Ayadi, Effects of inter-fiber spacing on fiber-matrix debond crack growth in unidirectional composites under transverse loading, Compos. Part A Appl. Sci. Manuf. 109 (2018) 463–471, https://doi.org/10.1016/j.compositesa.2018.03.031.

[24] J. Varna, L.Q. Zhuang, A. Pupurs, Z. Ayadi, Growth and interaction of debonds in local clusters of fibers in unidirectional composites during transverse loading, Key Eng. Mater. 754 (2017) 63–66, https://doi.org/10.4028/www.scientific.net/kem.754.63.

[25] L. Zhuang, R. Talreja, J. Varna, Transverse crack formation in unidirectional composites by linking of fibre/matrix debond cracks, Compos. Part A Appl. Sci. Manuf. 107 (2018) 294–303, https://doi.org/10.1016/j.compositesa.2018.01.013.

[26] E. Rybicki, M. Kanninen, A finite element calculation of stress intensity factors by a modified crack closure integral, Eng. Fract. Mech. 9 (4) (1977) 931–938, https://doi.org/10.1016/0013-7944(77)90013-3.

[27] R. Krueger, Virtual crack closure technique: history, approach, and applications, Appl. Mech. Rev. 57 (2) (2004) 109, https://doi.org/10.1115/1.1595677.

[28] R. Krueger, K.N. Shivakumar, I.S. Raju, Fracture mechanics analyses for interface crack problems - a review, in: 54th AIAA/ASME/ASCE/AHS/ASC Structures, Structural Dynamics, and Materials Conference, American Institute of Aeronautics and Astronautics, 2013https://doi.org/10.2514/6.2013-1476.

[29] C. Sun, C. Jih, On strain energy release rates for interfacial cracks in bi-material media, Eng. Fract. Mech. 28 (1) (1987) 13–20, https://doi.org/10.1016/0013-7944(87)90115-9.

[30] C. Sun, M. Manoharan, Strain energy release rates of an interfacial crack between two orthotropic solids, J. Compos. Mater. 23 (5) (1989) 460–478, https://doi.org/10.1177/002199838902300503.

[31] M. Manoharan, C. Sun, Strain energy release rates of an interfacial crack between two anisotropic solids under uniform axial strain, Compos. Sci. Technol. 39 (2) (1990) 99–116, https://doi.org/10.1016/0266-3538(90)90049-b.

[32] I. Raju, J. Crews, M. Aminpour, Convergence of strain energy release rate components for edge-delaminated composite laminates, Eng. Fract. Mech. 30 (3) (1988) 383–396, https://doi.org/10.1016/0013-7944(88)90196-8.

[33] E. Glaessgen, W. Riddell, I. Raju, Effect of shear deformation and continuity on delamination modeling with plate elements, in: 39th AIAA/ASME/ASCE/AHS/ASC Structures, Structural Dynamics, and Materials Conference and Exhibit, American Institute of Aeronautics and Astronautics, 1998https://doi.org/10.2514/6.1998-2023.

[34] A. Agrawal, A.M. Karlsson, Obtaining mode mixity for a bimaterial interface crack using the virtual crack closure technique, Int. J. Fract. 141 (12) (2006) 75–98, https://doi.org/10.1007/s10704-006-0069-4.

[35] S. Wang, C. Harvey, L. Guan, Partition of mixed modes in layered isotropic double cantilever beams with non-rigid cohesive interfaces, Eng. Fract. Mech. 111 (2013) 1–25, https://doi.org/10.1016/j.engfracmech.2013.09.005.

[36] Simulia, Providence, RI, USA, ABAQUS/Standard User's Manual, 2012, Version 6.12.

[37] P.S. Valvo, A revised virtual crack closure technique for physically consistent fracture mode partitioning, Int. J. Fract. 173 (1) (2011) 1–20, https://doi.org/10.1007/s10704-011-9658-y.

[38] P.S. Valvo, A further step towards a physically consistent virtual crack closure technique, Int. J. Fract. 192 (2) (2015) 235–244, https://doi.org/10.1007/s10704-015-0007-4.

[39] G.R. Irwin, Analysis of stresses and strains near the end of a crack traversing a plate, J. Appl. Mech. - Trans. ASME E24 (1957) 351–369.

[40] I. Raju, Calculation of strain-energy release rates with higher order and singular finite elements, Eng. Fract. Mech. 28 (3) (1987) 251–274, https://doi.org/10.1016/0013-7944(87)90220-7.

[41] W.T. Chow, S.N. Atluri, Finite element calculation of stress intensity factors for interfacial crack using virtual crack closure integral, Comput. Mech. 16 (6) (1995) 417–425, https://doi.org/10.1007/bf00370563.

Effect of the proximity to the 0°/90° interface on Energy Release Rate of fiber/matrix interface crack growth in the 90°-ply of a cross-ply laminate under tensile loading

Luca Di Stasio[1,2] ⓘ, Janis Varna[1] and Zoubir Ayadi[2]

Abstract

Models of Representative Volume Elements of cross-ply laminates with different geometric configurations and damage states are studied. Debond growth is characterized by the estimation of the Mode I and Mode II Energy Release Rate using the Virtual Crack Closure Technique. It is found that the presence of the 0°/90° interface and the thickness of the 0° layer has no effect, apart from laminates with *ultra-thin* 90° plies where it is however modest. The present analysis supports the claim that debond growth is not affected by the ply-thickness effect.

Introduction

Since the development of the *spread tow* technology or "FUKUI method",[1] significant efforts have been directed toward the characterization of *thin-ply* laminates[2–11] and their application to mission-critical structures in the aerospace sector.[12]

At the lamina level, the use of *thin-plies* leads to more regular and homogeneous microstructures.[6,9] Measurements of ply level properties (tensile and compressive modulus, Poisson's ratio, ultimate tensile strength, tensile onset of damage, and interlaminar shear strength) on uni-directional (UD) specimens ($[0_m^\circ]$ and $[90_m^\circ]$) revealed no remarkable difference with average properties available in the literature for the same type of fiber, nor showed any particular dependence on the ply thickness.[9] Only an increase of the ultimate compressive strength in the fiber direction was observed with very *thin-plies* (∼4 fiber diameters), although with very scattered values. The authors claim the increase to be due to the fiber arrangement's increased regularity which prevents the onset of fiber microbuckling.[9] A number of researchers[2–4] have reported improvements in fatigue life with the use of *thin-plies*, which are explained as a consequence of delayed propagation of free edge delaminations and intralaminar cracks. Several researchers have analyzed the effect of *thin-plies* on damage development under static,[3–9] fatigue,[2–5,9] and impact loadings.[3–5,9] It seems apparent that *thin-ply* laminates possess an increased ability to delay, and in some cases even suppress, the onset and propagation of intralaminar cracks (called often transverse or matrix or micro-cracks).

The first stage in the appearance of transverse cracks is known to be the occurrence of fiber/matrix interface cracks (also referred to as debonds), which grow along the fiber arc direction, then kink out of the interface and coalesce forming a transverse crack.[13] Different approaches have been applied to model the initiation and growth of debonds.[14] The Cohesive Zone Model (CZM) has been used to mimic the propagation of debonds along fiber interfaces; coupled with a failure

[1]Department of Engineering Sciences and Mathematics, Luleå University of Technology, Sweden
[2]IJL, EEIGM, Université de Lorraine, France

Corresponding author:
Luca Di Stasio, Luleå University of Technology, University Campus, SE-97187 Luleå, Sweden.
Email: luca.di.stasio@ltu.se

criterion for the matrix, it has provided simulations of the growth of transverse cracks starting from a virgin material.[15–18] The strength of the CZM, and its main requirement for a correct implementation, lies in the elimination of the stress and displacement singularity that exists at the crack tip in the Linear Elastic Fracture Mechanics (LEFM) solution, as the crack tip is not explicitly modeled and the failure process is "smeared" over the finite length of the cohesive element. The main advantages of this approach are the possibility to observe the development of a simulated crack path and to record a load–displacement curve to be compared with experimental measurements. The fracture toughness (or critical Energy Release Rate (ERR)) dependence on mode-mixity in the case of the interface crack[19] was successfully incorporated in a CZM by Freed and Banks-Sills.[20] However, different problems were reported[21] on the use of cohesive elements to simulate a bimaterial interface crack. It was observed that, for mixed-mode fracture in general, a single cohesive zone length might not simultaneously cancel both the tensile and shear stress singularity at the crack tip and thus fail to satisfy the fundamental requirement of the CZM approach. Also, it was concluded that energy dissipation at the cohesive zone tip could be neglected only with high enough values of the initial tensile and shear stiffness. A further issue which arises in the use of cohesive elements is the selection of appropriate values for the material parameters required by the model (critical stress and ERR). Two options are available: adopting values measured from macroscopic tests (e.g. Double Cantilever Beam) or calibrating the parameters through inverse estimation by approximation of the macroscopic stress–strain response of the specific specimen the Representative Volume Element (RVE) modeled is representing. Finally, the failure mechanisms proposed by the CZM might not represent the actual physics of the fiber/matrix interface failure process. It was shown[22] that the triaxiality of the matrix stress state in the inter-fiber region may be the driver of brittle matrix failure at or very close to the interface through a cavitation-like mechanism.[23] It thus seems likely that brittle failure at the interface may create an initial flaw from which debonding occurs in a fast and unstable manner, that could be modeled by the classic Griffith's criterion of LEFM. LEFM obviates many of the drawbacks highlighted for Cohesive Zone Modeling. The analysis focuses on the evaluation of Mode I and Mode II ERR at the crack tip by means of the Virtual Crack Closure Technique (VCCT)[24] or the J-Integral method.[25] The stress and strain fields, required for the ERR computation, can be solved by application of different methodologies such as

analytical solutions,[26] the Boundary Element Method (BEM),[27] or the Finite Element Method (FEM).[28] This approach presents nonetheless some limitations: it describes propagation of the debond and not its initiation; the role of friction in the contact zone is still an open issue; consensus is still lacking on a proper criterion for crack propagation in mixed mode. Finite fracture mechanics[29] is one way to address the initiation problem. Different studies have followed the LEFM approach and analyzed models of one or two fibers in an effectively infinite matrix[30–34] and of a hexagonal cluster of fibers in an effectively infinite homogenized UD composite.[28,35] The problem of debond growth along the fiber–matrix interface in a cross-ply laminate has been only treated very recently in Velasco et al.[36] and París et al.[37] where authors embed a single partially debonded fiber in an effectively infinite homogenized 90° ply bounded by homogenized 0° layers. Thus, the effect of debond–debond interaction and of the relative proximity of a 0°/90° interface on debond ERR in cross-ply laminates is yet to be addressed. The present work is devoted to this problem. In particular, we propose a LEFM assessment of the effect of micro- and macro-structural features (undamaged fibers, multiple debonds, 0°/90° ply interface, 0° ply thickness, and 90° ply thickness) on debond growth in cross-ply laminates. CZM-based works[15–18] have addressed the effect of macroscopic features such as the thickness of the 0° and of the 90° ply, while microscopical effects such as the presence of neighboring fully bonded fibers or of other debonds where neglected due to the choice of adopting random distribution of fibers. Previous LEFM studies[28,30–37] focused on both macroscopical (e.g. ply thickness) and microscopical (e.g. neighboring fibers and debonds), but with a very limited number of fibers (usually two or six) embedded either in an infinite matrix or in homogenized material. Our interest however is not to investigate the sequence of failure events, which would require knowledge of appropriate failure criteria and properties, but rather to understand which parameters may make debond growth energetically favorable and which may prevent it. Models of Repeating Unit Cells (RUCs) are developed to represent laminates with different degrees of damage in the 90° ply (here only in the form of debonds). The number of fully bonded fibers across the thickness of the 90° ply is varied in order to investigate the effect of the proximity of the 0°/90° interface. The thickness of the bounding 0° layers is also used as a parameter of the study. The stress and strain fields are solved with the FEM in Abaqus[38] and the debond (crack) is characterized by its Mode I and Mode II ERR calculated with the VCCT.

RVE models and Finite Element discretization

Introduction and nomenclature

In the present work, we investigate debond development under in-plane longitudinal tension in $\left[0^{\circ}_{m \cdot k \cdot 2L}, 90^{\circ}_{k \cdot 2L}, 0^{\circ}_{m \cdot k \cdot 2L}\right]$ laminates. The interaction between debonds in the presence of an interface with a stiff layer is studied with the use of different RUCs (see Figures 1 and 2), in which only the central fiber is partially debonded. Repetition of the composite RUC occurs along the in-plane laminate 0°-direction (corresponding to specimen axial direction and RUC horizontal direction in Figures 1 and 2), thus representing a cross-ply laminate with a thin or even *ultra-thin* 90° ply in the middle.

All the RUCs present regular microstructures with fibers placed according to a square-packing configuration characterized by the repetition of the same one-fiber unit cell of size $2L \times 2L$, where L is a function of the fiber volume fraction V_f and the fiber radius according to

$$L = \frac{R_f}{2}\sqrt{\frac{\pi}{V_f}} \qquad (1)$$

The choice of a square-packing configuration with a controlled number of fibers is motivated by the fact that our objective is to determine the effect of different geometrical and mechanical factors on debond ERR, such as fiber volume fraction, the presence of undamaged and partially debonded fibers, and the presence of the $0^{\circ}/90^{\circ}$ interface. The use of a regular microstructure allows us to isolate and identify the different contributions, which would be otherwise "smeared out" with the use of randomized distribution with a large number of fibers. Each fiber in the model has the

same radius R_f, equal to 1 µm. This specific value has no physical meaning per se and it has been selected for simplicity. It is useful to observe that, in a linear elastic solution subject to non-holonomic constraints as the one described in the present article, the ERR is proportional to the geometrical dimensions of the model and thus re-evaluation of the ERR for fibers of any size requires just a multiplication. Given that in the present paper we compare trends between models having always $R_f = 1$ µm, the conclusions proposed remain
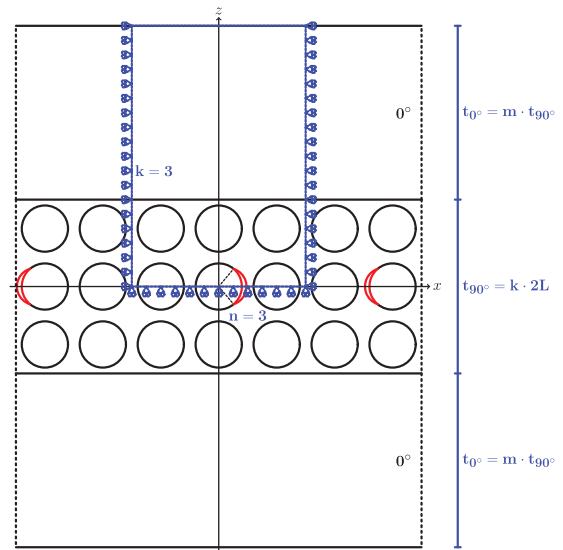
Figure 2. Models of $\left[0^{\circ}_{m \cdot k \cdot 2L}, 90^{\circ}_{k \cdot 2L}, 0^{\circ}_{m \cdot k \cdot 2L}\right]$ laminates with a 90° layer of variable thickness, determined by the number k of "rows" of fibers along the vertical direction. Debonds are repeating at different distances along the horizontal direction, measured in terms of the number $n - 1$ of fully bonded fibers appearing between two consecutive debonds. $2L$ is the thickness of one-fiber row.
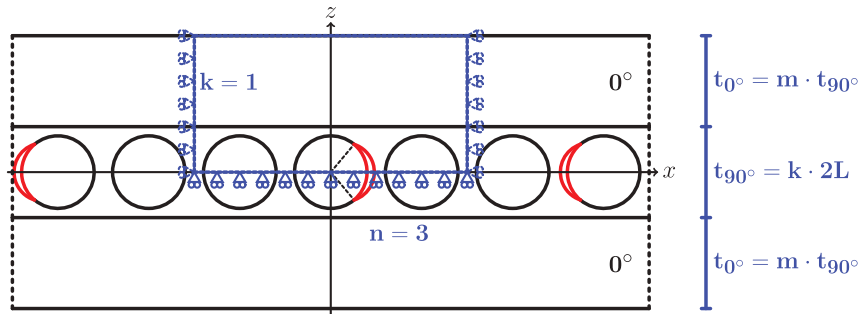
Figure 1. Models of $\left[0^{\circ}_{m \cdot 1 \cdot 2L}, 90^{\circ}_{1 \cdot 2L}, 0^{\circ}_{m \cdot 1 \cdot 2L}\right]$ laminates with an *ultra-thin* 90° layer, where the 90° ply is made up by a single "row" of fibers. Debonds are repeating at different distances, measured in terms of the number $n - 1$ of fully bonded fibers appearing between two consecutive debonds. $2L$ is the thickness of one-fiber row.

valid for different values of R_f as all the results would scale, in the context of LEFM, in the same way. Furthermore, it is worth to point out that V_f is the same in the one-fiber unit and in the overall RUC, i.e. no clustering of fibers is considered.

The thickness of the 90° ply depends on the number k of fiber rows present across the thickness (the vertical or z direction in Figures 1 and 2) according to

$$t_{90°} = k \cdot 2L \qquad (2)$$

On the other hand, the thickness of 0° layers can be assigned freely as a multiple of the 90° ply thickness as

$$t_{0°} = m \cdot t_{90°} \qquad (3)$$

where m is an arbitrary integer. Thus, the thickness ratio m represents one additional parameter for the investigation.

In the following, let us consider in-plane coordinates x and y, and assume that the laminate 0°-direction is aligned with the x-axis. In the presence of a load in the x-direction, the strain in the y-direction is small, due to the very small Poisson's ratio of the laminate. Debonds are present only in the 90° layer and are considered to be significantly longer in the fiber direction than in the arc direction.[39] Therefore, we use 2D models under the assumption of plane strain, defined in the x–z section of the composite. The study presented in this paper thus applies to long debonds and its focus is on understanding the mechanisms of growth along their arc direction. The laminates are assumed to be subjected to tensile strain, which is applied in the form of a constant displacement in the x-direction along both vertical boundaries of the RUC as shown in Figure 3.

We assume damage to be present only in the central "row" of fibers of the 90° layer in the form of multiple debonds appearing at different regular intervals along

the loading (horizontal) direction. The number of fibers n present in the horizontal direction of the RUC (Figures 1 and 2) controls the distance, in terms of fully bonded fibers, between consecutive debonds: if the RUC has n fibers in the horizontal direction, two consecutive debonds are separated by $n - 1$ undamaged fibers. We thus study distributions of multiple debonds aligned in the horizontal (loading) direction. The choice is motivated by our interest in understanding the mutual interaction between debonds in the loading direction, namely "crack shielding". As debonds represent nucleation sites for transverse cracks, analysis of debond interaction in the loading direction would help understanding if and under which conditions transverse cracks can initiate. Furthermore, recent experimental studies of extremely *thin-ply* laminates[6] show the suppression of transverse cracks but the occurrence of debonds in the 90° ply. Thus, although microscopical observations are still few, it seems possible that distributions of debonds along the horizontal (loading) direction might occur in this class of engineered materials. The RUCs considered are thus RVEs of cross-ply laminates with a certain distribution of debonds in the middle 90° layer.

In summary, the models are differentiated by: first, the spacing between debonds along the horizontal direction in the 90° layer, which corresponds to the number n of fibers in the RUC's horizontal direction; second, the thickness of the middle 90° ply measured in terms of the number k of fiber rows in the vertical direction; and third, the factor m which provides the thickness of 0° layers as a multiple of the 90° ply thickness. It thus seems natural to introduce a common notation for the RUCs as $n \times k - m \cdot t_{90°}$.

An additional family of RUCs is considered, in which: only one partially debonded fiber is present; the 0° layer is absent; different combinations of displacement boundary conditions are applied to the upper surface. The application of coupling of horizontal displacements u_x along the right and left sides allows for repetition along the horizontal direction. Noticing that the right and left sides are located respectively at $x = +nL$ and $x = -nL$, conditions of coupling of the horizontal displacements along the right and left sides imply that

$$u_x(\pm nL, z) = \pm \bar{\varepsilon}_x nL \qquad (4)$$

where $\bar{\varepsilon}_x$ is the value of the global applied strain. When the upper boundary of the RUC is left free, we define the $1 \times 1 - free$ model. If coupling of the vertical displacements u_z is applied to the upper boundary (coupling condition), we define instead the $1 \times 1 - coupling$ model. Observing that the upper boundary of the RUC is located at $z = kL$, conditions of coupling of the
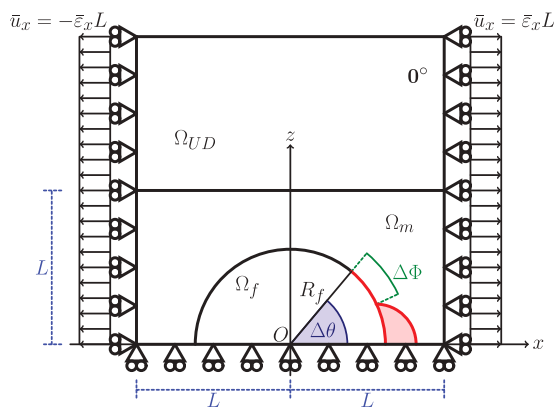

Figure 3. Schematic of the model with its main parameters.

vertical displacements along the upper boundary imply that

$$u_z(x, kL) = u_z^v \qquad (5)$$

where u_z^v is a value of the vertical displacement independent of x due to Poisson's effect and determined as part of the elastic solution. In other words, the conditions of coupling of the vertical displacements $u_z(x, kL)$ of equation (7) mean that the upper boundary remains straight during deformation but it is allowed to move along the vertical direction by u_z^v while remaining straight. In this case, a linear distribution of the horizontal displacement u_x is applied to the upper boundary (H-condition), as

$$u_x(x, kL) = \bar{\varepsilon}_x x \qquad (6)$$

where $\bar{\varepsilon}_x$ is the value of the global applied strain, the model is referred to as $1 \times 1 - H$. The presence of a linearly distributed horizontal displacement along the upper boundary is meant to represent, as an extreme case, the presence of stiffer material, i.e. the $0°$ layer, which forces a more homogeneous displacement distribution at the interface. Finally, when the linear distribution of the horizontal displacement u_x is superimposed to the condition of coupling of the vertical displacements u_z on the upper boundary, i.e. the following set of equations holds at the upper boundary

$$\begin{aligned} u_z(x, kL) &= u_z^v \\ u_x(x, kL) &= \bar{\varepsilon}_x x \end{aligned} \qquad (7)$$

we have the $1 \times 1 - coupling + H$. Further details about this family of RUCs and the corresponding laminate RVE can be found in Di Stasio et al.[40]

Description of modeled RVEs

The first family of RVEs is represented in Figure 1. It represents a set of $[0°_{m \cdot 1 \cdot 2L}, 90°_{1 \cdot 2L}, 0°_{m \cdot 1 \cdot 2L}]$ laminates with an *ultra-thin* $90°$ layer, constituted by a single row of fibers across the thickness. Debonds appear at regular intervals measured in terms of number $n - 1$ of fully bonded fibers present between them, which in turn correspond to the number of fibers along the horizontal direction of the RVE as highlighted in Figure 1. They are thus the $n \times 1 - m \cdot t_{90°}$ models, where $m = 1, 10$ and n is an integer ≥ 1 ($n = 1$ corresponds to the case of a debond appearing on all the fibers in the central $90°$ layer). These models are geometrically extreme, but allow to focus on the interaction between debonds and the inter-ply $0°/90°$ interface. Furthermore, the *spread tow* technology is today capable of producing cross-ply laminates with the central $90°$ layer thickness only $4 - 5$

times the fiber diameter, as shown, for example, in Saito et al.,[6] which may in future give practical relevance even to such extreme case.

The second set of models considers instead cross-ply laminates with a central $90°$ ply of variable thickness, measured in terms of number k of fiber rows "stacked" in the vertical direction in Figure 2. Once again, debonds appear in the central row only at regular intervals measured in terms of number $n - 1$ of fully bonded fibers present between them, as highlighted in Figure 2. These models are thus the $n \times k - m \cdot t_{90°}$ models, where $m = 1, 10, k > 1$, and n is an integer ≥ 1. Notice that $n = 1$ corresponds to the case of a debond appearing on all fibers of the central fiber row in the $90°$ layer, which represents an extreme idealization and corresponds to the state of maximum damage in the RVEs considered, in other words, it would provide the minimum ERR available at the debond tip. This, in turn, makes it a very good candidate to study the effect of the presence of the $0°/90°$ interface and of the thickness of the $0°$ ply. By increasing the number n of fibers in the horizontal direction in the RUC, decreasing levels of damage (debonds spaced further apart and the interaction between debonds becomes less important) are considered to be present in the laminate. By increasing the number k of fiber rows, the thickness of the $90°$ layer is increased and the effect of the relative proximity of the inter-ply $0°/90°$ interface can thus be studied. Finally, by increasing the factor m, the thickness of the $0°$ layers is increased for a given thickness of the $90°$, which allows the investigation of the $0°$ ply-block effect.[41]

Finite Element discretization

The RUCs are discretized and solved with the FEM using the commercial FEM package, Abaqus.[38] The total length and height of a RUC are determined by the number of fibers n in the horizontal direction, the number of fiber rows k across the thickness, and the thickness ratio m (see Section "Introduction and nomenclature" and Section "Description of modeled RVEs"). The debond appears symmetrically with respect to the x-axis (see Figure 3) and we characterize it with the angular size $\Delta\theta$ (the full debond size is thus $2\Delta\theta$). In the case of large debond sizes ($\geq 60° - 80°$), a region of size $\Delta\Phi$ to be determined by the solution itself appears at the crack tip. In this region, called the *contact zone*, the crack faces are in contact and slide on each other. Due to existence of the contact zone, frictionless contact is considered between the two crack faces to avoid interpenetration and allow free sliding. Symmetry with respect to the x-axis is applied on the lower boundary. Kinematic coupling on the x-displacement is applied along the left and right boundaries of

the model in the form of a constant x-displacement $\pm\bar{\varepsilon}_x nL$, corresponding to laminate x-strain $\bar{\varepsilon}_x$ equal to 1%. The bimaterial interface crack problem belongs to the class of *receding contact*,[27,42] i.e. such that the contact zone in the final configuration is smaller than in the initial one. It was shown that this class of problems has some peculiar properties,[43,44] which are valid both with and without friction at the interface[27,42]: size and shape of the contact zone remain the same upon a change in the magnitude of the applied load; only a change in the disposition of the applied load causes a change in the size and shape of the contact zone; displacements, stresses, and strains (and consequently, ERR) are directly proportional to the value of the applied load. Thus, although our interest is to compare the relative magnitude of Mode I and Mode II ERR among different configurations, the results presented could be used to compute the ERR at different levels of the applied strain through a simple multiplication.

The FEM model is discretized using second-order, 2D, plane strain triangular (CPE6) and rectangular (CPE8) elements. In the crack tip neighborhood, a refined regular mesh of quadrilateral elements with almost unitary aspect ratio is needed to ensure a correct evaluation of the ERR. The angular size δ of an element in this refined region close to the crack tip is by design equal to $0.05°$. The crack faces are modeled as element-based surfaces with a frictionless small-sliding contact pair interaction. The Mode I, Mode II, and total ERRs (respectively G_I, G_{II}, and G_{TOT}) represent the main result of the numerical analysis. They are computed using the VCCT[24] implemented in a Python routine developed by one of the authors. Glass fiber and epoxy are considered throughout this article, and it is assumed that their response always lies in the linear elastic domain. The effective UD properties are computed using Hashin's Concentric Cylinder Assembly model[45] with the self-consistency scheme for the out-of-plane shear modulus of Christensen and Lo.[46] The properties used are listed in Table 1. The model was validated with respect to BEM results of Sandino et al.[33] and París et al.;[47] considerations about the order of accuracy can be found in Di Stasio et al.[40]

Table 1. Summary of mechanical properties of fiber, matrix, and UD layer.

|	$V_f[\%]$	$E_L[GPa]$	$E_T[GPa]$	$G_{LT}[GPa]$	$\nu_{LT}[-]$	$\nu_{TT}[-]$
GF	–	70.0	70.0	29.2	0.2	0.2
EP	–	3.5	3.5	1.25	0.4	0.4
UD	60.0	43.442	13.714	4.315	0.273	0.465

GF: glass fiber; EP: epoxy; UD: glass–fiber/epoxy uni-directional properties.

Results and discussion

Effect of the proximity of the 0°/90° interface and of the thickness of the 0° layer on debond ERR for highly interactive debonds

We first focus our attention on the model $1 \times 1 - m \cdot t_{90°}$, which represents a particular case of the family $n \times 1 - m \cdot t_{90°}$. It corresponds to a cross-ply laminate in which the central 90° ply is constituted by only one fiber row, in which each fiber possesses a debond appearing on alternating sides. The model thus represents an extreme idealization, in the sense that: first, the central 90° layer is the thinnest that can be conceived, which allows us to investigate the direct effect of the proximity of the 0°/90° interface on debond ERR; second, a very particular damage state is present for which every fiber is partially debonded from the surrounding matrix, corresponding to the most severe damage state that can occur in the 90° ply when considering debonds as the only mechanism of damage. We are thus focusing on the presence of the 0°/90° interface and on the thickness of the 0° layer, by considering the ratio $m = \frac{t_{0°}}{t_{90°}}$ of ply thicknesses as a free parameter.

In Figures 4 and 5, it is possible to observe respectively the Mode I and Mode II ERR for models $1 \times 1 - m \cdot t_{90°}$ with $m = 1$, 10, and 100. Mode I ERR is practically unaffected by the 0° layer thickness, only a marginal increase ($\leq 1\%$) can be seen when m is increased from 1 to 10. No further observable change is present when m is increased to 100. Moreover, the contact zone onset, which corresponds to the first value of $\Delta\theta$ such that $G_I = 0$, is always equal to 70° irrespective of the value of m. A more remarkable, although
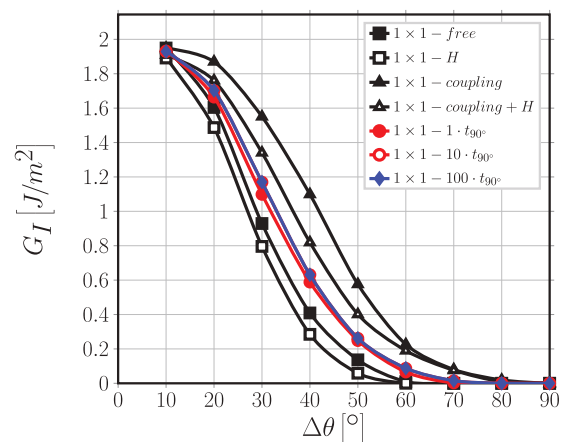
Figure 4. Effect of the proximity of the 0°/90° interface and of the thickness of the 0° layer on Mode I ERR: models $1 \times 1 - free$, $1 \times 1 - H$, $1 \times 1 - coupling$, $1 \times 1 - coupling + H$, and $1 \times 1 - m \cdot t_{90°}$. $V_f = 60\%$, $\bar{\varepsilon}_x = 1\%$.
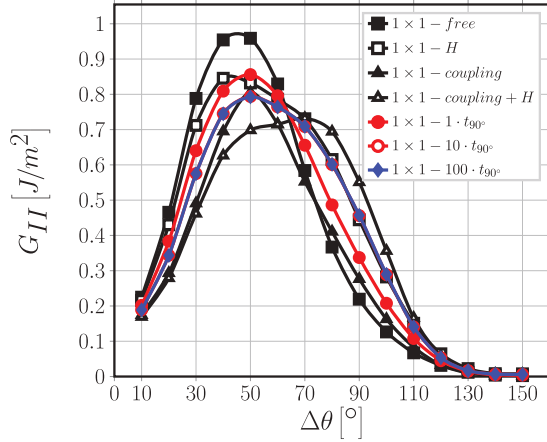
Figure 5. Effect of the proximity of the $0°/90°$ interface and of the thickness of the $0°$ layer on Mode II ERR: models $1 \times 1 - free$, $1 \times 1 - H$, $1 \times 1 - coupling$, $1 \times 1 - coupling + H$, and $1 \times 1 - m \cdot t_{90°}$. $V_f = 60\%$, $\bar{\varepsilon}_x = 1\%$.

small, effect of the $0°$ layer thickness can be observed for Mode II when m is increased from 1 to values ≥ 10. For open cracks, i.e. when no contact zone is present and thus $\Delta\theta$ is smaller than $70°$, increasing the $0°$ layer thickness causes a reduction of Mode II ERR; while for closed cracks, when a contact zone is present and $\Delta\theta > 70°$, the increase in thickness leads to an increase in ERR.

In order to understand the interaction mechanism between the $0°/90°$ interface and the debond, Mode I and Mode II ERR are reported respectively in Figures 4 and 5 for models $1 \times 1 - free$, $1 \times 1 - H$, $1 \times 1 - coupling$, and $1 \times 1 - coupling + H$. These RUCs all present equivalent boundary conditions and it is here useful to recall their characteristics: in model $1 \times 1 - free$, the upper boundary is left free; coupling conditions on the vertical displacements u_z are applied to the upper boundary in model $1 \times 1 - coupling$ (coupling condition); in model $1 \times 1 - H$, a linearly distributed horizontal displacement u_x is applied to the upper boundary (H-condition); in model $1 \times 1 - coupling + H$ coupling conditions on the vertical displacements u_z and a linearly distributed horizontal displacement u_x are imposed together on the upper boundary. Given that the presence of a $0°$ layer provides two constraints: first, it tends to keep the $90°$ layer boundary straight; second, it forces a more homogeneous horizontal displacement at the $90°$ layer boundary; the equivalent boundary conditions of $1 \times 1 - coupling$, $1 \times 1 - H$ and $1 \times 1 - coupling + H$ represent an extreme case respectively of the first constraint ($1 \times 1 - coupling$), the second constraint ($1 \times 1 - H$), and the two together ($1 \times 1 - coupling + H$). The case $1 \times 1 - free$ constitutes instead the base case (absence of $0°$ layer), on which comparisons are built.

Observing Figure 4, it is possible to notice that the values of G_I for the $1 \times 1 - free$ and the $1 \times 1 - coupling$ models represent respectively a lower and an upper bound for the $1 \times 1 - m \cdot t_{90°}$ RVEs: this is true with respect to the value of G_I as well as of contact zone onset ($60°$ for $1 \times 1 - free$, $70°$ for $1 \times 1 - m \cdot t_{90°}$, $80°$ for $1 \times 1 - coupling$). Notice that in the case of $1 \times 1 - coupling$, the upper surface moves by an amount of u_z^v in the vertical direction, due to Poisson's effect, while remaining straight (see equation (7)). The value of u_z^v is evaluated as part of the elastic solution and it results to be always negative. This agrees well with the expectation that, upon application of a tensile load in the x-direction, Poisson's effect causes a contraction of the cross-section normal to the x-axis, which translates into a negative z-displacement in the x–z plane. The contraction is greater in the matrix than in fibers, due to the fact that $v_m > v_f$.[48] This in turn means that the fiber–matrix interface is subjected to a compressive stress state for $\Delta\theta > 80° - 90°$, preventing debond growth in Mode I and corresponding in Figure 4 to the fact that $G_I = 0$ for $\Delta\theta \geq 80°$. When the H-condition is added to the $1 \times 1 - free$ and the $1 \times 1 - coupling$ models, thus obtaining the $1 \times 1 - H$ and $1 \times 1 - coupling + H$ models, G_I decreases while the value of $\Delta\theta$ at contact zone onset remains unchanged ($60°$ for $1 \times 1 - free$ and $1 \times 1 - H$, $80°$ for $1 \times 1 - coupling$ and $1 \times 1 - coupling + H$). Moreover, it is possible to observe that the values of G_I of $1 \times 1 - coupling + H$ are much closer to but always greater than those of $1 \times 1 - m \cdot t_{90°}$ RVEs, thus constituting a more representative upper bound for the latter.

Analogous considerations are drawn with regard to Mode II (see Figure 5). For small debonds, $\Delta\theta \leq 30°$, no significant difference in G_{II} can be seen between $1 \times 1 - free$ and $1 \times 1 - H$ and between $1 \times 1 - coupling$ and $1 \times 1 - coupling + H$ in this region. With respect to $1 \times 1 - m \cdot t_{90°}$ RVEs, the first pair ($1 \times 1 - free$ and $1 \times 1 - H$) represents the lower bound while the second pair ($1 \times 1 - coupling$ and $1 \times 1 - coupling + H$) the upper bound. For $30° < \Delta\theta \leq 60°$, $1 \times 1 - H$ and $1 \times 1 - coupling + H$ provide significantly lower values of G_{II} than respectively $1 \times 1 - free$ and $1 \times 1 - coupling$. G_{II} values of $1 \times 1 - H$ are very close to $1 \times 1 - 1 \cdot t_{90°}$, even coincident for $\Delta\theta = 60°$. On the other hand, G_{II} values of $1 \times 1 - coupling$ are very close to $1 \times 1 - m \cdot t_{90°}$ with $m \geq 10$ and even coincident for $\Delta\theta = 50°$. For $60° < \Delta\theta \leq 110°$, the situation changes. $1 \times 1 - free$ and $1 \times 1 - coupling$ provides values of G_{II} close to each other, even coincident for $\Delta\theta = 70°$. Values of G_{II} of $1 \times 1 - H$ and $1 \times 1 - coupling + H$ are significantly larger than both $1 \times 1 - free$ and $1 \times 1 - coupling$. Furthermore, G_{II} values of $1 \times 1 - H$ coincide

with those of $1 \times 1 - m \cdot t_{90°}$ with $m \geq 10$. Mode II ERR of $1 \times 1 - 1 \cdot t_{90°}$ is instead close, but not coincident, to that of $1 \times 1 - coupling$. For $\Delta\theta > 110°$, G_{II} is the same for all models and reaches 0 at a debond size of around $130°$.

These results help to understand the effect of the $0°/90°$ interface on debond ERR. Two constraining mechanisms are present in the case of $0°/90°$ interface that are absent in the free surface case: first, the boundary of the $90°$ layer remains straighter (effect modeled by the coupling condition in $1 \times 1 - coupling$); second, the x-strain on the $90°$ layer boundary is more uniform (effect modeled by the H-condition in $1 \times 1 - H$).

For small debonds ($\Delta\theta < 60° - 70°$), the presence of the $0°/90°$ interface causes an increase of G_I and a decrease of G_{II} with respect to the free surface case. For Mode I, the fact that the $90°$ layer boundary remains straight (coupling condition) forces the debond to open more than in the free case, thus increasing G_I. However, the uniformity of the x-strain on the $90°$ layer boundary reduces the local (in the debond neighborhood) x-strain magnification and contains the increase in G_I. This corresponds in Figure 4 to the fact that Mode I ERR for $1 \times 1 - m \cdot t_{90°}$ is always higher than $1 \times 1 - free$ but lower than $1 \times 1 - coupling$, and it is best approximated by $1 \times 1 - coupling + H$. For Mode II in the case of small debonds, the presence of the $0°$ layer keeps the $0°/90°$ interface straighter and reduces the vertical contraction of the matrix, which contributes for the most part to Mode II in this range, thus leading to a decrease of G_{II}. The small effect of $0°$ layer thickness on Mode II (Figure 5) can be explained in terms of local bending stiffness: a thinner $0°$ layer ($\frac{t_{0°}}{t_{90°}} = 1$) does not keep the $90°$ layer boundary as straight as thicker $0°$ layers ($\frac{t_{0°}}{t_{90°}} \geq 10$). In the case $\frac{t_{0°}}{t_{90°}} = 1$, the $90°$ layer boundary deforms in a way that is similar to the free surface case, but smaller in magnitude. This corresponds to the fact that for $\Delta\theta < 60° - 70°$, in Figure 5: $1 \times 1 - 1 \cdot t_{90°}$ is best approximated by $1 \times 1 - H$ (curved $90°$ layer boundary but uniform x-strain at the $90°$ layer boundary that disfavors G_{II}), $1 \times 1 - m \cdot t_{90°}, m \geq 10$ is best approximated by $1 \times 1 - coupling$ (straight $90°$ layer boundary).

For debonds larger than $70°$, the presence of the $0°/90°$ interface causes an increase of G_{II} with respect to the free surface case. The uniform x-strain distribution on the $90°$ layer boundary determined by the presence of the $0°$ layer causes, with respect to the free case, the matrix x-strain to be higher in the $x\sim0$ neighborhood and lower around $x \sim \pm L$, in order to keep the average ε_x at 1%. Given that for large debonds, Mode II ERR is determined mostly by the magnitude of the x-strain gap (between the matrix x-strain and the fiber x-strain), an increase of G_{II} is thus observed in the

presence of the $0°/90°$ interface. Again, the observed effect of the $0°$ layer thickness on Mode II for $\Delta\theta > 60° - 70°$ (Figure 5) can be discussed in terms of local $0°$ layer bending stiffness. In the free case, it is the curvature of the material around the fiber that causes the x-strain reduction and thus a lower G_{II}. Thicker $0°$ layers ($\frac{t_{0°}}{t_{90°}} \geq 10$) prevent this $90°$ boundary deformation to a greater extent than the thinner $t_{0°} = t_{90°}$ case: the x-strain (and thus G_{II}) increase is greater for $\frac{t_{0°}}{t_{90°}} \geq 10$ than $\frac{t_{0°}}{t_{90°}} = 1$.

Effect of the proximity of the $0°/90°$ interface and of the thickness of the $0°$ layer on non-interactive debonds in a one-fiber row $90°$ ply

We turn now our attention to models $n \times 1 - m \cdot t_{90°}$, which correspond to a cross-ply laminate in which the central $90°$ ply is constituted by only one fiber row where multiple partially debonded fibers are present with $n - 1$ fully bonded fibers between them and debonds appear on alternating sides of consecutive damaged fibers (see Figure 1). As observed in a previous work,[40] the presence of fully bonded fibers between partially debonded ones in the loading direction has a strong effect on debond ERR and controls the interaction between debonds. When n is increased, both Mode I and Mode II increase: the addition of stiffer elements, in the form of fully bonded fibers, increase the strain applied to the damaged unit and thus causes higher values of ERR. Looked from this perspective, i.e. moving from the most to the least severe state of damage, this effect is referred to as "strain magnification".[40] Notice also that the addition of stiffer elements causes a higher global stress at the boundary, i.e. the laminate corresponding to $21 \times 1 - m \cdot t_{90°}$ is stiffer than the laminate modeled by $1 \times 1 - m \cdot t_{90°}$. In the present work, comparisons are drawn at the same level of applied strain, as in practical applications, the interest lies often in understanding the material response to a prescribed strain. Furthermore, this choice adheres with the modeling approach of Classical Laminate Theory and, in the context of damage-induced degradation of elastic properties, with the GLOB-LOC modeling strategy developed for transverse cracks.[49] There seems to exist a characteristic distance, measured in terms of fully bonded fibers, above which a change in the number of undamaged fibers affects only marginally, or even not at all, debond ERR. This distance, generally $n\sim20$, marks the transition between a non-interactive solution ($n > 20$) and an interactive one ($n < 20$). The "strain magnification" effect thus represents the transition from the interactive to the non-interactive solution. If in Section "Effect of the proximity of the $0°/90°$ interface and of the thickness of the $0°$ layer on debond

ERR for highly interactive debonds" we studied the effect of the proximity of the 0°/90° interface and of the thickness of the 0° layer on interactive debonds $(1 \times 1 - \ldots)$, we analyze in the present section the effect of the 0°/90° interface and of the 0° layer thickness on non-interactive ones $(n \times 1 - \ldots$ with n > 20).

Comparing Figure 6 with Figure 4 and Figure 7 with Figure 5, it is possible to observe how, as previously described, increasing the number of fully bonded fibers between consecutive debonds in the loading direction leads to an increase in Mode I and Mode II ERR. The peak G_I increases from $1.93\left[\frac{J}{m^2}\right]$ in $1 \times 1 - 1 \cdot t_{90°}$ to $3.42\left[\frac{J}{m^2}\right]$ in $21 \times 1 - 1 \cdot t_{90°}$, while the peak G_{II} from $0.86\left[\frac{J}{m^2}\right]$ to $3.04\left[\frac{J}{m^2}\right]$. The value of $\Delta\theta$ at contact zone onset remains however the same (70°).

The effect of the 0° layer thickness is instead non-existent: values of both G_I and G_{II} are coincident for $21 \times 1 - 1 \cdot t_{90°}$ and $21 \times 1 - 10 \cdot t_{90°}$.

In agreement with the introductory considerations of this section and the results in Di Stasio et al.,[40] it is possible to observe in Figures 6 and 7 that $21 \times 1 - free$ and $21 \times 1 - coupling$ (in which the horizontal displacement u_x is left unconstrained on the upper boundary) show both the highest values of Mode I and Mode II ERR as well as the maximum increase with respect to the interactive case ($1 \times 1 - free$ and $1 \times 1 - coupling$). When the H-condition is applied to the upper boundary, thus constraining the magnitude of the strain magnification effect, both the magnitude of Mode I and Mode II ERR as well as their relative increase with respect to the interactive case are significantly reduced; $21 \times 1 - coupling + H$ represents, when considering both Mode I and Mode II ERR, the best
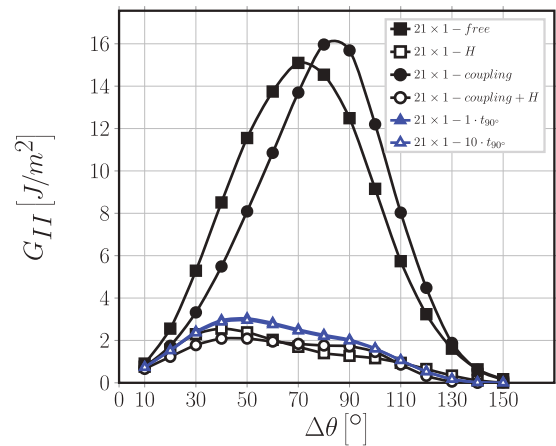
approximation to the results of $21 \times 1 - m \cdot t_{90°}$. The mechanisms at play are the same as in Section "Effect of the proximity of the 0°/90° interface and of the thickness of the 0° layer on debond ERR for highly interactive debonds": by keeping the 0°/90° interface straight (coupling condition), the 0° layer favors an increase in G_I and decrease in G_{II} for small debonds and an increase in G_{II} for large debonds; by applying a uniform x-strain on the 90° layer boundary (H-condition), the 0° layer promotes a more uniform x-strain in the 90° layer and acts against the strain magnification effect, reducing debond ERR. Results in Figures 6 and 7 show that the latter effect (H-condition) is dominant. It seems reasonable to conclude that debond growth is favored (i.e. debond ERR is higher) in the presence of strain or stress concentrations (as, for example, in the presence of a free surface or only coupling conditions on the vertical displacement), while more uniform strain and stress fields as those created by the proximity of the 0°/90° interface reduce both Mode I and Mode II ERR and thus tend to prevent debond growth.

Effect of the presence of fiber rows with no damage on the debond-0°/90° interface interaction

After having investigated the effect of the proximity of the 0°/90° interface and of the thickness of the 0° layer on debond ERR for different cases of debond–debond interaction in the same fiber row, we address in this section the effect of the presence of fiber rows with only fully bonded fibers between debonds and the 0°/90° interface. In other words, we are separating the debond from the 0°/90° interface by inserting
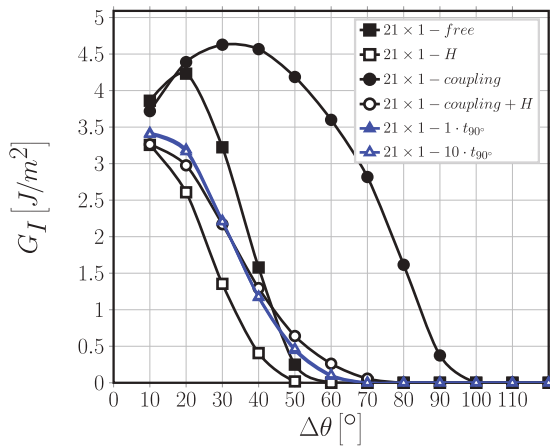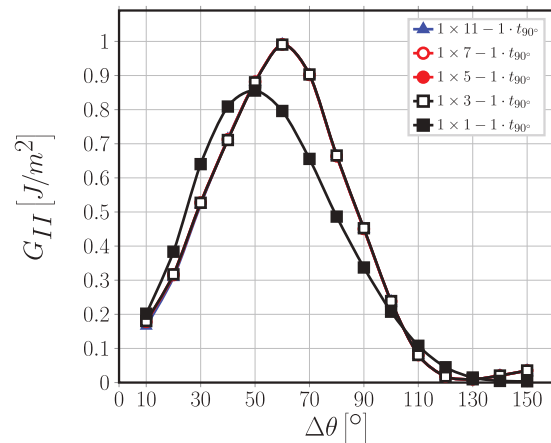

Figure 6. Effect of the presence of the 0° layer on Mode I ERR of non-interactive debonds: models $21 \times 1 - free$, $21 \times 1 - H$, $21 \times 1 - coupling$, $21 \times 1 - coupling + H$, $21 \times 1 - 1 \cdot t_{90°}$, and $21 \times 1 - 10 \cdot t_{90°}$. $V_f = 60\%$, $\bar{\varepsilon}_x = 1\%$.

Figure 7. Effect of the presence of the 0° layer on Mode II ERR of non-interactive debonds: models $21 \times 1 - free$, $21 \times 1 - H$, $21 \times 1 - coupling$, $21 \times 1 - coupling + H$, $21 \times 1 - 1 \cdot t_{90°}$, and $21 \times 1 - 10 \cdot t_{90°}$. $V_f = 60\%$, $\bar{\varepsilon}_x = 1\%$.

rows of fully bonded fibers in between. We consider only the case $m = 1$, i.e. $t_{0°} = t_{90°}$, given that increasing the 0° layer thickness does not result in any remarkable effect on ERR as shown in Section "Effect of the proximity of the 0°/90° interface and of the thickness of the 0° layer on debond ERR for highly interactive debonds" and Section "Effect of the proximity of the 0°/90° interface and of the thickness of the 0° layer on non-interactive debonds in a one-fiber row 90° ply". Following the same philosophy of these two previous Sections, we analyze the effect of the presence of fiber rows with no damage on debond ERR: first, when the central fiber row possesses only partially debonded fibers, which represents the most severe damage state for these RUCs and the solution for interactive debonds (models $1 \times k - 1 \cdot t_{90°}$ in Figures 8 and 9); second, the case of debonds separated by $n - 1$ fully bonded fibers in the central fiber row, which corresponds to the least severe state of damage and to the solution for non-interactive debonds (models $21 \times k - 1 \cdot t_{90°}$ in Figures 10 and 11).

Observation of Figures 8–11 reveals that no difference can be seen in Mode I and Mode II ERR by increasing the number k of rows with undamaged fibers when $k \geq 3$, which means that debond ERR does not change once, at least one row of undamaged fibers is present between the debond and the 0°/90° interface. A significant change is visible only when $k = 1$, which means that no row of undamaged fibers is present between the debond and the 0°/90° interface. This change, from $k \geq 3$ to $k = 1$, corresponds in particular to a reduction of both G_I and G_{II}.

The results of Figures 8–11 imply that the mechanisms of debond–0°/90° interface interaction described in Sections "Effect of the proximity of the 0°/90°

interface and of the thickness of the 0° layer on debond ERR for highly interactive debonds" and "Effect of the proximity of the 0°/90° interface and of the thickness of the 0° layer on non-interactive debonds in a one-fiber row 90° ply" are actually very localized and that debond ERR is affected by the presence of the 0°/90° interface only when no fully bonded fiber is placed in between. Given that the number k of fibers in the RUC vertical direction corresponds to the thickness of the 90° ply measured in terms of number of fiber rows present through its thickness, the results presented here point to another conclusion: the ply-thickness effect does not seem to apply to debond growth, unless an *ultra-thin* ply constituted by only one fiber row ($k = 1$) is considered.
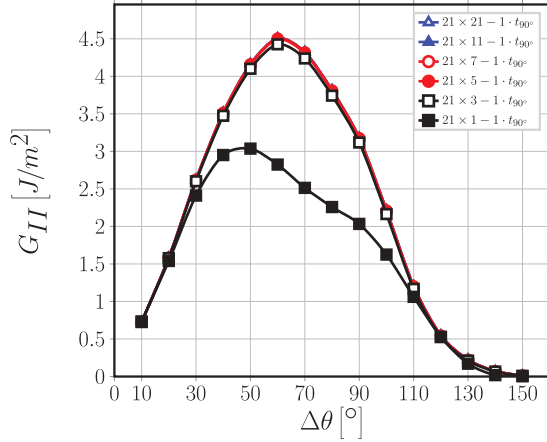

Figure 9. Effect of the presence of undamaged fiber rows in the 90° layer on debond-0°/90° interface interaction for Mode II ERR: models $1 \times k - 1 \cdot t_{90°}$. $V_f = 60\%$, $\bar{\varepsilon}_x = 1\%$.
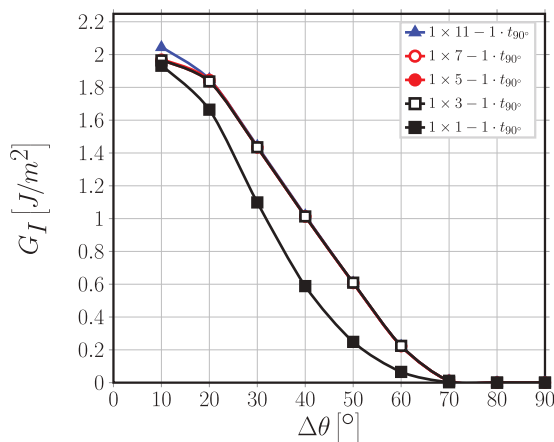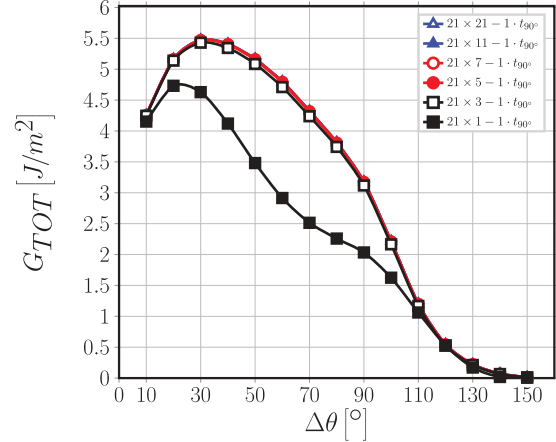

Figure 8. Effect of the presence of undamaged fiber rows in the 90° layer on debond-0°/90° interface interaction for Mode I ERR: models $1 \times k - 1 \cdot t_{90°}$. $V_f = 60\%$, $\bar{\varepsilon}_x = 1\%$.
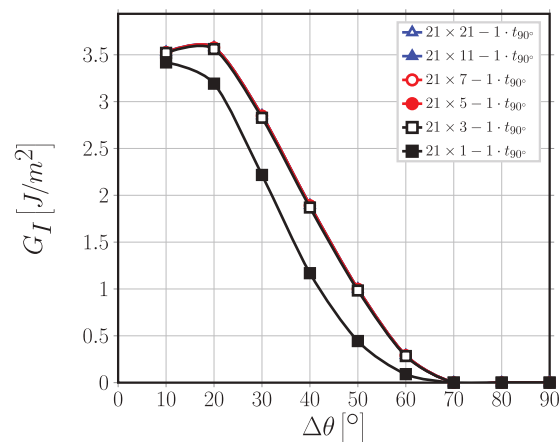
Figure 10. Effect of the presence of undamaged fiber rows in the 90° layer on debond-0°/90° interface interaction for Mode I ERR: models $n \times k - 1 \cdot t_{90°}$. $V_f = 60\%$, $\bar{\varepsilon}_x = 1\%$.

Figure 11. Effect of the presence of undamaged fiber rows in the 90° layer on debond-0°/90° interface interaction for Mode II ERR: models $n \times k - 1 \cdot t_{90°}$. $V_f = 60\%$, $\bar{\varepsilon}_x = 1\%$.

Figure 12. Effect of the presence of undamaged fiber rows in the 90° layer on debond-0°/90° interface interaction for total ERR: models $n \times k - 1 \cdot t_{90°}$. $V_f = 60\%$, $\bar{\varepsilon}_x = 1\%$.

Analogous results can be found in Velasco et al.[36] and París et al.,[37] where the authors investigate the ply-thickness effect on debond growth in cross-ply laminates using: first, a single centrally-placed partially debonded fiber with surrounding matrix corresponding to $V_f = 55\%$, embedded from all sides in a homogenized 90° ply bounded by homogenized 0° layers; second, one partially debonded fiber placed in the center and a second partially debonded fiber placed at an angle θ_2 with respect to the horizontal direction with surrounding matrix corresponding to $V_f = 55\%$, embedded from all sides in a homogenized 90° ply bounded by homogenized 0° layers. The thickness of the 0° layer is chosen as reference and a $[0°_p, 90°_{r \cdot p}]_S$ laminate is considered. Carbon–epoxy and glass–epoxy systems are both studied. The thickness of the 90° ply, $t_{90°} = r \cdot t_{0°}$, varies from $r = 3$ (thick 90° ply, >100 fiber diameters) to $r = 0.1$ (thin 90° ply, ~4 − 5 fiber diameters). No measurable ply-thickness effect was observed. Experimental support to the claim that the ply-thickness effect has no influence on debond growth can be also found in the literature, in Saito et al.[6] The authors conducted in-situ observations of edge micro-cracks with an optical microscope on $[0°_2, 90°_n, 0°_2]$ carbon fiber–epoxy laminates with $n = 1$, 2, 4, corresponding to a 90° ply thickness of respectively 40 [μm] (~6 − 8 fiber diameters), 80 [μm] (~12 − 16 fiber diameters), and 160 [μm] (~24 − 32 fiber diameters). For $n = 1$, i.e. the case of a very thin 90° ply, isolated debonds appear at a lower value of the applied strain than in thicker plies (at 0.4% vs 0.7%), while growth and coalescence of debonds is suppressed and no transverse crack can be observed even at a strain of 1.5%. The ply-thickness effect was thus observed in Saito et al.[6] for transverse cracks, i.e. coalescence of

debonds was delayed to higher strains and even suppressed, but not for debond growth. The analysis presented in this article brings new arguments to the claim that the ply-thickness effect does not influence the growth of debonds.

It is finally worth to devote some space to the total ERR G_{TOT}, which is computed as

$$G_{TOT} = G_I + G_{II} \tag{8}$$

i.e. as the sum of Mode I and Mode II ERR evaluated using the VCCT. The total ERR for models $21 \times k - 1 t_{90°}$ is shown in Figure 12.

Comparing Figure 12 with Figures 10 and 11, it is possible to observe that for smaller debonds ($\Delta\theta < 40° − 50°$), where $G_I > G_{II}$, the profile of G_{TOT} is very close to that of G_I, i.e. it is G_I−dominated; for larger debonds ($\Delta\theta > 50° − 60°$), where $G_I \rightarrow 0$, the profile of G_{TOT} is almost identical to that of G_{II}, i.e. it is G_{II}−dominated. Comparing total ERR between different RVE provides results analogous to those derived for G_I and G_{II}. These conclusions apply for every different RVE considered in the present work. The total ERR might be relevant only in the determination of the maximum size of the debond, when it is compared with the value of a critical ERR G_c which is a function of material properties and of the mode ratio $\psi = \sqrt{\frac{G_{II}}{G_I}}$. Other authors however prefer to adopt a power-law criterion expressed as a function of G_I and G_{II} to describe debond propagation and to estimate its size. Agreement is still lacking on the formulation of a criterion for debond propagation and thus the case for a detailed analysis of G_{TOT} is weaker than for Mode I and Mode II ERR. At the moment, it is the analysis of G_I and G_{II} that provides the greatest insights

into the mechanics of debond growth and it is for this reason that we decided to focus in this paper on the discussion of Mode I and Mode II ERR instead of the total ERR.

Conclusions

Different models of RUC, representing different cross-ply laminates, have been studied in order to investigate the effect of the presence of the $0°$ layer and of its thickness on debond ERR for interactive and non-interactive debonds. A particular damage state is studied, in which only the central row of fibers of the $90°$ ply possesses debonds. The thickness of the $90°$ ply is measured in terms of the number of fiber rows in the layer; the $0°$ layer is on the other hand modeled as a homogenized material, the thickness of which is a multiple of the $90°$ ply thickness. In order to investigate the mechanisms of the debond-$0°/90°$ interface interaction, Mode I and Mode II ERR of cross-ply RUCs are compared with those of RUCs with equivalent boundary conditions on the upper boundary: free surface; coupling conditions on the vertical displacements; an applied linear distribution of the horizontal displacement; and coupling conditions on the vertical displacements superimposed to an applied linear distribution of the horizontal displacement (this last combination represents the most extreme effect of the $0°$ layer on debond growth). It has been found that:

- by forcing the $0°/90°$ interface to remain approximately straight and controlling, the uniformity of the horizontal displacements in the composite (and thus in the $90°$ ply), the presence of the $0°$ layer causes more homogeneous local (i.e. in the debond neighborhood) strains, reducing the ERR at the debond crack tip;
- when increasing the thickness of the $0°$ layer, the effect of the presence of the $0°$ layer on debond ERR remains the same as in the case $t_{0°} = t_{90°}$;
- no effect of the $90°$ layer thickness, measured in terms of number of fiber rows, is observed; a reduction in ERR takes place only when the thickness is reduced to only one fiber row.

The results reported in this article strengthen the claim that the ply-thickness effect does not influence the growth of individual debonds, as previously suggested in the literature.[6,18,36,37]

Declaration of Conflicting Interests

The author(s) declared no potential conflicts of interest with respect to the research, authorship, and/or publication of this article.

ORCID iD

Luca Di Stasio https://orcid.org/0000-0002-9261-301X

References

1. Kawabe K. New spreading technology for carbon fiber tow and its application to composite materials. *Sen'i Gakkaishi* 2008; 64: 262–267.
2. Yamaguchi K and Hahn H. The improved ply cracking resistance of thin-ply laminates. In: *Proceedings of the 15th international conference on composite materials (ICCM-15)*. Tokyo, Japan, 27 June–02 July 2005. SAMPE.
3. Sihn S, Kim R, Kawabe K, et al. Experimental studies of thin-ply laminated composites. *Compos Sci Technol* 2007; 67: 996–1008.
4. Yokozeki T, Aoki Y and Ogasawara T. Experimental characterization of strength and damage resistance properties of thin-ply carbon fiber/toughened epoxy laminates. *Compos Struct* 2008; 82: 382–389.
5. Yokozeki T, Kuroda A, Yoshimura A, et al. Damage characterization in thin-ply composite laminates under out-of-plane transverse loadings. *Compos Struct* 2010; 93: 49–57.
6. Saito H, Takeuchi H and Kimpara I. Experimental evaluation of the damage growth restraining in 90 layer of thin-ply cfrp cross-ply laminates. *Adv Compos Mater* 2012; 21: 57–66.
7. Arteiro A, Catalanotti G, Xavier J, et al. Notched response of non-crimp fabric thin-ply laminates. *Compos Sci Technol* 2013; 79: 97–114.
8. Arteiro A, Catalanotti G, Xavier J, et al. Large damage capability of non-crimp fabric thin-ply laminates. *Composites Part A* 2014; 63: 110–122.
9. Amacher R, Cugnoni J, Botsis J, et al. Thin ply composites: experimental characterization and modeling of size-effects. *Compos Sci Technol* 2014; 101: 121–132.
10. Guillamet G, Turon A, Costa J, et al. Damage occurrence at edges of non-crimp-fabric thin-ply laminates under off-axis uniaxial loading. *Compos Sci Technol* 2014; 98: 44–50.
11. Cugnoni J, Amacher R, Kohler S, et al. Towards aerospace grade thin-ply composites: effect of ply thickness, fibre, matrix and interlayer toughening on strength and damage tolerance. *Compos Sci Technol* 2018; 168: 467–477.
12. Kopp A, Stappert S, Mattsson D, et al. The aurora space launcher concept. *CEAS Space J* 2017; 10: 167–187.
13. Bailey JE and Parvizi A. On fibre debonding effects and the mechanism of transverse-ply failure in cross-ply

laminates of glass fibre/thermoset composites. *J Mater Sci* 1981; 16: 649–659.

14. Krueger R, Shivakumar KN and Raju IS. Fracture mechanics analyses for interface crack problems – a review. In: *54th AIAA/ASME/ASCE/AHS/ASC structures, structural dynamics, and materials conference*, Boston, Massachusett, 8–11 April 2013. Reston, Virginia: American Institute of Aeronautics and Astronautics.

15. Kushch V, Shmegera S, Brøndsted P, et al. Numerical simulation of progressive debonding in fiber reinforced composite under transverse loading. *Int J Eng Sci* 2011; 49: 17–29.

16. Canal LP, González C, Segurado J, et al. Intraply fracture of fiber-reinforced composites: microscopic mechanisms and modeling. *Compos Sci Technol* 2012; 72: 1223–1232.

17. Bouhala L, Makradi A, Belouettar S, et al. Modelling of failure in long fibres reinforced composites by x-FEM and cohesive zone model. *Composites Part B* 2013; 55: 352–361.

18. Herráez M, Mora D, Naya F, et al. Transverse cracking of cross-ply laminates: a computational micromechanics perspective. *Compos Sci Technol* 2015; 110: 196–204.

19. Mantič V. Interface crack onset at a circular cylindrical inclusion under a remote transverse tension. Application of a coupled stress and energy criterion. *Int J Solids Struct* 2009; 46: 1287–1304.

20. Freed Y and Banks-Sills L. A new cohesive zone model for mixed mode interface fracture in bimaterials. *Eng Fract Mech* 2008; 75: 4583–4593.

21. Jin ZH and Sun C. Cohesive zone modeling of interface fracture in elastic bi-materials. *Eng Fract Mech* 2005; 72: 1805–1817.

22. Asp LE, Berglund LA and Gudmundson P. Effects of a composite-like stress state on the fracture of epoxies. *Compos Sci Technol* 1995; 53: 27–37.

23. Pawlak A, Galeski A and Rozanski A. Cavitation during deformation of semicrystalline polymers. *Prog Polym Sci* 2014; 39: 921–958.

24. Krueger R. Virtual crack closure technique: history, approach, and applications. *Appl Mech Rev* 2004; 57: 109.

25. Rice JR. A path independent integral and the approximate analysis of strain concentration by notches and cracks. *J Appl Mech* 1968; 35: 379.

26. Toya M. A crack along the interface of a circular inclusion embedded in an infinite solid. *J Mech Phys Solids* 1974; 22: 325–348.

27. París F, Caño JC and Varna J. The fiber-matrix interface crack — a numerical analysis using boundary elements. *Int J Fract* 1996; 82: 11–29.

28. Zhuang L, Pupurs A, Varna J, et al. Effects of inter-fiber spacing on fiber-matrix debond crack growth in unidirectional composites under transverse loading. *Composites Part A* 2018; 109: 463–471.

29. Muñoz-Reja M, Távara L, Mantič V, et al. Crack onset and propagation at fibre–matrix elastic interfaces under biaxial loading using finite fracture mechanics. *Composites Part A* 2016; 82: 267–278.

30. Correa E, Mantič V and París F. Effect of thermal residual stresses on matrix failure under transverse tension at micromechanical level: a numerical and experimental analysis. *Compos Sci Technol* 2011; 71: 622–629.

31. Correa E, París F and Mantič V. Effect of the presence of a secondary transverse load on the inter-fibre failure under tension. *Eng Fract Mech* 2013; 103: 174–189.

32. Correa E, París F and Mantič V. Effect of a secondary transverse load on the inter-fibre failure under compression. *Composites Part B* 2014; 65: 57–68.

33. Sandino C, Correa E and París F. Numerical analysis of the influence of a nearby fibre on the interface crack growth in composites under transverse tensile load. *Eng Fract Mech* 2016; 168: 58–75.

34. Sandino C, Correa E and París F. Interface crack growth under transverse compression: nearby fibre effect, Athens, Greece, 24–28 June 2018. In: *Proceeding of the 18th European conference on composite materials (ECCM-18)*.

35. Varna J, Zhuang LQ, Pupurs A, et al. Growth and interaction of debonds in local clusters of fibers in unidirectional composites during transverse loading. *Key Eng Mater* 2017; 754: 63–66.

36. Velasco M, Graciani E, Távara L, et al. BEM multiscale modelling involving micromechanical damage in fibrous composites. *Eng Anal Boundary Elem* 2018; 93: 1–9.

37. París F, Velasco ML and Correa E. Micromechanical study on the influence of scale effect in the first stage of damage in composites. *Compos Sci Technol* 2018; 160: 1–8.

38. Simulia, Providence, RI, USA. *ABAQUS/Standard User's Manual, Version 6.12*, 2012.

39. Zhang H, Ericson M, Varna J, et al. Transverse single-fibre test for interfacial debonding in composites: 1. Experimental observations. *Composites Part A* 1997; 28: 309–315.

40. Di Stasio L, Varna J and Ayadi Z. Energy release rate of the fiber/matrix interface crack in UD composites under transverse loading: effect of the fiber volume fraction and of the distance to the free surface and to non-adjacent debonds. *Theor Appl Fract Mech* 2019; 103: 102251.

41. Teixeira R, Pinho S and Robinson P. Thickness-dependence of the translaminar fracture toughness: experimental study using thin-ply composites. *Composites Part A* 2016; 90: 33–44.

42. Garrido J, Foces A and Paris F. B.e.m. applied to receding contact problems with friction. *Math Comput Modell* 1991; 15: 143–153.

43. Keer LM, Dundurs J and Tsai KC. Problems involving a receding contact between a layer and a half space. *J Appl Mech* 1972; 39: 1115.

44. Tsai KC, Dundurs J and Keer LM. Elastic layer pressed against a half space. *J Appl Mech* 1974; 41: 703.

45. Hashin Z. Analysis of composite materials—a survey. *J Appl Mech* 1983; 50: 481.

46. Christensen R and Lo K. Solutions for effective shear properties in three phase sphere and cylinder models. *J Mech Phys Solids* 1979; 27: 315–330.

47. París F, Correa E and Mantič V. Kinking of transversal interface cracks between fiber and matrix. *J Appl Mech* 2007; 74: 703.

48. Varna J, París F and CCaño J. The effect of crack-face contact on fiber/matrix debonding in transverse tensile loading. *Compos Sci Technol* 1997; 57: 523–532.

49. Varna J. 2.10 crack separation based models for microcracking. In: Carl H Zweben and Peter Beaumont (eds) *Comprehensive composite materials II*. Amsterdam, the Netherlands: Elsevier, 2018, pp.192–220.

Energy release rate of the fiber/matrix interface crack in UD composites under transverse loading: Effect of the fiber volume fraction and of the distance to the free surface and to non-adjacent debonds

Luca Di Stasio[a,b,*], Janis Varna[b], Zoubir Ayadi[a]

[a] *Université de Lorraine, EEIGM, IJL, 6 Rue Bastien Lepage, F-54010 Nancy, France*
[b] *Luleå University of Technology, University Campus, SE-97187 Luleå, Sweden*

A B S T R A C T

The effects of crack shielding, finite thickness of the composite and fiber content on fiber/matrix debond growth in thin unidirectional composites are investigated analyzing Representative Volume Elements (RVEs) of different ordered microstructures. Debond growth is characterized by estimation of the Energy Release Rates (ERRs) in Mode I and Mode II using the Virtual Crack Closure Technique (VCCT) and the J-integral. It is found that increasing fiber content, a larger distance between debonds in the loading direction and the presence of a free surface close to the debond have all a strong enhancing effect on the ERR. The presence of fully bonded fibers in the composite thickness direction has instead a constraining effect, and it is shown to be very localized. An explanation of these observations is proposed based on mechanical considerations.

1. Introduction

Stimulated by the ever more stringent requirements in terms of weight and mechanical performances of the aerospace industry, in recent years the composite community has returned its attention to the mechanisms of intralaminar crack initiation with a focus on thin-ply laminates. Alternative design approaches are now considered based on this non-conventional laminate in applications ranging from cryogenic pressure vessels [1], to airplanes' wings [2], and even reusable space launchers [3].

Thin-ply laminates are the result of a technological innovation, the *spread tow technology*, which consists in opening or spreading the tows, in which fibers (carbon, glass, aramid, basalt among others) are usually shipped in, into very thin tapes used for laminate production. Ply thicknesses of less than $50 \, \mu m$ can nowadays be mass-produced, and record thicknesses of around $20 - 25 \, \mu m$, or $\sim 4 - 5$ times the average fiber's diameter, have been achieved. In its current form the technique, sometimes referred to as "FUKUI method", was firstly proposed towards the end of the 1990s [4] and perfected in the subsequent decade [5,6].

Several experimental investigations on *thin ply* laminates have highlighted their main properties [7–13]: increased fiber content; more uniform packing of fibers; delay and even suppression of intralaminar cracking (called also transverse-, matrix- or micro-cracking) and delamination. A very insightful work documenting how these phenomena

are affected by the morphology of *thin-ply* laminates is the microscopic study of Saito et al. [14], which focuses on the effect of ply thickness on the onset and propagation of intralaminar cracking. In their investigation, tensile tests were performed on carbon fiber/epoxy $[0_2, 90_n, 0_2]$*thin-ply* laminates for $n = 1, 2, 4$ and the crack density was measured with a digital microscope at several levels of applied tensile strain in the range between 0% and 1.5%. Furthermore, they performed microscopic observations on the specimen's edge at each level of strain. They observed the onset of fiber/matrix interface cracks (referred to as debonds in the following) at lower levels of strain in thinner plies, while at the same time coalescence of debonds and through-the-thickness propagation of transverse cracks in thin plies were delayed and even suppressed as ply thickness decreased. In particular, they reported the first onset of debonds at 0.4% for $n = 1, 2$ and 0.7% for $n = 4$. For $n = 1$, however, at $\varepsilon = 1.5\%$ coalescence of debonds had started to take place but the crack had not completely propagated through the thickness, while for $n = 2$ and $n = 4$ the latter already happened at a value of strain respectively of 1.3% and 1%. Our inability to explain these observations with the currently accumulated knowledge demonstrates the necessity of further investigation of interactions between debonds and studies of the constraining (or accelerating) effect of presence of bonded fibers, free and constrained boundaries in the vicinity of a partially debonded fiber.

Early studies on the effect of ply thickness on the onset and

---

propagation of transverse cracks were conducted on glass fiber/epoxy cross-ply laminates by Bailey, Parvizi and collaborators [15–17], who firstly observed the beneficial effect of thickness reduction on the delay of transverse cracking. They furthermore pointed the attention to the appearance of debonds at the fiber/matrix interface and their subsequent coalescence as the mechanism at the origin of transverse cracks [18]. Moreover, they identified the main mechanical driver of the damage process in the mismatch of elastic properties, and particularly of Poisson's ratios, between fibers and matrix [19]. A full understanding of damage onset and propagation in *thin-ply* laminates thus requires comprehension of the mechanisms governing its very first stage, i.e. the fiber/matrix interface crack. First results were obtained through analytical models in the case of a single fiber with an arc crack (debond) in an infinite matrix under transverse tension by England [20] and Perlman & Sih [21], who obtained the stresses at the interface and calculated the stress intensity factors at the crack tip, and by Toya [22], who evaluated the Energy Release Rate (ERR). Drawing upon the results for the straight bi-material interface crack by Comninou [23], the effect of crack face contact in fiber–matrix debonding was investigated in [24,25]. In [26], it was showed in terms of ERR why the case of a single asymmetric debond is more likely to be observed under remote transverse tension than two symmetric debonds on the same fiber. The effect of different types and combinations of loads on debonding have been studied for the single fiber model: compression [27], residual thermal stresses [28], and biaxial configurations with different combinations of tension and compression [29,30]. The effect of the presence of nearby bonded fibers on the debonding of a fiber embedded in an infinite matrix has been studied under uniaxial transverse tension [31], biaxial tension [32] and uniaxial transverse compression [33]. The effect of inter-fiber distance on debond growth has been studied for a partially debonded fiber at the center of a hexagonal cluster inside a homogenized UD composite in the case of fully bonded neighbouring fibers [34] and of two partially debonded fibers out of the surrounding six [35]. An understanding of crack shielding and finite ply thickness effects on debond growth in non-homogenized microstructural models of UDs seems thus to be lacking: this is the problem that we want to address in the present work. Mode I and Mode II energy release rates will be analyzed using stress fields calculated with the FEM for a variety of Repeating Unit Cell (RUC) of the composite with square packing of fibers under transverse tensile loading. The choice of a square packing configuration for the fibers is motivated by its simplicity, as it allows to easily separate the effect of fibers (fully bonded and/or partially debonded) placed along the loading direction from that of fibers placed in the through-the-ply-thickness direction. These RUCs represent composites with different distances between partially debonded fibers and a varying number of bonded fibers between them, which allows to study the effect of crack shielding on the ERR. In the ply thickness direction, the varying number of perfectly bonded fiber rows exposes the effect of the proximity of the free boundary of the composite on debond growth. Finally, using coupling of thickness direction displacements on horizontal boundaries of the RUC, the accelerating effect of the interaction between debonds of fibers located on the same vertical line is studied.

2. RVE models & FE discretization

2.1. Introduction & nomenclature

In this paper, we analyze debond development in unidirectional (UD) composites subjected to in-plane transverse tensile loading. The interaction between debonds in UD composites is studied developing models of different Repeating Unit Cells (RUC) of laminates (see Figs. 1–3) where only the central fiber in the cell has a damage in the form of a fiber/matrix interface crack (debond). The composite RUC may be repeating in the in-plane transverse direction only (representing an ultra-thin composite) or repeating also in the composite thickness direction, representing an infinite composite in a limiting case. Thus,

the conditions at the UD composite's upper and lower boundaries are one of the parameters for the investigation. The used RUCs allow for considering the composite with debonds as a sequence of stacked damaged and undamaged fiber rows, each row with only one fiber in the thickness direction. Since all of these RUCs feature regular microstructures with fibers placed according to a square-packing configuration, they are Representative Volume Elements (RVE) of composites with a certain distribution of debonds. Introducing in-plane coordinates x and y, where x is in the transverse direction of the UD composite under consideration, the strain in the y-direction due to a load in the x-direction is small, caused in turn by the very small minor Poisson's ratio of the UD composite. Additionally, debonds are considered to be significantly longer in the fiber direction than in the arc direction. Therefore, we use 2D models under the assumption of plane strain, defined in the $x - z$ section of the composite. Thus, the analysis presented applies to long debonds, with a focus on understanding the mechanisms of growth along their arc direction. The composites are subjected to transverse tensile strain, applied as a constant displacement in the x-direction along the vertical boundary of the RUC as shown in Figs. 1–4. As the models are differentiated by the number of rows of fibers and by the spacing between debonds along the vertical and horizontal directions, the corresponding RUCs can be distinguished from each other based on the number n of fibers in the horizontal direction and k in the vertical direction. Furthermore, the horizontal surfaces can be either free or vertical displacement coupling can be applied. We thus introduce a common notation $n \times k - free$ and $n \times k - coupling$ to denote a RUC with $n \times k$ fibers and, respectively, a free upper surface or with kinematic coupling applied to it. The specific combinations of particular choices of n, k, and boundary conditions are detailed in Section 2.2, together with the description of the corresponding models of damaged composite they are representing.

### 2.2. Models of Representative Volume Element (RVE)

The first two models feature, as shown in Fig. 1, an ultra-thin UD laminate with only one row of fibers across its thickness, $k = 1$. This is quite an extreme model from the microstructural point of view; however, it allows to focus the analysis on the interaction between debonded fibers placed along the x-direction. Furthermore, as the horizontal surfaces are considered free, the interaction is stronger in this case than in any other, making the trends very clear and the predictions of this model rather conservative. In retrospective, if only 20 years ago such a model would have been considered too abstracted from the physical reality, the recent advancements in the spread tow technology make this approach appealing also as a limiting case for practical considerations.

In the sub-model of Fig. 1a, every n^{th} fiber in the composite is partially debonded on alternating sides of the fiber. The symmetries of the model allow the use of the upper part of the RUC, as highlighted in Figs. 1–3. Following the notation introduced in Section 2.1, we will refer to this model as $n \times 1 - free$. In the sub-model $n = 1$, Fig. 1b, a debond appears on each fiber on alternating sides and the corresponding RUC contains only one fiber. We will refer to this model as $1 \times 1 - free$.

The second set of models in Figs. 2 and 3 considers laminates with multiple rows of fibers across the thickness: a finite number of rows in the first two sub-models in Fig. 2; an infinite number in the model of Fig. 3. In Fig. 2a, the RUC contains $n = 1$ fiber in the x-direction, k fibers across the thickness and the central fiber is debonded. This model will be referred to in the following as $1 \times k - free$. Thinking in terms of rows, in this model we have a central row where each fiber is debonded. This row is surrounded from each side by $(k - 1)/2$ rows with perfectly bonded fibers. In the sub-model in Fig. 2b, each nth fiber in the central row is debonded and this row is surrounded by $(k - 1)/2$ rows of undamaged fibers from each side. We will refer to this model as $n \times k - free$ (because the horizontal boundary of the RUC is free of any constraint).
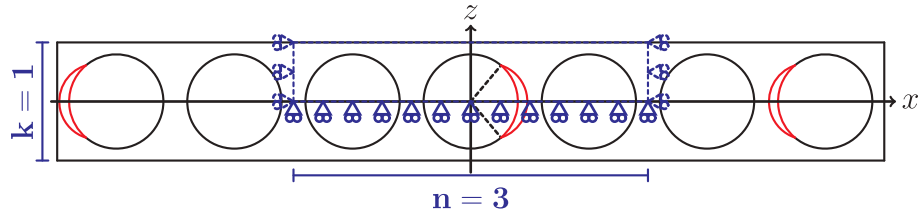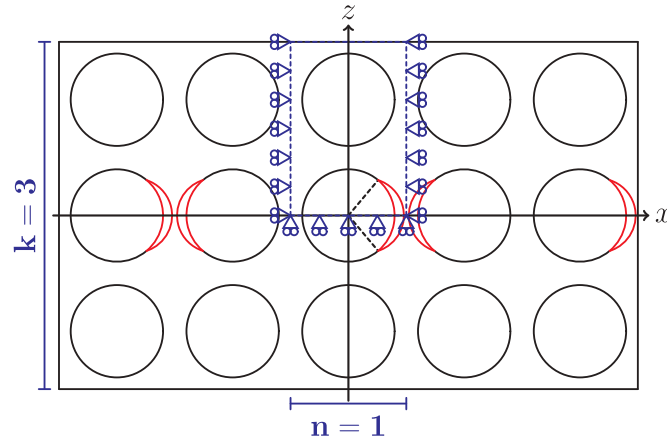
(a) Single row of fibers with a debond appearing every n fibers: model $n \times 1 - free$ ($n = 3$ in the figure).
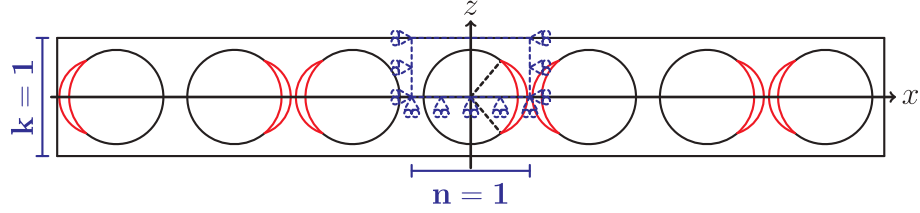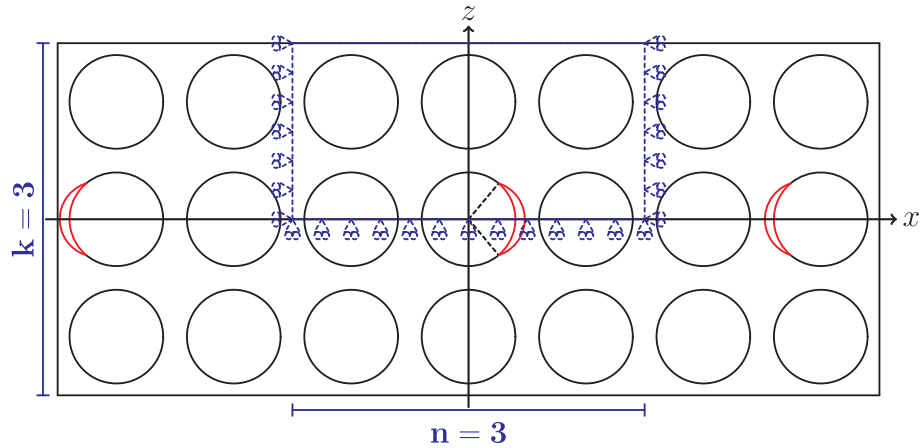

(b) Single row of fibers with debonds appearing on each fiber: model $1 \times 1 - free$.

Fig. 1. Models of ultra-thin UD composites with a single "row" of fibers and debonds repeating at different distances.

(a) Multiple rows of fibers with debonds appearing on each fiber beloging to the central row: model $1 \times k - free$ ($k = 3$ in the figure).

(b) Mutiple rows of fibers with a debond appearing every n fibers within the central row: model $n \times k - free$ ($n = 3$ and $k = 3$ in the figure).

Fig. 2. Models of UD composites with different "rows" of fibers and debonds repeating at different distances.
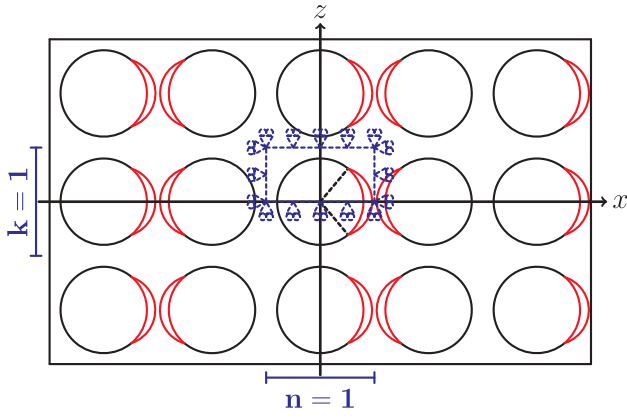
Fig. 3. Model of UD composites with an infinite number of "rows" of fibers and debonds appearing on each fiber: model $1 \times 1 - coupling$.
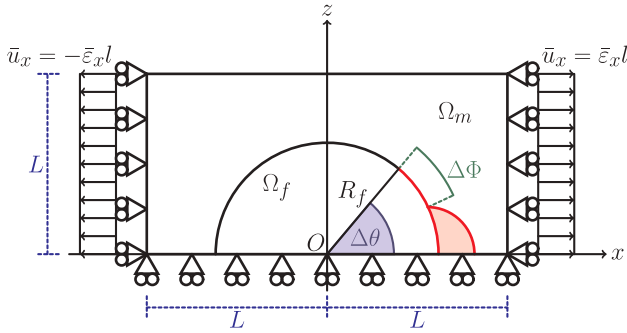

Fig. 4. Schematic of the model with its main parameters.

Finally, the model in Fig. 3 represents an UD composite with an infinite number of rows; all of them with partially debonded fibers. As all fibers have debonds, the corresponding RUC is made of a single partially debonded fiber with kinematic coupling conditions applied to the upper boundary to assure periodicity. This model is referred to as $1 \times 1 - coupling$.

2.3. Finite Element (FE) discretization

Each RUC is discretized using the Finite Element Method (FEM) within the Abaqus environment, a commercial FEM package [36]. The length l and height h of the model are determined by the number of fibers n in the horizontal direction and k across the thickness (see Section 2.2) according to Eq. (1):

$$l = 2nL \qquad h = kL;$$ (1)

where $2L$ is the length of a one-fiber unit, see Fig. 4, defined as a function of the fiber volume fraction V_f and the fiber radius according to

$$L = \frac{R_f}{2}\sqrt{\frac{\pi}{V_f}}.$$ (2)

The fiber radius R_f is assumed to be the same for each fiber in the model and equal to 1 μm. The latter value is not physical and it has been chosen for simplicity. It is worth to note at this point that, in a linear elastic solution as the one presented here, the ERR is proportional to the geometrical dimensions and recalculation of the ERR for fibers of any size, thus, requires a simple multiplication. Furthermore, notice that the relationships in Eqs. (1) and (2) ensure that the local and global V_f are everywhere equal.

The debond is placed symmetrically with respect to the x axis (see Fig. 4) and we characterize it with an angular size of $\Delta\theta$ (the full debond size is thus $2\Delta\theta$). For large debond sizes ($\geqslant 60° - 80°$), a region of

variable size $\Delta\Phi$ appears at the crack tip in which the crack faces are in contact and slide on each other. Due to its appearance, frictionless contact is considered between the two crack faces to allow free sliding and avoid interpenetration. The presence of friction at the interface is considered in [37], where the authors model the contact interaction between crack faces using Coulomb's friction with a coefficient $\mu = 0.25$ and show that, for a debond with $\Delta\theta = 80°$, the crack sliding displacement is always different from zero in every point of the crack and only slightly lower than that of the frictionless case. This in turn means that the estimation of G_{II} in the case of frictionless contact provide an upper bound and thus the results presented here represent a conservative estimation (a higher ERR corresponds to higher likelihood of crack propagation). Symmetry with respect to the x axis is applied on the lower boundary. The upper boundary is in general free, except for the model $1 \times 1 - coupling$ (Fig. 3) which requires kinematic coupling of vertical displacements also on the upper side. Kinematic coupling on the x-displacement is applied along the left and right sides of the model in the form of a constant x-displacement $\pm \bar{\varepsilon}_x l$, corresponding to transverse strain $\bar{\varepsilon}_x$ equal to 1%.

The model is meshed using second order, 2D, plane strain triangular (CPE6) and rectangular (CPE8) elements, which have respectively 6 and 8 nodes per element. Each node has 2 degrees of freedom, i.e. the horizontal displacement u_x and the vertical displacement u_z. A regular mesh of quadrilateral elements with an almost unitary aspect ratio is required at the crack tip. The angular size δ of an element in the crack tip region is always equal to 0.05°. The overall number of elements needed to discretize the model depends on the debond size $\Delta\theta$ (larger debonds have larger contact zones which require more elements for their correct resolution), the fiber volume fraction (which determines the size of the RVE) and the number of fully bonded fibers present in the model. As an example, the discretization of the $1 \times 1 - free$ model at $V_f = 60\%$ requires a total of 132507 elements for $\Delta\theta = 10°$ and of 296606 elements for $\Delta\theta = 140°$, which corresponds to a minimum required RAM respectively of 445 MB and 1014 MB and to a minimum RAM needed to minimize I/O operations respectively of 1.63 GB and 3.87 GB. To put it into perspective, the wallclock time required for their solution is respectively 1.3 [min] and 14.95 [min] on a laptop with a 2.5 GHz Intel Core i5 processor and 6 GB of installed RAM. The crack faces are modeled as element-based surfaces and a small-sliding contact pair interaction with no friction is established between them. The Mode I, Mode II and total Energy Release Rates (ERRs) (respectively referred to as G_I, G_{II} and G_{TOT}) represent the main output of the FEM analysis; they are evaluated using the VCCT [38] implemented in a custom Python routine and, for the total ERR, the J-integral [39] is obtained by application of the Abaqus built-in functionality. A glass fiber-epoxy system is considered throughout this paper, and it is assumed that their response lies always in the linear elastic domain. The latter assumption lies on the work of Asp and co-workers, who show that epoxy subjected to a tri-axial stress state as the one observable in the inter-fibers region fails at very low strains ($\sim 0.5\% - 0.8\%$) [40] and in a brittle manner [41], and that the magnitude of deviatoric stresses (evaluated in terms of equivalent Von Mises stress) in the fiber/matrix interface neighborhood does not justify the occurrence of plastic deformations in the case of debond propagation [41]. The properties used are listed in Table 1.

Table 1
Summary of the mechanical properties of fiber and matrix. E stands for Young's modulus, μ for shear modulus and ν for Poisson's ratio.

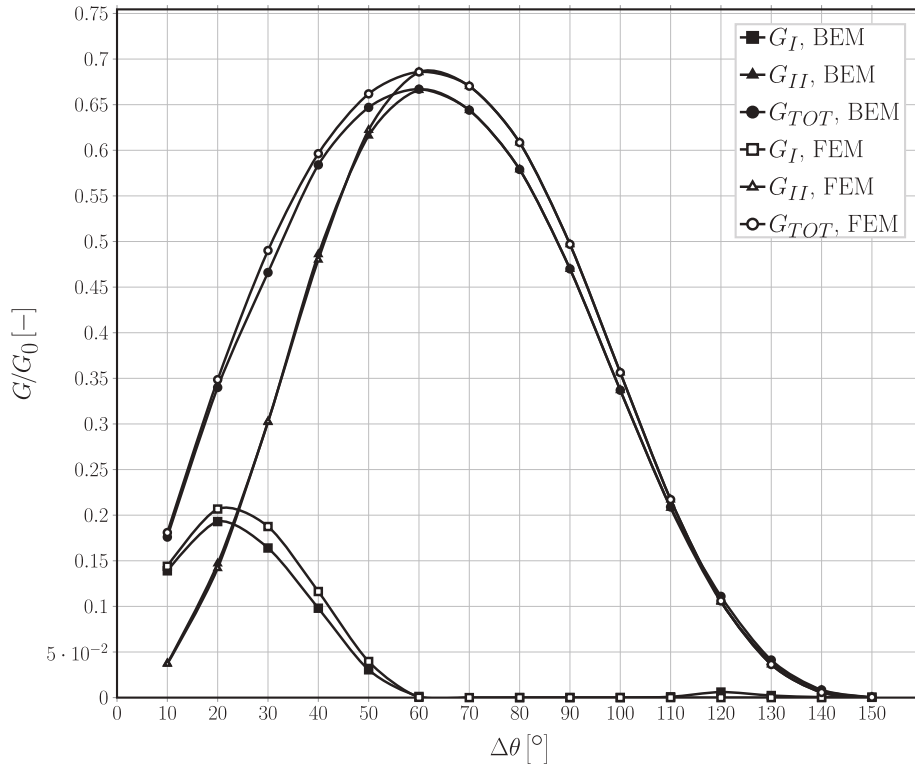| Material	E [GPa]	μ [GPa]	ν [−]
Glass fiber	70.0	29.2	0.2
Epoxy	3.5	1.25	0.4

Fig. 5. Validation of the single fiber model for the infinite matrix case with respect to the BEM solution in [31].

2.4. Validation of the model

The model is validated in Fig. 5 against the results reported in [42,31], obtained with the Boundary Element Method (BEM) for a single fiber with a symmetric debond placed in an infinite matrix. This situation is modeled using the $1 \times 1 - free$ RVE with $V_f = 0.0079\%$, which corresponds to a RUC's length and height of respectively $\sim 200 R_f$ and $\sim 100 R_f$.

To allow for a comparison, the results are normalized following [31] with respect to a reference Energy Release Rate G_0 defined as

$$G_0 = \frac{1 + k_m}{8 \mu_m} \sigma_0^2 \pi R_f \tag{3}$$

where μ is the shear modulus, k is the Kolosov's constant defined as $3 - 4\nu$ for plane strain conditions, R_f is the fiber radius and the index m refers to the properties of the matrix. σ_0 is the stress at the boundary, computed as the average of the stress extracted at each boundary node along the right side (arithmetic average as nodes are equispaced by design along both the left and right sides). The agreement is good: the difference between the BEM solution, which is considered more accurate, and the FEM solution does not exceed 5%. The ERRs' maxima are in the same positions and the size of the contact zone is the same. Nevertheless, an analysis of phenomena leading to less than 5% differences in ERR would not be reliable and, therefore, it is not recommended.

3. Results & discussion

3.1. Effect of fiber volume fraction

As shown in Figs. 6 and 7, respectively for Mode I and Mode II, the fiber content has a drastic effect on the Energy Release Rate at the tip of the fiber/matrix interface crack. The effect of four levels of fiber volume fraction are compared, 30%, 50%, 60% and 65%, on two microstructural models: a $11 \times 11 - free$ (every 11th fiber in the central fiber row is

partially debonded and, on the top of this row, we have 5 undamaged fiber rows), Figs. 6a and 7a, and a $21 \times 21 - free$ (every 21th fiber in the central fiber row is partially debonded and, on the top of this row, we have 10 undamaged fiber rows), Figs. 6b and 7b.

Comparing Fig. 6a with b, and Fig. 7a with b, we can observe that the ERRs' values are very similar for RUCs with 11×11 and 21×21 fibers, though they are slightly higher for the larger RUC where the next debonded fiber and the free surface are further away from the debonded fiber. From these results we conclude that both RUCs are large enough to represent a single debonded fiber in an infinite array of bonded fibers. Obviously, there exists a specific effect of the fiber content. For Mode I, Fig. 6, the maximum value of the ERR increases by ~ 5.2 times when V_f changes from 30% to 65%. The debond's angular size for which the peak value occurs remains unchanged at 20°, but for $V_f = 60\%$ and 65% the values of Mode I ERR are rather similar when measured at 10° and at 20°, approximately creating a plateau. Furthermore, increasing the fiber volume fraction delays the onset of the contact zone, which corresponds in Fig. 6 to the first value of $\Delta\theta$ for which G_I is equal to zero. For $V_f = 30\%$, the contact zone first appears for a debond of 60°, similarly to what happens in the single fiber in infinite matrix model (Fig. 5). For higher fiber contents, the contact zone's onset is delayed to a debond's size approximately equal to 70°.

For Mode II, Fig. 7, there is a distinct maximum in the curve and its shape does not depend on the fiber content. The maximum value of the ERR increases by ~ 2.1 times when V_f changes from 30% to 65%. The effect is thus similar to Mode I, but with a significantly lower magnitude. Similar to Mode I, the debond's size for which the peak value of Mode II occurs remains unchanged, at 60°. It is worthwhile to notice that the ratio of Mode II to Mode I peak values is $\frac{max(G_{II})}{max(G_I)} \sim \frac{2.2}{0.9} \sim 2.4$ for $V_f = 30\%$, while it is $\sim \frac{4.7}{4.7} \sim 1$ for $V_f = 65\%$.

The general increasing trends observed in Figs. 6 and 7 are related to the fact that, given that the global and local V_f are everywhere identical in the models presented, an increase in fiber content corresponds to a decrease in the average distance between fibers. Thus, the distances for the decay of the local stress and strain fields in the matrix
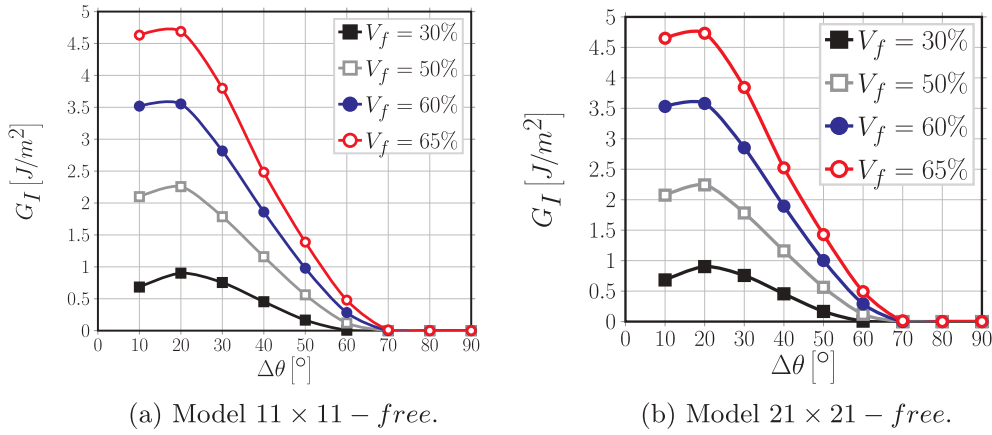
(a) Model $11 \times 11 - free$.   (b) Model $21 \times 21 - free$.

Fig. 6. A view of the effect of fiber volume fraction on Mode I ERR in two exemplificative models, subject to an applied transverse strain ε_x of 1%.

domain become shorter, leading to higher stresses in general and causing higher values at the crack tip. The difference in relative magnitude between Mode I and Mode II and the delay in the contact zone's onset are instead due to the interplay between two different mechanisms, both caused by the ordered microstructural arrangement of the model. In the models considered, a fully bonded fiber is always placed along the horizontal direction, aligned with the partially debonded fiber and exactly in front of the debond. By increasing V_f, the former moves closer to the latter and for small debonds this causes a magnification of the x-strain at the crack tip. For small debonds ($\leqslant 20° - 30°$) in fact, the crack tip is approximately normal to the x-direction and thus an increase in ε_x causes an increase in G_I. On the other hand, for large debonds ($\geqslant 70° - 80°$) the crack growth direction is almost aligned with the x-axis, thus a magnification in the x-strain translates into an increase of Mode II ERR. However, this increasing effect on G_{II} is partially counteracted by the presence of a fully bonded fiber on top of the debonded fiber and aligned with it. As fibers are more rigid than the surrounding matrix, the presence of the former will restrain horizontal displacements, thus hampering strong increases in G_{II} for large debonds. Furthermore, due to the mismatch in the Poisson's ratios, the fully bonded fiber placed above generates an upward-directed component of the vertical displacement field in the matrix, which tends to open the debond and causes the delay in the contact zone's onset. The interplay between these mechanisms is governed by the average interfiber distance and, in turn, by the fiber volume fraction.

These observations are in agreement with the results reported in [31], where the effect on the ERR of a partially debonded fiber of two fully bonded nearby fibers, placed symmetrically with respect to the loading direction, is studied for different angular positions (denoted as θ_2) and radial distances in a model with an effectively infinite matrix

($V_f \sim 0.09\%$). The effect of the former is studied for a constant value of the radial distance between the debonded and bonded fibers, which corresponds to a local V_f^{local} of $\sim 62\%$ assuming hexagonal packing. They report an increase in both Mode I and Mode II ERR with respect to the single fiber case when the two fibers are placed at an angle of respectively ± 25°, ±30°, ±140°, ±150°, ±155°, i.e. closest to the loading direction. Notice that for ± 25° and ± 155° the two fully bonded fibers are almost in contact, with an inter-fiber distance of ~ 0.04 times their radius. This result confirms the considerations made in the previous paragraph about the x-strain magnification caused by the presence of fully bonded fibers along the loading direction. The effect is further analyzed and discussed in Sections 3.2 and 3.4. In the range ± 40° − ±130° instead, the presence of the other fibers causes a reduction of the ERR and, particularly in the range 80° − 120°, results are very close and almost insensitive to variations in θ_2, which supports the previous conclusion about the effect of a fully bonded fiber on top the partially debonded one. This effect is treated in more detail in Section 3.3.

Comparing the results from [31] with those presented in this paper, an hypothesis can be furthermore formulated about the robustness of the results of the present article with respect to deviations in fiber position: it seems reasonable to assume a tolerance to deviations of max. ± 30° with respect to the loading direction and of max. ± 20° with respect to the through-the-thickness direction.

The effect of the local fiber content is also investigated in [31], by changing the radial distance between the partially debonded fiber and the fully bonded ones. They observe that the further the fully bonded fibers are placed from the central one, i.e. the lower the local V_f, the lower is their effect on the ERR. The magnitude of the effect is however small: the maximum increase of the total ERR is of ~ 1.15 times for
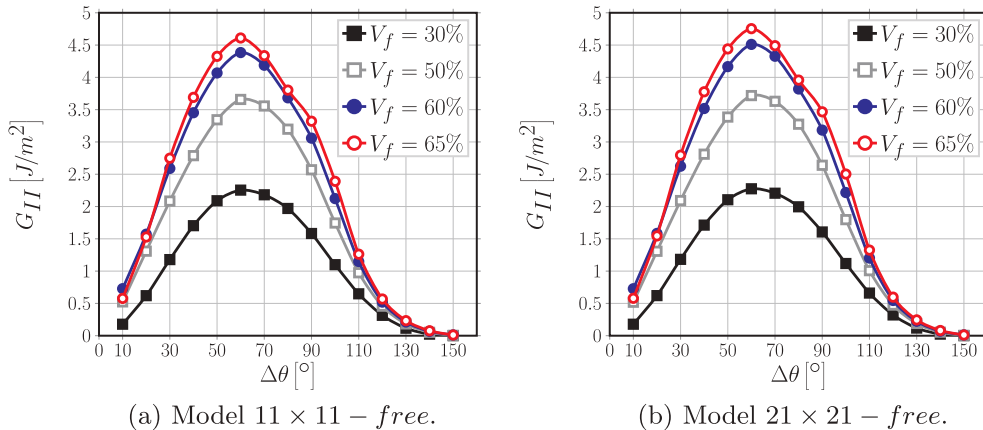

(a) Model $11 \times 11 - free$.   (b) Model $21 \times 21 - free$.

Fig. 7. A view of the effect of fiber volume fraction on Mode II ERR in two exemplificative models, subject to an applied transverse strain ε_x of 1%.

$\theta_2 = 30°$ and $150°$ when increasing V_f^{local} from 28% to 62%; the total ERR decreases by a factor of ~ 0.62 for $\theta_2 = 60°$, ~ 0.74 for $\theta_2 = 90°$ and ~ 0.5 for $\theta_2 = 120°$ when increasing V_f^{local} from 28% to 62%. Analogous results can be found in [34], where the authors consider a centrally-placed partially debonded fiber surrounded by an hexagonal cluster inside an homogenized UD composite. They observe a reduction in the ERR when the local fiber volume fraction is increased, i.e. when the spacing between fibers is reduced. The strongest change is reported for Mode II, which decreases by a factor of ~ 0.73 when the local fiber volume fraction is decreased from 66% to 78%. Thus, the trends presented in [31,34] are in agreement with our results on the effect of V_f and support the considerations made so far. The stark difference in magnitude however highlights the contrast between the effect of the local fiber volume fraction of a cluster of fibers inside an infinite medium and of the global V_f of long-range microstructural arrangements, such the ones considered in this article. The similarity in trends with the concurrent difference in magnitudes can be explained in relation to the characteristics of the elastic solution computed. In the first case the local fiber volume fraction controls the distance, with respect to the central partially debonded fiber, at which a localized perturbation zone appears in the far-field elastic solution; in the second case the global V_f determines the characteristic lengths of a global periodic solution.

3.2. Interaction between debonds in UD composites with a single row of fibers

The interaction of debonds appearing at regular intervals in an ultra-thin UD composite with a single row of fibers is studied for Mode I (Fig. 8) and Mode II (Fig. 9) and fiber content equal to 30% (Figs. 8a and 9)a and 60% (Figs. 8b and 9b). The models treated are $3 \times 1 - free$, $5 \times 1 - free$, $7 \times 1 - free$, $11 \times 1 - free$, $21 \times 1 - free$, $101 \times 1 - free$ and $201 \times 1 - free$, corresponding respectively to a debond every 3rd, 5th, 7th, 11th, 21st, 101st and 201st fiber (Fig. 1a). Given that the upper surface of the UD row is left free, the interaction with the debonded fiber in the next RUC is stronger than in any other case and the results of this section are thus the most conservative in terms of debond's growth: the ERRs should be the largest. The effect is enhanced in composites with high V_f and especially for G_{II}: at $V_f = 60\%$ the highest G_{II} value for the $201 \times 1 - free$ composite in Fig. 9b is more than 3 times higher than the G_{II} value for the $21 \times 21 - free$ composite in Fig. 7b. Even the maximum is shifted to larger angles. The G_I value is for some cases only 30% higher.

From both Figs. 8 and 9, it can be seen that the presence of a debond close to the analyzed debond decreases the strain magnification effect discussed in Section 3.1 and thus reduces the value of the ERR. This phenomenon is called "crack shielding" [26].

For Mode I, the presence of a free surface, and inversely the absence

of a fully bonded fiber along the vertical direction, implies the absence of the counteracting upward-oriented vertical component of the displacement field due to the mismatch in Poisson's ratios. This in turn translates into the constancy of the value of $\Delta\theta$ corresponding to contact zone's onset, always equal to 60°. For $V_f = 30\%$, Mode I is reduced when the spacing between debonds (in terms of number of fully bonded fibers between them in our models) decreases, but the magnitude of change is significant only in the range when the spacing is reduced from a debond every 5th fiber to one every 3rd. For comparison, the difference of peak G_I values for $V_f = 30\%$ between $5 \times 1 - free$ and $3 \times 1 - free$ is $\sim 0.2 \frac{J}{m^2}$ (around 30% of the lower value), while between $201 \times 1 - free$ and $5 \times 1 - free$ is $\sim 0.05 \frac{J}{m^2}$ (around 7% of the lower value). A similar observation can be made for $V_f = 60\%$, but for larger spacings: no difference can be seen between the case of a debond placed every 101st and every 201st fiber. These observations suggest the existence of characteristic distance dependent on the fiber volume fraction which governs the interaction between debonds: in low V_f composites ($V_f = 30\%$) the convergence to a non-interactive solution is faster (less interaction between debonded fibers in neighboring RUCs).

Without costraint on the upper surface, the strain magnification effect creates a larger displacement gap in the x-direction, which increases Mode II for larger debonds. When debonds are far apart, the series of rigid elements in the ultra-thin composite row (constituted by fully bonded fibers and their surrounding matrix) creates higher x-strains than in average in the element with the debonded fiber, which in turn generates higher tangential displacements at the crack tip for larger debonds. Conversely, when debonds are closer (smaller number of rigid elements between them), the strain concentration in the debonded element is more similar to the applied strain (the magnification is reduced) and the tangential displacement component at the crack tip decreases for large $\Delta\theta$. This is the mechanism behind the change in the value of $\Delta\theta$ for which the peak of G_{II} occurs: from 70° to 50° at 30%, and from 80° to 40° at 60% going from the higher to the smaller spacing of debonds. Differently from Mode I, the presence of a characteristic distance is harder to establish. For $V_f = 30\%$ (Fig. 9a), it seems reasonable to establish it at around 100 fully bonded fibers between each debond. For $V_f = 60\%$ (Fig. 9b), the difference between models $101 \times 1 - free$ and $201 \times 1 - free$ is still sizable, thus preventing the establishment of such characteristic distance. It is possible to observe, however, that the change between $101 \times 1 - free$ and $201 \times 1 - free$ is significantly smaller than between $21 \times 1 - free$ and $101 \times 1 - free$ ($2\left[\frac{J}{m^2}\right]$ vs $11\left[\frac{J}{m^2}\right]$), thus suggesting the existence of the characteristic distance outside the range studied. Nevertheless, one should question whether the single row composite with free surface is an appropriate RUC for defining the upper bound for G_{II}: G_{II} may be more affected by the free surface than by the effect of the interaction between debonds in the
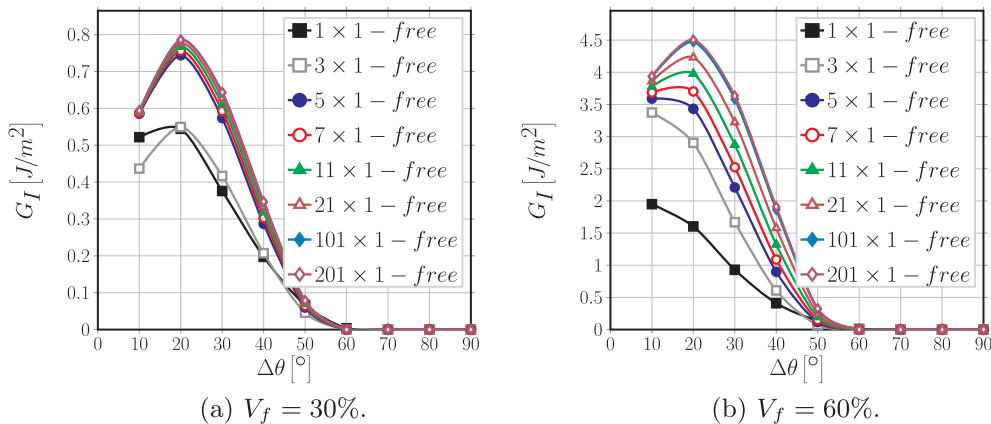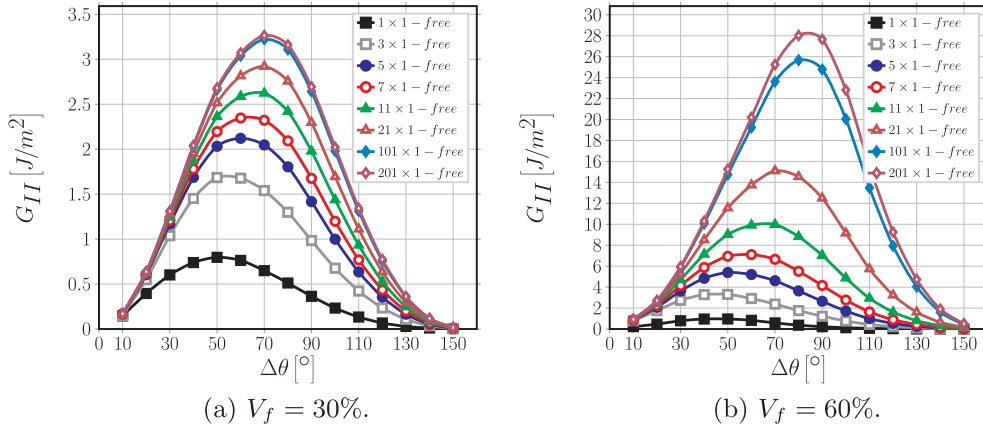

(a) $V_f = 30\%$.

(b) $V_f = 60\%$.

Fig. 8. Effect of the interaction between debonds appearing at regular intervals on Mode I ERR in an UD with a single row of fibers at different levels of fiber volume fraction V_f, subject to an applied transverse strain ε_x of 1%.

(a) $V_f = 30\%$. (b) $V_f = 60\%$.

Fig. 9. Effect of the interaction between debonds appearing at regular intervals on Mode II ERR in an UD with a single row of fibers at different levels of fiber volume fraction V_f, subject to an applied transverse strain ε_x of 1%.

row.

3.3. Influence of rows of fully bonded fibers on debond's ERR in the middle row

The effect of the presence of rows of fully bonded fibers on debond's growth in the central row with all fibers partially debonded is studied for Mode I (Fig. 10) and Mode II (Fig. 11) and fiber content equal to 30% (Figs. 10a and 11)a and 60% (Figs. 10b and 11b). The models treated are $1 \times 3 - free$, $1 \times 5 - free$, $1 \times 7 - free$, $1 \times 11 - free$, $1 \times 21 - free$, $1 \times 101 - free$ and $1 \times 201 - free$, corresponding to a UD composite with respectively 3, 5, 7, 11, 21, 101 and 201 rows of fibers (Fig. 2a).

The results shown strengthen the arguments made in Sections 3.1 and 3.2. It can, in fact, be seen in Fig. 10 that an increasing number of bonded fiber rows across the thickness delays the onset of the contact zone to a debond of 70° in size, due to the introduction of an additional positive component of the vertical displacement which translates into an opening displacement at the debond's tip.

Comparing Fig. 9b with Fig. 11b, we observe that the presence of bonded fiber rows significantly reduce the G_{II} and its maximum is shifted back to 60°, thus confirming the hypothesis in Section 3.2 that the absence of G_{II} convergence with the increasing distance in a single-row composite is caused more by the free surface than by the interaction between debonds.

The results of both Mode I and Mode II show that the introduction of an increasing number of fully bonded fiber rows doesn't change the ERR calculated at the crack tip after adding more than one row (the convergence is very fast). A small effect, mostly on Mode I, of the

number of bonded fiber rows can be observed at low fiber content (Figs. 10a and 11a), while for high fiber content the smaller model with only one fiber row above the partially debonded one is already re-presentative.

3.4. Effect of multiple rows of bonded fibers on debonding in the central row of a UD composite with different distances between debonded fibers

The ERR of debonds appearing at regular intervals in the central row of fibers in UD composites is affected by the number of rows with bonded fibers. The effect is investigated using different combinations of horizontal debond spacing, controlled by the number of bonded fibers in the central row of the RUC, and the number of rows of bonded fibers on top of it. The following models have been studied: $3 \times 3 - free$, $5 \times 3 - free$, $5 \times 5 - free$, $7 \times 3 - free$, $7 \times 5 - free$, $7 \times 7 - free$, $11 \times 3 - free$, $11 \times 5 - free$, $11 \times 7 - free$, $11 \times 11 - free$, $21 \times 3 - free$, $21 \times 5 - free$, $21 \times 7 - free$, $21 \times 11 - free$, $21 \times 21 - free$, $101 \times 3 - free$, $101 \times 5 - free$, $101 \times 7 - free$, $101 \times 11 - free$, $201 \times 3 - free$, $201 \times 5 - free$, $201 \times 7 - free$, $201 \times 11 - free$ (Fig. 2b).

The results shown in Fig. 12 confirm the observations discussed in Sections 3.2 and 3.3: the presence of fully bonded fiber rows on top of the central row with debonded fibers reduces the interaction with the free surface and thus has a restraining effect on the ERR, that counteracts the magnification due to an increasing number of fully bonded fibers in the horizontal direction. The interplay is further modulated by the fiber content. Observing Fig. 12, it is possible to note how the free surface interaction decays fast: the presence of 5 fiber rows across the thickness is already sufficient to prevent any significant effect of

(a) $V_f = 30\%$. (b) $V_f = 60\%$.
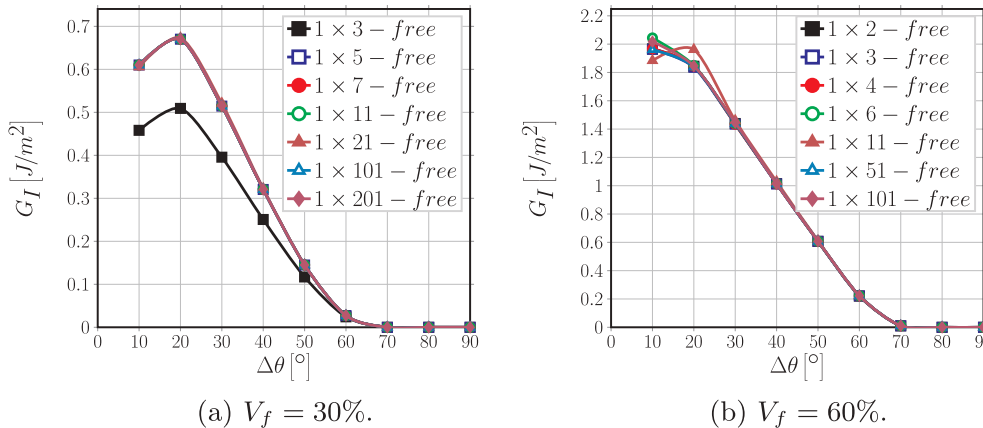
Fig. 10. Influence of rows of fully bonded fibers on debond's growth in Mode I ERR in a centrally located row of debonded fibers at different levels of fiber volume fraction V_f, subject to an applied transverse strain ε_x of 1%.

(a) $V_f = 30\%$.

(b) $V_f = 60\%$.
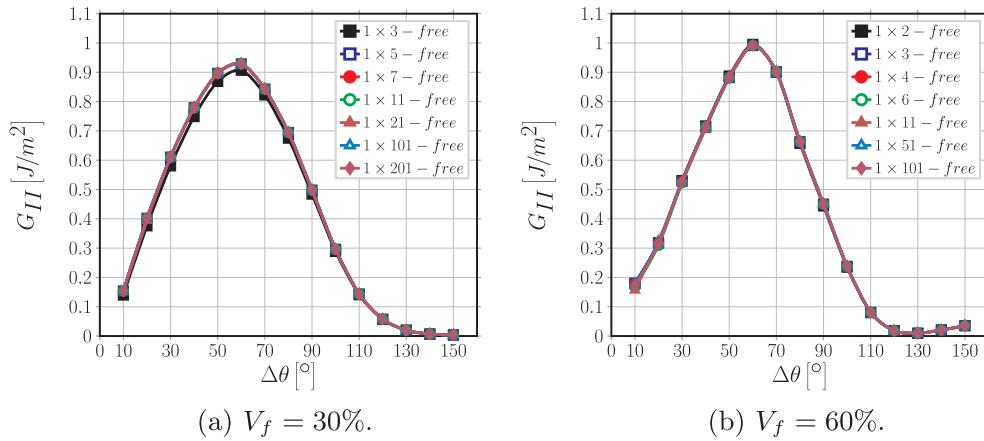
Fig. 11. Influence of rows of fully bonded fibers on debond's growth in Mode II ERR in a centrally located row of debonded fibers at different levels of fiber volume fraction V_f, subject to an applied transverse strain ε_x of 1%.

(a) G_I.

(b) G_{II}.
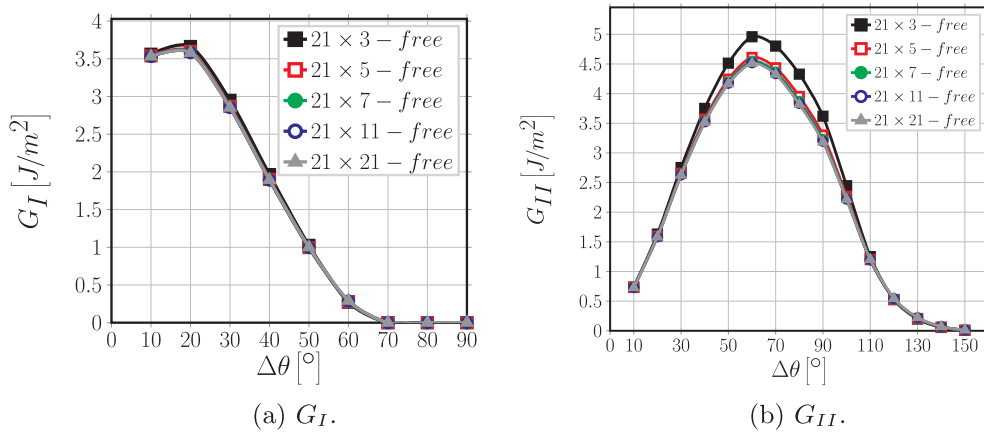
Fig. 12. Effect on Mode I and Mode II ERR of the presence of an increasing number of rows of fully bonded fibers in UD composites with debonds appearing every 10th fiber (model $21 \times k - free$). $V_f = 60\%$ and $\varepsilon_x = 1\%$.

(a) G_I.

(b) G_{II}.
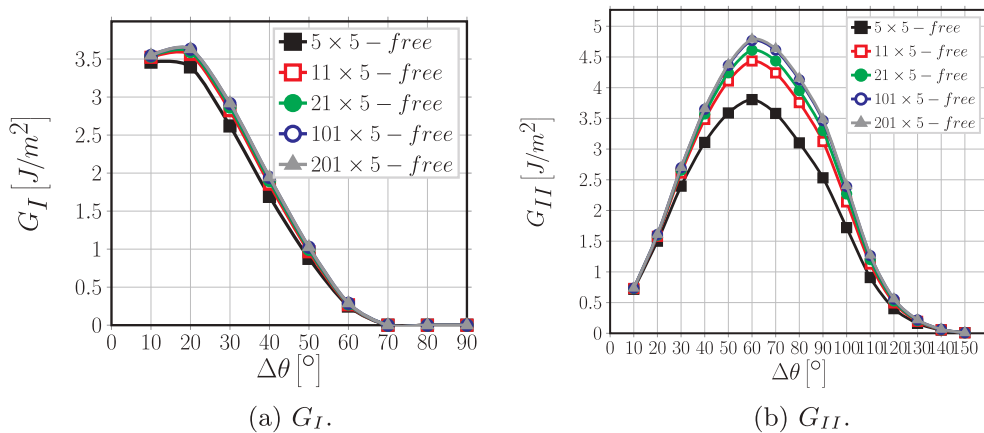
Fig. 13. Effect on Mode I and Mode II ERR of increasing the spacing between debonds appearing in the central row of fibers in a UD composite with a fixed number of rows across the thickness. $V_f = 60\%$, $k = 5$ and $\varepsilon_x = 1\%$.

additional fiber rows on the ERR of a debond in the central row.

The results in Fig. 13 show instead the effect of increasing the distance between two consecutive debonds in the central row of a UD composite of given thickness. In agreement with the observations of Section 3.2, increasing the distance between debonds (measured in terms of fully bonded fibers between them) causes an increase in the ERR in both Mode I and Mode II. For both Mode I and Mode II, it is possible to observe the existence of a characteristic distance which

defines the limit between the interactive and the non-interactive solution. Furthermore, comparing Fig. 13a and b, it is possible to notice that Mode I is less sensitive than Mode II to the horizontal spacing of debonds.
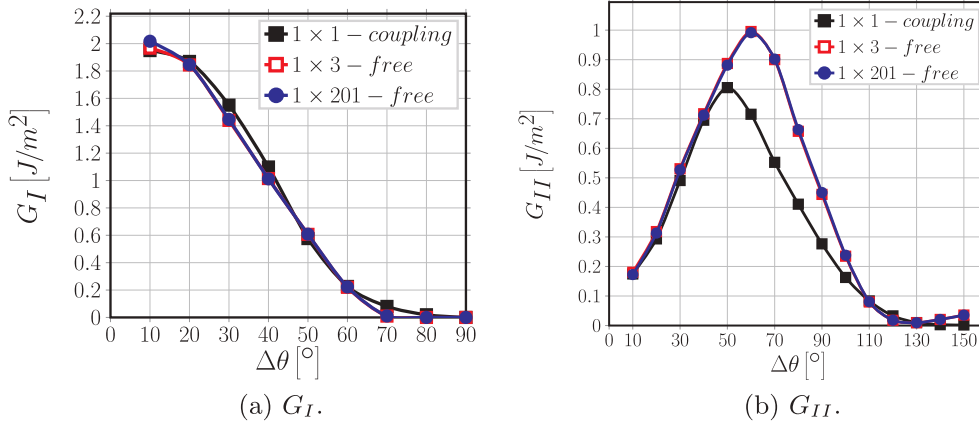
(a) G_I.

(b) G_{II}.

Fig. 14. Comparison of the ERR between the single fiber model with coupling conditions along the upper boundary and the $1 \times k - free$ model. $V_f = 60\%$ and $\varepsilon_x = 1\%$.

3.5. Comparison with the single fiber model with equivalent boundary conditions

The single fiber RUC ($1 \times 1 - free$ or $1 \times 1 - coupling$) corresponds to the most damaged state of the composite, i.e. the state in which all fibers have debonds. The $1 \times 1 - free$ model represents an ultra-thin UD composite with a single row of partially debonded fibers. The $1 \times 1 - coupling$ model, where the displacement coupling is used to enforce periodic boundary conditions, represents an infinite composite.

The comparison of the $1 \times 1 - free$ model with one row multi-fiber models $n \times 1 - free$ in Figs. 8 and 9 show that the former provides in general the lowest value of the ERR (the highest crack shielding case).

The $1 \times 1 - coupling$ model is compared with $1 \times 3 - free$ and $1 \times 201 - free$ models in Fig. 14. In all three models the distance between debonds in the x-direction is the same and the difference is in the vertical direction. The $1 \times 1 - coupling$ model describes the interaction between debonds in different rows of debonded fibers whereas the $1 \times k - free$ models describe the effect of the proximity of the composite's free surface. The Mode I ERR in the $1 \times 3 - free$ and $1 \times 201 - free$ model is very similar to the $1 \times 1 - coupling$ model, which leads to a rather surprising conclusion. In both models we have, on the top of the central one, a large amount of fibers (bonded in two cases and debonded in the third case). It appears that the effect of bonded and debonded fibers on the central debond is the same. This implies that, for Mode I ERR, the interaction between debonds in elements placed on top of each other is small.

The same comparison for Mode II shows a sizeable difference in the range $50° - 90°$, while the results almost coincide for smaller values of $\Delta\theta$. The lower values of G_{II} of the $1 \times 1 - coupling$ model in the range $50° - 90°$ are due to the shielding effect of a debond of the same size in the fiber just above the central one (modeled by the coupling boundary condition), which leaves the strip of matrix between the two fibers free to deform away from both of them due to the Poissons effect and thus favors Mode I and reduces Mode II. This translates into the delay in the appearance of the contact zone, particularly evident in Fig. 14a.

4. Conclusions & outlook

Several models of Repeating Unit Cell, representative of different microstructural arrangements of a unidirectional (UD) composite, have been studied in order to investigate the effect on fiber/matrix interface crack growth of the presence of partially debonded and/or fully bonded fibers. Regular microstructures based on square-packing arrangements of fibers have been loaded in transverse tension, with debonds appearing in the central row of fibers at regular intervals measured in terms of number of fully bonded fibers between them. This central row is embedded in-between a varying number of rows with perfectly bonded fibers. The surface of the composite is either traction-free or

with imposed vertical displacement constraint imitating a periodic structure in the composite thickness direction.

In each RUC, the fiber volume fraction is spatially homogeneous (no fiber clustering is considered) and the fiber distribution is uniform by design, which establishes a direct relationship between fiber content and inter-fiber distance. The main conclusions of this work are summarized here.

1. With a decreasing number of fully bonded fibers between two partially debonded fibers in the central row, the ERR decreases. It seems to exist a characteristic distance between debonds which defines the transition to a non-interactive solution. However, this distance depends on the number of perfectly bonded fiber rows surrounding the central row and on the fiber volume fraction. This distance can be estimated to be around 100 fully bonded fibers for a 1-fiber-row thick UD with $V_f = 30\%$ and 200 for a 1-fiber-row thick UD with $V_f = 60\%$, while it is expected to be around 100 fibers for a 5-fibers-row thick UD with $V_f = 60\%$.
2. The presence of a free surface close to the debond leads to higher Mode I and Mode II ERRs and a shift of the peak G values to larger debonds.
3. The presence of fibers (fully or partially bonded) in the composite thickness direction, along the same vertical line as the analyzed central fiber, appears to have a restraining effect on both G_I and G_{II}. The free composite surface effect on the ERR decays very fast: adding more than 2 fully bonded fibers below and above the central row leads to stable constant values of ERR.
4. The presence of a debond in the fiber above the central partially debonded one only delays the appearance of the contact zone, while no significant effect on the ERR has been observed.
5. Increasing the fiber content (decreasing the inter-fiber distance), magnifies in general the effects described in the previous points.
6. The results and conclusions presented agree well with previous observations reported in the literature [31,34]. A mechanical explanation of the observed trends has been presented based on the mismatch in elastic properties, particularly Poisson's ratios, and the positions of fibers and debonds with respect to the loading direction.

References

[1] D.A. McCarville, J.C. Guzman, A.K. Dillon, J.R. Jackson, J.O. Birkland, 3.5 Design,

Manufacture and Test of Cryotank Components, Elsevier, 2018, pp. 153–179. https://doi.org/10.1016/b978-0-12-803581-8.09958-6.

[2] Y.H.N. Kim, S. Ko, W.-S. Lay, J. Tian, P. Chang, S.U. Thielk, H.-J. Bang, J. Yang, Effects of shallow biangle, thin-ply laminates on structural performance of composite wings, AIAA J. 55 (6) (2017) 2086–2092, https://doi.org/10.2514/1.j055465.

[3] A. Kopp, S. Stappert, D. Mattsson, K. Olofsson, E. Marklund, G. Kurth, E. Mooij, E. Roorda, The aurora space launcher concept, CEAS Space J. 10 (2) (2017) 167–187, https://doi.org/10.1007/s12567-017-0184-2.

[4] K. Kawabe, S. Tomoda, T. Matsuo, A pneumatic process for spreading reinforcing fiber tow, in: Proceedings of the 42nd International SAMPE Symposium and Exhibition, SAMPE, pp. 65–76.

[5] K. Kawabe, New spreading technology for carbon fiber tow and its application to composite materials, Sen'i Gakkaishi 64 (8) (2008) 262–267, https://doi.org/10.2115/fiber.64.p_262.

[6] K. Kawabe, H. Sasayama, S. Tomoda, New carbon fiber tow-spread technology and applications to advanced composite materials, SAMPE J. 45 (2) (2008) 6–17.

[7] H. Sasayama, K. Kawabe, S. Tomoda, I. Ohsawa, K. Kageyama, N. Ogata, Effect of lamina thickness on first ply failure in multidirectionally laminated composites, in: Proceedings of the 8th Japan SAMPE Symposium, SAMPE, 2003.

[8] S. Sihn, R. Kim, K. Kawabe, S. Tsai, Experimental studies of thin-ply laminated composites, Compos. Sci. Technol. 67 (6) (2007) 996–1008, https://doi.org/10.1016/j.compscitech.2006.06.008.

[9] T. Yokozeki, Y. Aoki, T. Ogasawara, Experimental characterization of strength and damage resistance properties of thin-ply carbon fiber/toughened epoxy laminates, Compos. Struct. 82 (3) (2008) 382–389, https://doi.org/10.1016/j.compstruct.2007.01.015.

[10] T. Yokozeki, A. Kuroda, A. Yoshimura, T. Ogasawara, T. Aoki, Damage characterization in thin-ply composite laminates under out-of-plane transverse loadings, Compos. Struct. 93 (1) (2010) 49–57, https://doi.org/10.1016/j.compstruct.2010.06.016.

[11] A. Arteiro, G. Catalanotti, J. Xavier, P. Camanho, Large damage capability of non-crimp fabric thin-ply laminates, Compos. Part A: Appl. Sci. Manuf. 63 (2014) 110–122, https://doi.org/10.1016/j.compositesa.2014.04.002.

[12] R. Amacher, J. Cugnoni, J. Botsis, L. Sorensen, W. Smith, C. Dransfeld, Thin ply composites: experimental characterization and modeling of size-effects, Compos. Sci. Technol. 101 (2014) 121–132, https://doi.org/10.1016/j.compscitech.2014.06.027.

[13] J. Cugnoni, R. Amacher, S. Kohler, J. Brunner, E. Kramer, C. Dransfeld, W. Smith, K. Scobbie, L. Sorensen, J. Botsis, Towards aerospace grade thin-ply composites: effect of ply thickness, fibre, matrix and interlayer toughening on strength and damage tolerance, Compos. Sci. Technol. 168 (2018) 467–477, https://doi.org/10.1016/j.compscitech.2018.08.037.

[14] H. Saito, H. Takeuchi, I. Kimpara, Experimental evaluation of the damage growth restraining in 90 layer of thin-ply cfrp cross-ply laminates, Adv. Compos. Mater. 21 (1) (2012) 57–66, https://doi.org/10.1163/156855112X629522.

[15] K.W. Garrett, J.E. Bailey, Multiple transverse fracture in 90° cross-ply laminates of a glass fibre-reinforced polyester, J. Mater. Sci. 12 (1) (1977) 157–168, https://doi.org/10.1007/bf00738481.

[16] A. Parvizi, J.E. Bailey, On multiple transverse cracking in glass fibre epoxy cross-ply laminates, J. Mater. Sci. 13 (10) (1978) 2131–2136, https://doi.org/10.1007/bf00541666.

[17] A. Parvizi, K.W. Garrett, J.E. Bailey, Constrained cracking in glass fibre-reinforced epoxy cross-ply laminates, J. Mater. Sci. 13 (1) (1978) 195–201, https://doi.org/10.1007/bf00739291.

[18] J.E. Bailey, A. Parvizi, On fibre debonding effects and the mechanism of transverse-ply failure in cross-ply laminates of glass fibre/thermoset composites, J. Mater. Sci. 16 (3) (1981) 649–659, https://doi.org/10.1007/bf02402782.

[19] J.E. Bailey, P.T. Curtis, A. Parvizi, On the transverse cracking and longitudinal splitting behaviour of glass and carbon fibre reinforced epoxy cross ply laminates and the effect of poisson and thermally generated strain, Proc. Roy. Soc. A: Math., Phys. Eng. Sci. 366(1727) (1979,) 599–623, https://doi.org/10.1098/rspa.1979.0071.

[20] A.H. England, An arc crack around a circular elastic inclusion, J. Appl. Mech. 33 (3) (1966) 637, https://doi.org/10.1115/1.3625132.

[21] A. Perlman, G. Sih, Elastostatic problems of curvilinear cracks in bonded dissimilar materials, Int. J. Eng. Sci. 5 (11) (1967) 845–867, https://doi.org/10.1016/0020-7225(67)90009-2.

[22] M. Toya, A crack along the interface of a circular inclusion embedded in an infinite solid, J. Mech. Phys. Solids 22 (5) (1974) 325–348, https://doi.org/10.1016/0022-5096(74)90002-7.

[23] M. Comninou, The interface crack, J. Appl. Mech. 44 (4) (1977) 631, https://doi.org/10.1115/1.3424148.

[24] F. París, J.C. Caño, J. Varna, The fiber-matrix interface crack — a numerical analysis using boundary elements, Int. J. Fract. 82 (1) (1996) 11–29, https://doi.org/10.1007/bf00017861.

[25] J. Varna, F. París, J.C. Caño, The effect of crack-face contact on fiber/matrix debonding in transverse tensile loading, Compos. Sci. Technol. 57 (5) (1997) 523–532, https://doi.org/10.1016/s0266-3538(96)00175-3.

[26] I. García, V. Mantič, E. Graciani, Debonding at the fibre–matrix interface under remote transverse tension. one debond or two symmetric debonds? Eur. J. Mech. A. Solids 53 (2015) 75–88, https://doi.org/10.1016/j.euromechsol.2015.02.007.

[27] E. Correa, E. Gamstedt, F. París, V. Mantič, Effects of the presence of compression in transverse cyclic loading on fibre–matrix debonding in unidirectional composite plies, Compos. Part A: Appl. Sci. Manuf. 38 (11) (2007) 2260–2269, https://doi.org/10.1016/j.compositesa.2006.11.002.

[28] E. Correa, V. Mantič, F. París, Effect of thermal residual stresses on matrix failure under transverse tension at micromechanical level: a numerical and experimental analysis, Compos. Sci. Technol. 71 (5) (2011) 622–629, https://doi.org/10.1016/j.compscitech.2010.12.027.

[29] E. Correa, F. París, V. Mantič, Effect of the presence of a secondary transverse load on the inter-fibre failure under tension, Eng. Fract. Mech. 103 (2013) 174–189, https://doi.org/10.1016/j.engfracmech.2013.02.026.

[30] E. Correa, F. París, V. Mantič, Effect of a secondary transverse load on the inter-fibre failure under compression, Compos. Part B: Eng. 65 (2014) 57–68, https://doi.org/10.1016/j.compositesb.2014.01.005.

[31] C. Sandino, E. Correa, F. París, Numerical analysis of the influence of a nearby fibre on the interface crack growth in composites under transverse tensile load, Eng. Fract. Mech. 168 (2016) 58–75, https://doi.org/10.1016/j.engfracmech.2016.01.022.

[32] C. Sandino, E. Correa, F. París, Composite materials under transverse biaxial loads: study of the influence of a nearby fibre on the interface crack growth under tension, Proceeding of the 17th European Conference on Composite Materials (ECCM-17), 2016.

[33] C. Sandino, E. Correa, F. París, Interface crack growth under transverse compression: nearby fibre effect, Proceeding of the 18th European Conference on Composite Materials (ECCM-18), 2018.

[34] L. Zhuang, A. Pupurs, J. Varna, R. Talreja, Z. Ayadi, Effects of inter-fiber spacing on fiber-matrix debond crack growth in unidirectional composites under transverse loading, Compos Part A: Appl Sci Manuf 109 (2018) 463–471, https://doi.org/10.1016/j.compositesa.2018.03.031.

[35] J. Varna, L.Q. Zhuang, A. Pupurs, Z. Ayadi, Growth and interaction of debonds in local clusters of fibers in unidirectional composites during transverse loading, Key Eng. Mater. 754 (2017) 63–66, https://doi.org/10.4028/www.scientific.net/kem.754.63.

[36] Simulia, Providence, RI, USA, ABAQUS/Standard User's Manual, Version 6.12, 2012.

[37] J. Varna, F. Paris, J.C. del Cano, The effect of crack-face contact on fiber/matrix debonding in transverse tensile loading, Compos. Sci. Technol. 57 (5) (1997) 523–532, https://doi.org/10.1016/s0266-3538(96)00175-3.

[38] R. Krueger, Virtual crack closure technique: history, approach, and applications, Appl. Mech. Rev. 57 (2) (2004) 109, https://doi.org/10.1115/1.1595677.

[39] J.R. Rice, A path independent integral and the approximate analysis of strain concentration by notches and cracks, J. Appl. Mech. 35 (2) (1968) 379, https://doi.org/10.1115/1.3601206.

[40] L.E. Asp, L.A. Berglund, P. Gudmundson, Effects of a composite-like stress state on the fracture of epoxies, Compos. Sci. Technol. 53 (1) (1995) 27–37, https://doi.org/10.1016/0266-3538(94)00075-1.

[41] L. Asp, L. Berglund, R. Talreja, A criterion for crack initiation in glassy polymers subjected to a composite-like stress state, Compos. Sci. Technol. 56 (11) (1996) 1291–1301, https://doi.org/10.1016/s0266-3538(96)00090-5.

[42] F. París, E. Correa, V. Mantič, Kinking of transversal interface cracks between fiber and matrix, J. Appl. Mech. 74 (4) (2007) 703, https://doi.org/10.1115/1.2711220.